An Electrospray Ion Source for Ultra–High Vacuum Deposition of Organic Molecules

Dissertation

zur Erlangung des Doktorgrades
der Mathematisch–Naturwissenschaftlichen Fakultät
der Christian–Albrechts–Universität zu Kiel

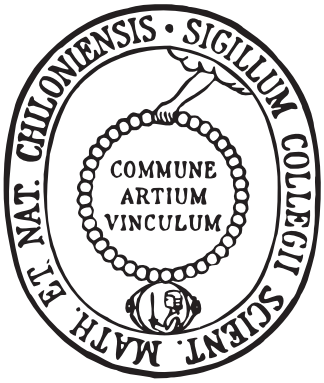

vorgelegt von

Christian Hamann

Kiel, 2011

Referent/in:	Prof. Dr. Richard Berndt
Koreferent/in:	Prof. Dr. Olaf Magnussen
Tag der mündlichen Prüfung:	18.11.2011
Zum Druck genehmigt:	18.11.2011

gez. Prof. Dr. Lutz Kipp, Dekan

Kurzfassung

Im Rahmen dieser Arbeit wurde eine Apparatur zum Deponieren von durch Elektrospray–Ionisation erzeugten Ionen auf Oberflächen unter Ultrahochvakuum–Bedingungen entworfen, aufgebaut und in Betrieb genommen. Die unter Ultrahochvakuum–Bedingungen zur Verfügung stehenden Depositionsmethoden können für Moleküle mit zu niedrigem Dampfdruck in der Regel nicht genutzt werden, da die gängigen Verfahren auf Sublimation beruhen und daher nicht anwendbar sind. Möglichkeiten der Präparation an Luft kommen auf Grund der geringeren Reinheit oft nicht in Betracht.

Elektrospray–Ionisation ist eine Möglichkeit, solche Moleküle schonend in die Gasphase zu überführen. Da die Ionen bei diesem Verfahren bei Umgebungsdruck erzeugt werden, müssen zwölf Größenordnungen Druckdifferenz überbrückt werden. Dazu wurden fünf differentielle Pumpstufen aufgebaut. Verschiedene ionenoptische Bauteile leiten den Ionenstrahl durch diese Stufen und sorgen gleichzeitig für seine Reinigung. Ein elektrostatischer Quadrupol–Umlenker trennt die Ionen von neutralen Bestandteilen, die der Ionenquelle entstammen, und sorgt für eine Begrenzung der kinetischen Energie der Ionen. Ein Quadrupol–Massenspektrometer dient der Massenselektion während des Depositionsprozesses.

Ein Schwerpunkt der Entwicklung war der Entwurf eines Ionentrichters, der sich über zwei differentielle Pumpstufen erstreckt und eine Transmission von etwa zehn Prozent erreicht. Dieser Trichter unterscheidet sich von vorherigen Entwürfen durch geringere innere Durchmesser der Elektroden, wodurch die Effektivität des differentiellen Pumpens erhöht wird. Die Transmissionseigenschaften dieses Trichters wurden in detaillierten Simulationen untersucht.

Parallel zum Aufbau der Anlage wurde ein Tieftemperatur–Rastertunnel– und –Rasterkraftmikroskop beschafft, welches in Zusammenarbeit mit dem Hersteller *SPS CreaTec GmbH* speziell für den Betrieb mit der Ionen–Quelle angepasst wurde.

Die Deposition der Ionen erfolgt in der Präparationskammer des Rastertunnelmikroskop–Systems bei einem Druck von 1×10^{-9} mbar, bei Ionenströmen bis zu 100 pA und bei Aufschlagsenergien von weniger als 10 eV. In diesen drei Schlüsselspezifikationen ist unsere Apparatur auf dem neuesten Stand der Technik. Für Untersuchungen mit dem Rastertunnelmikroskop typische Schichten von einigen zehn Prozent einer Monolage können so innerhalb weniger Stunden präpariert werden. Präparation und Untersuchung können erfolgen, ohne dass die zu untersuchende Probe das Ultrahochvakuum verlassen muss.

Eine Reihe verschiedener – überwiegend thermisch instabiler – Substanzen wurde

auf Oberflächen von Edelmetall–Einkristallen deponiert und mit dem Rastertunnelmikroskop untersucht um die Leistungsfähigkeit des Systems unter Beweis zu stellen. Untersuchungen an dem Porphyrin MnTPPS zeigen, dass die erreichbare Reinheit vergleichbar mit der durch Sublimation oder gepulstem Einspritzen erzeugten Molekülschichten ist. Dass das Verfahren für große empfindliche Biomoleküle anwendbar ist, zeigen Experimente mit Desoxyribonukleinsäure und bovinem Serumalbumin. Experimente mit Liganden von metall–organischen Gittern unterstreichen die Anwendbarkeit auch für kleine organische Moleküle. Rutheniumkomplexe, wie das untersuchte N3, sind auf Grund ihrer Anwendbarkeit in elektrochemischen Farbstoff–Solarzellen von großem technischen Interesse. Soweit bekannt konnten solche Komplexe zum ersten Mal individuell spektroskopisch mit Hilfe der Rastertunnelspektroskopie untersucht werden.

Abstract

During the course of this thesis a new instrument for the deposition of ions, produced by electrospray ionization, under ultra–high vacuum conditions was designed, assembled, and put into operation. The deposition techniques available under ultra–high vacuum conditions can usually not be applied to molecules with low vapour pressures, because most of these techniques are based on sublimation. The preparation techniques available under ambient conditions often do not come into consideration because of their lower degree of purity.

Electrospray ionization is one possibility to transfer these molecules gently into the gas phase. Because the ions are created under ambient conditions in this process, a pressure difference of twelve orders of magnitude has to be bridged. For that reason five differentially pumped vacuum stages were set up. Several ion optical components guide the ion beam through these stages and ensure its purification. A quadrupole deflector separates the ions from neutral contaminations, originating from the ion source, and confines the ions' kinetic energy. A quadrupole mass filter is used for mass selection during the deposition process.

One main focus of the development was the design of an ion funnel, extending over two differentially pumped stages and achieving transmission of roughly ten percent. This ion funnel exhibits a higher efficiency of the differentially pumping than previous reported designs, because the inner diameter of its electrodes is smaller. The transmission properties of this funnel were investigated by detailed simulations.

In parallel to the construction of the deposition instrument a low–temperature scanning tunnelling and atomic force microscope was purchased, which was adapted for the assembly with the ion source in cooperation with the manufacturer *SPS CreaTec GmbH*.

The ion deposition is performed in the preparation chamber of the scanning tunnelling microscope system at a pressure of 1×10^{-9} mbar, ion currents up to 100 pA and impact energies below 10 eV. The apparatus is state of the art in these key features. Coverages of some ten percent of a monolayer–well suited for investigation by scanning tunnelling microscopy–can be prepared within a few hours. The prepared sample can be analysed without ever leaving the ultra–high vacuum.

A number of different substances, most of them thermally unstable, were deposited on the surfaces of noble metal single crystals and studied by scanning tunnelling microscopy to prove the capabilities of the system. Investigations on the porphyrin MnTPPS show that purities of the molecular layers comparable to sublimation and pulsed injection can be achieved. The applicability on large fragile biomolecules

was verified by experiments on deoxyribonucleic acid and bovine serum albumin. Experimenst on the ligands of metal–organic grid complexes confirm the suitability for small organic molecules. Ruthenium complexes, such as the investigated N3, are of great technological interest, due to their utilisation in dye–sensitized solar cell. To the best of our knowledge we present the first spectroscopic investigations on individual complexes of this kind.

Contents

Introduction

Nanosciences is one of the most prominent research fields of our times, in which physics, chemistry, and biology come into touch. It is beneficial to analyse substances of interest in these research fields and their interaction with solid surfaces by the full arsenal of techniques available in surface science, especially the scanning probe techniques. To investigate these systems with the same accuracy as known from, for example, bare single crystal surfaces we have to find suitable deposition techniques.

Deposition of molecules, with low vapor pressures at standard conditions, onto surfaces in ultra–high vacuum can be achieved by techniques such as thermal sublimation and thermal shock sublimation [2]. Sublimation techniques can achieve very high degrees of purity, but cannot be applied to substances that are thermally unstable or have too low vapour pressures. Shock sublimation is basically only a variation of the normal sublimation. Since rapid heating favours evaporation over decomposition, this technique enlarges the number of possible substances slightly.

Another *in vacuo* deposition method is the pulse injection [3–5] where a solution containing the substance of interest is directly injected into the vacuum chamber. Other possibilities for the deposition of macromolecules from solution at ambient pressure, such as spin coating, Langmuir–Blodgett films, and ink–jet printing, are also available. The deposition from the liquid phase is much softer but usually some contaminations due to solvents remain at the surface. The pulse injection method is superior to the other depositions from solution in this regard because most of the solvent may be expected to evaporate before the molecules reach the surface. However the solvent molecules can still be adsorbed directly from the gas phase as their partial pressure is relatively high. Achieving the low impurity densities, which are typical of thermal sublimation, is difficult by deposition from solution.

None of the mentioned deposition techniques is appropriate for fragile substances, like large biomolecules, enabling to investigate them and their interaction with the surface in completely known conditions.

The deposition of ionized molecules is a promising approach to increase the range of available substances. Mass spectrometry may be used to monitor the cleanliness of the substances and the integrity of the molecular ions during deposition. Mass spectrometry provides two established ionization techniques for large and fragile molecules, Matrix Assisted Laser Desorption / Ionization and Electrospray Ionization. We decided in favour of the electrospray ionization method, because it is not only useful for non–volatile macromolecules such as polymers and larger biomolecules, but also for other soluble substances. Additionally it can provide sufficiently high constant

ion current and extends the mass range of the mass analyser, because of the existence of multiple charged ions. Electrospray ionization was introduced in the early 1980s by Fenn et al. and awarded a Nobel Prize in Chemistry in 2002.

The first deposition of different substances by electrospraying was performed to create uniform thin films for further investigation by plasma desorption mass spectrometry [6]. In 2003 and 2004 the first in vacuum deposition of mass filtered protein ions produced by electrospray ionization on solid and liquid surfaces, retaining their native structure and biological activity, was reported [7, 8].

Extremely diluted sub-monolayer films of proteins and gold nanoparticles were deposited by electrospraying and imaged by atomic force microscopy by Rauschenbach et al. [9]. The same deposition source was used for the deposition of crown ether alkali host–guest complexes which were studied by scanning tunnelling microscopy [10]. In this case deposition was performed under high vacuum conditions and mass filtering was employed.

A very sophisticated design has been proposed by Hadjar et al. [11–13] to prepare samples of peptides and metal organic complexes using the so–called soft landing technique [14]. This experiment comprises a quadrupole mass filter and a quadrupole deflector and permits deposition under ultra–high vacuum conditions.

An *in vacuo* electrospray has been proposed in Reference [15], but this technique has the disadvantage of relatively high solvent concentrations in the gas phase similar to the pulsed injection technique. Therefore it is not quite comparable to the other experiments.

In the present work an electrospray apparatus for deposition of organic molecules on surfaces in ultra–high vacuum is presented. The electrospray deposition setup is directly attached to a cryogenic scanning tunnelling and atomic force microscope, which enables detailed characterisation of the deposited molecules. To render it useful for experiments on clean metal surfaces in ultra–high vacuum it is necessary to achieve sufficiently large ion currents, which enable deposition of a monolayer on a time scale of hours. As the ions reach the surface, kinetic energies of not more than a few electronvolt are desirable to avoid their fragmentation or damage to the substrate. Moreover, neutral particles, such as solvent molecules, should be prevented from reaching the substrate as well as charged impurities, such as molecular fragments.

The kinetic energy at the impact can be controlled by an electrostatic quadrupole deflector which separates neutral particles at the same time. An in–line quadrupole mass spectrometer filters the ions to deposit by their mass to charge ratio. With an ion funnel in the first two vacuum stages a high ion transmission is achieved.

Typically coverages of the order of ten percent of a monolayer are particularly useful as pristine metal substrate areas are required for preparing the scanning tunnelling microscope tip and monitoring its status.

Chapter 1 of this thesis discusses some consideration regarding the demands made on the electrospray deposition system, which have been considered in the design. In Chapter 2 you will find a review of the electrospray ionization technique, a detailed explanation of the ion formation, and some general remarks on possible fields of application. It discusses ion motion in radio frequency fields as they are present as well in the ion funnel as in the quadrupole mass filter, and explains the operation of quadrupole mass filters. Influences of the space–charge effect and the theory of scanning tunnelling microscopy will be explained briefly.

Chapter 3 provides a detailed description of the design and construction of the electrospray deposition apparatus, with the design being the major task of my work. At first it gives a quick overview of the experimental setup. After this all important components are described in detail. The properties of the novel ion funnel design are investigated by a numerical method. The functionality of the instrument is documented by a number of different deposition experiments shown in Chapter 4, using large biomolecules as well as small organic molecules and metal–organic compounds.

A condensed version of this thesis has been published in a peer–reviewed journal article:

> Hamann, C., Woltmann, R., Hong, I., Hauptmann, N., Karan, S. & Berndt, R. Ultrahigh vacuum deposition of organic molecules by electrospray ionization. *Review of Scientific Instruments* **82,** 033903 (2011)

1 Design Criteria

The preparation of pure organic molecular layers on atomically flat and clean single crystal surfaces by electrospray deposition is a challenging task, especially concerning the ratio of intentionally deposited particles to unwanted contaminations and reasonable deposition times. Another important point is the suitability of the experimental setup for molecules having masses well above 1000 u, which are especially eligible for the electrospray method.

1.1 Required Ion Current

For Scanning Tunnelling Microscope (STM) experiments typical coverages of the order of ten percent of a monolayer are most useful, as the STM tip can be prepared and characterized on the pristine metal substrate area. If we assume the surface area A to be 30 mm^2, and the area a covered by a molecule carrying a single electric charge to be 3 nm^2, the charge

$$Q = A/a \cdot \mathrm{e} \approx 500\,\mathrm{pAh}$$

is needed for a complete monolayer coverage. To achieve some ten percent of a monolayer within some hours a total charge of roughly 50 pAh is required. This value does of course differ depending on the molecular size and charge state.

Electrospray ion sources usually generate a total ion current of up to 5 nA. Therefore an overall transmission as high as one percent is needed. Skimmer setups [16] commonly used to separate the first chambers in an electrospray mass spectrometer usually have ion transmissions of less than ten percent per stage, not taking the transmission losses of the stages following the skimmer into account. Therefore an ion funnel setup, yielding much higher transmission, is required.

1.2 Ion Beam Filtering

While depositing ions from an electrospray ion source, the sample quality may suffer for a number of reasons, which are directly related to the deposition. First, the particle beam may contain neutral or charged contaminations. In addition, deposited ions may fragment during the adsorption process, for example, when the ions kinetic energy is too high.

To filter charged impurities in a constant current ion beam, the use of a quadrupole mass filter appears most appropriate. Quadrupole mass filters are readily available up to $m/z = 4000$ e/u and higher. In addition, these filters can be operated in a way, that their resolution and transmission are optimized for the particular case.

The use of an electrostatic energy filter will separate charged from neutral particles and allow the adjustment of the mean kinetic energy and its distribution.

1.3 Adaption to LT-STAFM

The most reliable way to preserve high sample qualities is to perform preparation and characterization within the same vacuum system. Each transfer in a transportable container under either vacuum or noble gas atmosphere increases the risk of possible contaminations. To realize the combination of the deposition source with an *Low Temperature Scanning Tunnelling and Atomic Force Microscope* (LT–STAFM) system, two aspects have to be considered. At first the STM is operated on a pressured air damping system and the rigid connection of the deposition source to the STM chamber demands both systems to be mounted on the damping system. This is no drawback in general, because a higher mass on the damping system allows lower frequencies to be damped.

In addition ultra–high vacuum (UHV, $p < 10^{-9}$ mbar) has to be maintained at all times. To achieve high surface qualities during a deposition experiment, the number of residual gas molecules absorbed has to be much smaller than that of ions deposited at the same time. If the sticking coefficient of gas molecules is assumed to be one, at a pressure of 1 mbar the time to cover the sample surface with one molecular layer is approximately 10^{-6} s [17]. Since it usually takes a couple of hours until a sample is completely prepared, a pressure in the range of 10^{-10} mbar or low 10^{-9} mbar is required and process gases with low sticking coefficient, like noble gases, should be favoured.

Because the electrospray ionization process takes place at ambient pressure, the ions have to be guided through a number of differentially pumped vacuum stages, to achieve the required pressure difference of twelve orders of magnitude. In general the pressure can be reduced by a factor of one hundred or one thousand from one vacuum stage to the next, depending on the conductance limiting aperture size and pumping speed, whereby at least four or five differentially pumped stages are necessary.

To achieve UHV heating of the vacuum system above 120°C for two to three days is required prior to sample preparation and characterization. To permit STM measurements, UHV has to be preserved without the use of mechanical pumps. This is only possible if gas leakage through the deposition system can be prevented.

2 Theoretical Principles

In this chapter some basic theoretical principles for the operation of the electrospray deposition source will be given. At first the formation of ions in the electrospray ionization process will be explained and possible fields of application of the electrospray ionization method will be discussed. Section 2.2 describes the guiding of ions in radio frequency fields as they are present, for example, in the ion funnel and quadrupole mass filter. Section 2.3 explains the quadrupole mass filter and some possible operation modes. Finally the space–charge effect and the theory of scanning tunnelling microscopy will be explained briefly in Sections 2.4 and 2.5.

2.1 Electrospray Ionization

The Electrospray Ionization (ESI) technique [18, 19] is a common technique to introduce large and fragile biomolecules into the gas phase because it is known for its low fragmentation ratio. This chapter gives a general overview of the ESI technique [20, 21]. Sections 2.1.1 to 2.1.3 focuses on the basic mechanism of the ion formation in ESI. We explain some design criteria of ESI sources in Section 2.1.4. The types of ions produced by ESI and some possible applications are discussed in Sections 2.1.5 and 2.1.6.

A characteristic feature of ESI is the transfer of ions from solution to the gas phase, making it useful for substances that are non–volatile but soluble and chargeable. The ions are produced at atmospheric pressure and afterwards guided to a high vacuum system (in our case even an ultra–high vacuum system). The ESI technique allows to softly ionize very fragile organic and biological molecules and provides "wings for molecular elephants" [19]. Since ESI provides multiple charged ions, it expands the range of the used mass analysers. Today ESI is one of the most common ionization techniques especially for biological and medical applications.

The mechanism of ion formation in an electrospray can be divided into three steps, the creation of the charged spray consisting of multiply charged droplets, the reduction of the size of the droplets, and the liberation of ions from these droplets. The complete mechanism is illustrated in Figure 2.1.

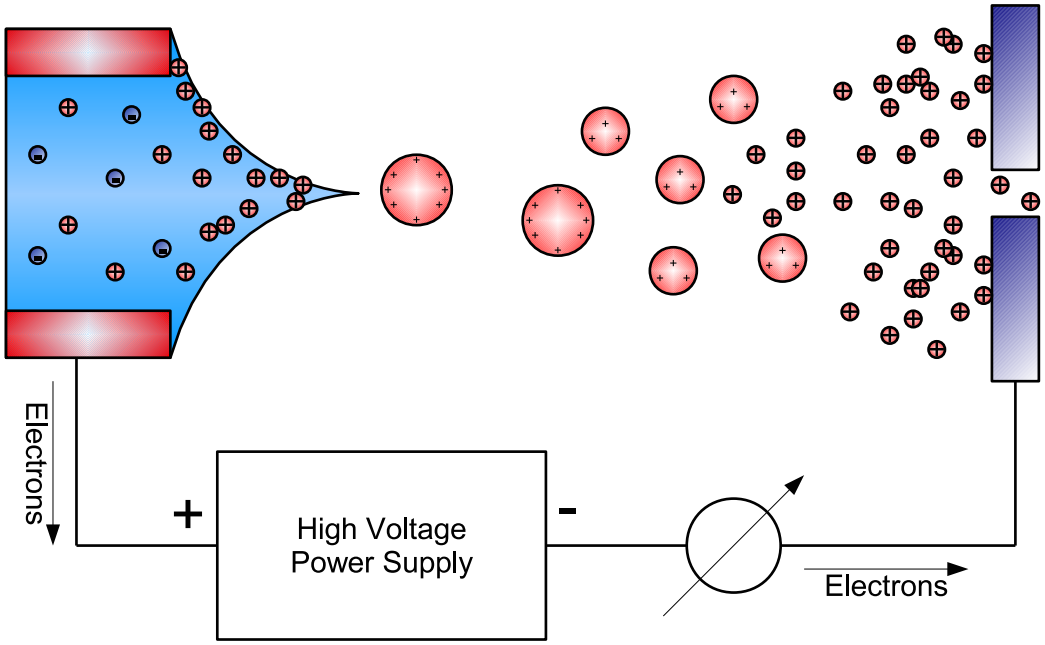

FIGURE 2.1: *Schematic Illustration of the Electrospray Ionization Process.*
A solution containing the analyte is drawn through a metal spray needle (left side) which is kept at a high (in this case positive) voltage potential. The resulting electric field between this needle and the desolvation capillary acting as counter electrode (right side) is penetrating the solution and the dissolved ions move electrophoretically towards the right. The excess of ions of positive polarity attracted by the counter electrode results in the formation of a Taylor cone [22]. At the tip of this cone charged droplets can overcome the surface tension building a fine aerosol. Due to the evaporation of the solvent the droplet size decreases, while the droplet charge is constant, until the Rayleigh limit is reached [23]. At this point much smaller droplets are formed by droplet jet fission [24]. In the end individual ions are formed.

2.1.1 Formation of the Spray

During the electrospray process a solution containing the analyte is guided through a metal spray needle with an inner diameter of 50–100 µm which is kept at a high voltage potential. This needle is facing a desolvation capillary leading inside the vacuum system (compare Figure 2.1). In this condition the electrospray can be formed as described in the following.

If we assume the voltage between the needle and the capillary to be 3 kV and the distance to be approximately 1 cm, then the electric field at the end of the needle can reach 10^6 V/m and penetrates the solution. Due to this high field charges in the liquid are separated. The accumulation of charges at the surface of the liquid is attracted by the capillary, resulting in the formation of a meniscus and finally the so–called *Taylor cone* [22]. At the tip of this cone the electrostatic forces are high enough to overcome the surface tension and liquid can be ejected as a jet, which then breaks into droplets, moving towards the desolvation capillary and forming the spray. Since the charge density is highest at the tip of the cone, these droplets are highly charged.

2.1.2 Droplet Size Reduction

The size of the droplets is in the micrometre range as they are ejected from the Taylor cone. Each of these droplets carries some 10^4 charges distributed over its surface [21]. Due to the evaporation of the solvent the droplet size decreases, while the droplet charge is constant. The charge density on the surface increases until the so–called *Rayleigh limit* is reached [23]. At the Rayleigh limit the electrostatic repulsion exceeds the surface tension. The droplets form two elongated ends to separate charges as much as possible. At the ends of these elongations a number of much smaller droplets with 1-2% of mass but 10-20% of charge are ejected. This process is similar to the liquid ejection at the Taylor cone and called *droplet jet fission* [24].

2.1.3 Liberation of the Ions

The final generation of single ions can be described by the older charge residue model (CRM) [25] or the more recent ion evaporation model (IEM) [26]. There is an ongoing discussion about which is the appropriate ion formation model [27].

The Charge Residue Model

The CRM [25] expects the droplet size reduction (as described above) to continue until the droplet contains just a single analyte ion. The evaporation of solvent molecules continues until the free analyte ion remains. The CRM is especially feasible to explain the formation of large analyte ions with just one or a few charges.

The Ion Evaporation Model

In contrast, the IEM [26] expects the analyte ions to be directly emitted from the droplet under certain conditions. This process requires a critical droplet size to make the electrostatic forces large enough for direct evaporation of the ion. Ion evaporation can only occur if this critical size is larger than the dimension of the ion and the Rayleigh limit. This model is suited to explain the formation of small ions like alkali metal ions, other atomic ions, and salt clusters.

In summary, the CRM appears to be better suited for large molecules, while the IEM only explains the formation of ions from small analytes.

2.1.4 Source Design

The first design sufficient for mass spectrometry was presented by Fenn in the early 1980s [18, 28–31]. The sample solution is introduced to the source from a syringe pump through a needle. This needle is held at a high potential of 3–4 kV relative to a surrounding cylindrical counter electrode. Solvent flow rates are typically of the order of 5–20 µl/min. The formed spray expands into a countercurrent stream of nitrogen gas, which helps to better vaporize the solvent. A small portion of the aerosol enters the desolvation capillary interfacing the atmospheric pressure spray to the first pumping stage. A portion of the beam entering the first pumping stage passes through the orifice of a skimmer [16] to the high vacuum stage, where it is focused into a quadrupole mass analyser.

Since this earliest design, ESI sources have undergone continuous development. A heated desolvation capillary and heated countercurrent gas were employed to improve solvent evaporation [32]. A concentric flow of inert gas around the spray needle in the spray direction allows for flow rates up to ten times higher, and is referred to as *pneumatical assisted* ESI [33]. The formation of the spray can be enforced by an ultrasonic nebulizer for solutions otherwise unsuited for ESI [34]. The development of a nanoelectrospray ion source [32, 35] with sample flow rates of ~ 20 nl/min allows for higher detection efficiencies, the use of buffered solutions and longer signal averaging with the same amount of analyte. The use of different spray geometries like off–axis, orthogonal, or bent paths prevents particles of low or no charge from reaching the capillary's aperture and decreases the amount of impurities in the ion beam.

2.1.5 Ions Produced by an ESI Source

The ions produced in the ESI process are *quasi–molecular ions* in the majority of cases, rather than radical ions. Quasi–molecular ions are not created by electron transfer but by addition or removal of protons (hydrogen ions) or other ions (such

as alkali metal ions). In contrast to radical ions, which possess unpaired electrons, the number of electrons of these ions is usually even. Especially for larger molecules multiple charging can be frequently observed. The observation of different charge states under a characteristic envelope is common. The variety of ions produced of a particular analyte depends on the polarity of the analyte, the used solvent (for example its pH), and the concentrations of salts and other additives.

Non–polar analytes can be considered unsuitable for ESI. If any ions can be found, they are formed by protonation, deprotonation or ion addition (for example alkali metal ions). For ionic analytes the cations C^+ and anions A^- can be formed as well as $[C_n + A_{n-1}]^+$ or $[C_{n-1} + A_n]^-$ ion clusters. Analytes of medium and high polarity exhibit a number of different ions like *exchange ions* formed by the exchange of hydrogen and alkali atoms, clusters, and adducts containing solvent molecules.

2.1.6 Fields of Application

The ESI technique is suitable for many different classes of molecules. It is widely used for studying peptides and proteins. Small molecules ($m < 1500$ u) are investigated by ESI especially for pharmaceutical and metabolism studies. For oligonucleotides of more than twenty nucleotides ionization by MALDI (Matrix Assisted Laser Desorption / Ionization) becomes difficult and ESI is better suited to ionize larger oligonucleotides, DNA, and RNA [36–38]. Also determining the nucleotide order of DNA (DNA sequencing) is possible this way [36, 38]. A remaining problem for this special application is the exchange of hydrogen atoms by alkali metals, which can be solved by adding nitrogen bases [39]. The molecular weight and structure of oligosaccharides and related compounds can be determined by ESI [40]. Another possibility is the application to metal complexes that are soluble in suitable solvents [41, 42].

The mass to charge ratio of ions produced by ESI is normally less than 3000 u/e since the ions produced are multiple charged. This makes ESI suited for quadrupole mass filters application, because modern quadrupole instruments cover an m/z range of up to 4000 u/e.

2.2 Guiding of Charged Particles by Radio Frequency Fields

As a direct consequence of Laplace's equation in a charge–free domain $\Delta\Phi = 0$, an equilibrium of the electrostatic potential is always unstable and consequently electrostatic potentials are unfavourable for trapping ions. This situation is worsened by space charge and other distortions. In contrast the effective potential of RF electric fields allows three dimensional potential minima. It is used in a number of devices handling gas phase ions, such as quadrupole mass filters, paul traps, multipole ion guides, ring electrode traps, ion funnels and others.

The description of their theoretical principles presented in this section is inspired by the detailed review of Dieter Gerlich in Reference [43]. At first an effective potential will be derived within the so–called adiabatic approximation. The effective potential explains the motion of charged particles for a number of applications, especially for the ion funnel and the low–mass band pass operation of the quadrupole mass filter. This operation mode is the most favourable for a soft ion deposition.

2.2.1 The Adiabatic Approximation

The *adiabatic approximation* [43] can be used to describe the motion of charged particles in radio frequency fields under certain conditions. Within this approximation the total energy of the ion can be shown to be constant if an additional potential, the so–called *effective potential*, is introduced and it is not influenced by the oscillatory motion in the radio frequency field. We will describe the motion of charged particles in oscillatory electric fields, find an approximate analytical solution, introduce the effective potential and discuss the validity of the adiabatic approximation within this section.

Equation of Motion

To describe the movement of a classical particle of charge q and mass m in an external electric field[1] $\mathbf{E}(\mathbf{r}, t)$ the equation of motion can be written as

$$m\ddot{\mathbf{r}} = q\mathbf{E}(\mathbf{r}, t). \tag{2.1}$$

This equation will be simplified to allow an approximate solution within certain constraints, because a general analytical solution only exists for some special field geometries. We assume the electric field $\mathbf{E}(\mathbf{r}, t)$ to be composed of a static, $\mathbf{E}_s(\mathbf{r})$, and

[1] Because we deal with particle velocities much lower than the velocity of light the magnetic part of the oscillatory electromagnetic field is disregarded. Stationary magnetic fields are excluded as well.

a time–dependent part, $\mathbf{E}_0(\mathbf{r})\cos(\omega t+\delta)$, with amplitude $\mathbf{E}_0(\mathbf{r})$, angular frequency $\omega = 2\pi f$, and phase δ. Equation (2.1) simplifies to

$$m\ddot{\mathbf{r}} = q\mathbf{E}_0(\mathbf{r})\cos(\omega t+\delta) + q\mathbf{E}_s(\mathbf{r}). \tag{2.2}$$

The phase δ can be eliminated by a shift of the time axis, and as a first consideration we assume the static field $\mathbf{E}_s(\mathbf{r})$ to be zero. In case of a charged particle in a homogeneous radio frequency field $\mathbf{E}(t)$ (parallel plate capacitor) Equation (2.2) can be solved directly. The solution is a harmonic oscillation

$$\mathbf{r}(t) = \mathbf{r}(0) - \mathbf{A}\cos(\omega t) \tag{2.3}$$

with the amplitude

$$\mathbf{A} = q\mathbf{E}_0/m\omega^2. \tag{2.4}$$

On average the particle's position does not change.

In weakly inhomogeneous fields, the amplitude $\mathbf{A}$ is almost the same, but the particle experiences an apparent force toward lower field strength because of the varying field strength during one oscillation. In general, the corresponding differential equation has to be solved numerically and the particle trajectories can be complex.

Effective Potential

To describe the motion of charged particles in inhomogeneous radio frequency fields, an analytical approximation of the solution of Equation (2.2) is now derived.

If we assume the frequency ω to be high and variations of the electric field as a function of coordinates $\mathbf{r}$ to be small, the amplitude $\mathbf{A}$ in Equation (2.4) is expected to be small and vary only slowly due to motion along $\mathbf{r}$. These assumptions will be discussed in detail in the section **Adiabaticity and Stability** on Page 15. In this case we expect the particle motion to be a superposition of a drift term $\mathbf{R}_0(t)$ and a radio frequency oscillatory motion $\mathbf{R}_1(t) = -\mathbf{A}\left(\mathbf{R}_0(t)\right)\cos\omega t$ around the mean position $\mathbf{R}_0(t)$ with an amplitude $\mathbf{A}\left(\mathbf{R}_0(t)\right)$ as calculated in Equation (2.4):

$$\mathbf{r}(t) = \mathbf{R}_0(t) - \mathbf{A}\left(\mathbf{R}_0(t)\right)\cos\omega t. \tag{2.5}$$

Due to the assumption of small $\nabla\mathbf{E}_0$, $\mathbf{E}_0$ can be estimated by its second order expansion at $\mathbf{r} = \mathbf{R}_0$

$$\begin{aligned}\mathbf{E}_0(\mathbf{r}) &= \mathbf{E}_0\left(\mathbf{R}_0 - \mathbf{A}(\mathbf{R}_0)\cos\omega t\right)\\ &= \mathbf{E}_0(\mathbf{R}_0) - \left(\mathbf{A}(\mathbf{R}_0)\cdot\nabla\right)\mathbf{E}_0(\mathbf{R}_0)\cos\omega t + \mathcal{O}\left((\mathbf{r}-\mathbf{R}_0)^2\right).\end{aligned} \tag{2.6}$$

From substituting Equations (2.5) and (2.5) into Equation (2.2), in the case of the

static field $\mathbf{E}_S$ being zero, it follows that

$$m\ddot{\mathbf{R}}_0 + m\omega^2\mathbf{A}\cos\omega t = q\mathbf{E}_0(\mathbf{R}_0)\cos\omega t - q\left(\mathbf{A}(t)\cdot\nabla\right)\mathbf{E}_0(\mathbf{R}_0)\cos^2\omega t. \tag{2.7}$$

Considering Equation (2.4) the $\cos\omega t$ terms in Equation (2.7) can be canceled. For quasistatic electric fields (typical length $L \ll \frac{2\pi}{\omega}c$) we can use the relation

$$(\mathbf{E}_0\cdot\nabla)\mathbf{E}_0 = \tfrac{1}{2}\nabla\mathbf{E}_0^2 - \mathbf{E}_0\times(\nabla\times\mathbf{E}_0) \approx \tfrac{1}{2}\nabla E_0^2, \tag{2.8}$$

because $\nabla\times\mathbf{E}_0 \approx 0$ and after averaging $\cos^2\omega t$ over time the differential equation for the non–oscillating part of motion

$$m\ddot{\mathbf{R}}_0 = -\frac{q^2}{4m\omega^2}\nabla E_0^2 \tag{2.9}$$

can be found. In time average a force pushes charged particles of both polarities towards regions of lower field strength.

By taking the electrostatic force $q\mathbf{E}_s(\mathbf{r})$ from Equation (2.2) into account again, as the negative gradient of the electrostatic potential Φ_s, the so–called *radio frequency pseudopotential*

$$qV^*(\mathbf{R}_0) = q^2E_0^2/4m\omega^2 + q\Phi_s \tag{2.10}$$

can be expressed, simplifying the equation of motion for the smoothed trajectories, to

$$m\ddot{\mathbf{R}}_0 = -\nabla V^*(\mathbf{R}_0). \tag{2.11}$$

This *radio frequency pseudopotential* is also known as *effective potential*, *high-frequency potential*, or *quasipotential*.

The time–averaged kinetic energy of the oscillatory motion can be calculated from Equations (2.4) and (2.5) to be

$$\left\langle \frac{1}{2}m\dot{\mathbf{R}}_1^2 \right\rangle = q^2E_0^2/4m\omega^2, \tag{2.12}$$

the *effective potential energy*.

Integration of Equation (2.11) leads to the total energy E_m

$$\frac{1}{2}m\dot{\mathbf{R}}_0^2 + \left\langle \frac{1}{2}m\dot{\mathbf{R}}_1^2 \right\rangle + q\Phi_s = E_m, \tag{2.13}$$

an adiabatic constant of the ion motion.

A well known example illustrating this result is the operation of a quadrupole mass filter as a low–mass band filter as described in the section **Low–Mass Band Pass** on Page 20.

Adiabaticity and Stability

The presented derivation of the effective potential results in a constant total energy of the ion. The assumption made to derive this result will be discussed in this section.

The system described by Equation (2.2) does not need to be conservative, and the oscillating force on the particle can result in continuous augmentation of kinetic energy. In the following some general conditions for adiabaticity and stability will be presented.

In the literature [43–45] the characteristic parameter is derived from the assumption of small $\nabla \mathbf{E}_0$, that is justifying the approximation of $\mathbf{E}_0$ by its second order expansion (compare Equation (2.5)). Therefore, it can be demanded that over the full distance of the oscillation $2\mathbf{A}$ the change of the electric field ∇E_0 is much smaller than the field E_0 itself.

$$|2\,(\mathbf{A}\,\cdot\,\nabla)\,\mathbf{E}_0| < |\mathbf{E}_0|$$

The characteristic parameter η can now be defined as

$$\eta = |2\,(\mathbf{A}\,\cdot\,\nabla)\,\mathbf{E}_0| \,/\, |\mathbf{E}_0|\,,$$

which can be converted to

$$\eta = 2q\,|\nabla E_0| \,/ m\omega^2 \tag{2.14}$$

by using Equations (2.4) and (2.8).

Because $|\nabla E_0|$ is a function of $\mathbf{r}$, $\eta(\mathbf{r})$ must be known for each point along the ion trajectory. Empirical results [44, 46] and simulations [43] have shown, that

$$\eta < 0.3 \tag{2.15}$$

is sufficient to ensure adiabaticity.

In general, it is not easy to determine whether the motion of an ion in an RF field is stable. If the adiabatic approximation (Equation (2.15)) is fulfilled, it is sufficient to postulate the total ion energy E_m (Equation (2.13)) to be low enough to prevent the ion from crossing the boundary $\mathbf{r}_m$ of the allowed region inside the electrode assembly. A stability condition can therefore be formulated as

$$V^*(\mathbf{r}_m) > E_m. \tag{2.16}$$

However these conditions are not absolutely necessary. Stable trajectories, which may be rather complicated, can exist outside the validity of the adiabatic approximation. A well known example is the default operation of quadrupole mass filters close to the point $(q, a = 0.706, 0.236)$ of the Mathieu stability diagram (region **A** in Figure 2.2) as described in Section 2.3.

Buffer Gas

If an ion of mass M and scattering cross section σ is moving in a radio frequency (RF) field in a buffer gas of molecular mass m, the number density of the gas n influences the efficiency of the field in guiding the ions towards regions of lower field strength. At higher pressures hundreds of collisions per oscillation period can reduce the effect of the RF–field. The decrease of the oscillation amplitude of the ion and a change of the phase dependence between the RF–field and the oscillation of the ion result in a rescaling of the effective potential by a coefficient γ. The result of the calculation of the coefficient γ, as given in detail in Reference [47], is

$$\gamma = \frac{\omega^2\tau^2}{1+\omega^2\tau^2}$$

with ω being the angular frequency of the RF–field and $\tau = \frac{3(m+M)}{4m} t_{col}$ the relaxation time of the damping. The time between two collisions $t_{col} = 1/n\sigma v$ depends on the buffer gas molecules' mean speed $v = \sqrt{\frac{8kT}{\pi m}}$.

2.3 The Quadrupole Mass Filter

In this section a summary of the theory of quadrupole mass filters will be given. The equation of motion of ions inside the quadrupole will be derived and stable solutions will be presented. Three different modes of operation of the quadrupole mass filter will be explained, which are the RF–only mode, the low–mass band pass operation and the most common mass resolving mode. The applicability of these modes to deposition experiments will be discussed.

An ideal quadrupole mass filter [48, 49] consists of four hyperbolically shaped rod electrodes in a square configuration. Each diagonally opposing rod pair is held at the same potential and a direct current (DC) voltage U superimposed with a radio frequency (RF) voltage V with the frequency ω is applied between the two rod pairs.

Because their field geometry is very special, the theoretical principles of linear quadrupoles have been discussed and reviewed in detail in literature [50, 51]. The equations of motion perpendicular to the quadrupole axis can be reduced into two decoupled, one–dimensional differential equations in x– and y–direction. Stable solutions do not depend on the ions initial conditions and can be displayed in a two dimensional stability diagram.

An ion of mass m and charge q entering the quadrupole assembly parallel to the rods (z–direction) is attracted by one of the rods with its charge momentarily opposite to the ionic charge. Since the applied voltage is periodic in time the ion starts an oscillatory motion in both x– and y–directions.

The electric potential inside the quadrupole is

$$\Phi_0 = (U + V\cos\omega t) \cdot \frac{x^2 - y^2}{r_0^2} \tag{2.17}$$

with r_0 being the rods' distance to the quadrupoles axis, resulting in the following equations of motion:

$$\frac{\mathrm{d}^2x}{\mathrm{d}t^2} + \frac{q}{m_i r_0^2}(U + V\cos\omega t)\,x = 0 \tag{2.18}$$

$$\frac{\mathrm{d}^2y}{\mathrm{d}t^2} - \frac{q}{m_i r_0^2}(U + V\cos\omega t)\,y = 0. \tag{2.19}$$

By substituting the dimensionless parameters

$$a_x = -a_y = \frac{4qU}{m_i r_0^2\omega^2},\ q_x = -q_y = \frac{2qV}{m_i r_0^2\omega^2} \text{ and } \tau = \frac{\omega t}{2}, \tag{2.20}$$

Equations (2.18) and (2.19) can be converted to the dimensionless Mathieu's differ-

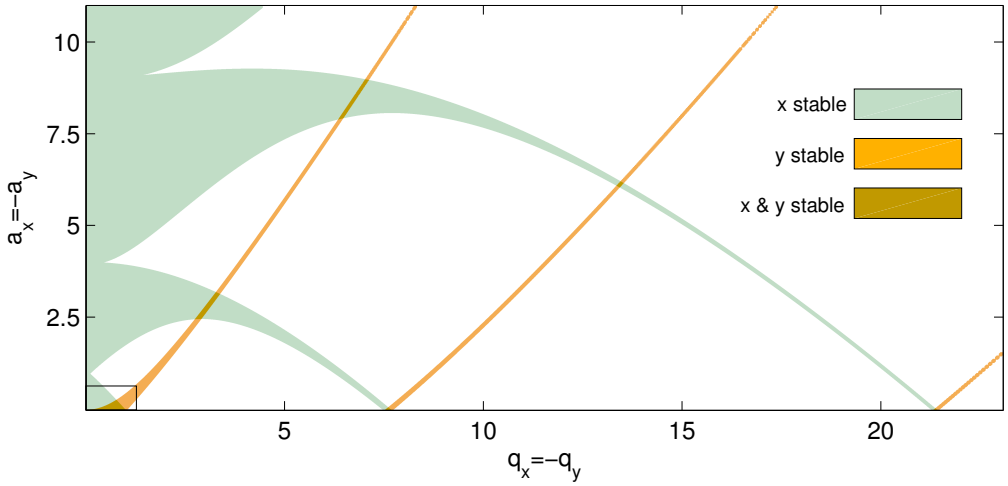

FIGURE 2.2: *First Quadrant of the Mathieu Stability Diagram.*
Regions of stability for a linear quadupole analyser for x– and y–motion are marked in green and yellow, shown by a plot of $a_x = -a_y$ versus $q_x = -q_y$ (see Equation (2.20)). Regions of simultaneous overlap are coloured brown, the marked region corresponds to the traditional quadrupole mass filter operation (compare also Figure 2.3). Regions of stability were computed using a recursion formula as proposed in References [52, 53].

ential equation

$$\frac{\mathrm{d}^2 x}{\mathrm{d}\tau^2} + (a_x + 2q_x \cos 2\tau)\, x = 0 \tag{2.21}$$

$$\frac{\mathrm{d}^2 y}{\mathrm{d}\tau^2} + (a_y + 2q_y \cos 2\tau)\, y = 0. \tag{2.22}$$

For some values of U, V and ω the solutions of this equation can result in stable ion trajectories through the quadrupole with limited amplitudes in the xy–plane for specific m/z–ratios. Plotting $a_x = -a_y$ versus $q_x = -q_y$ results in the Mathieu stability diagram (Figure 2.2), revealing regions of stability in x– and y–motion that partly overlap. The marked region in Figure 2.2 corresponds to the traditional mass–separating mode of the quadrupole mass filter and an expanded view of this region can be found in Figure 2.3. Some useful formulas for the common mass filter operation can be found on Page 23. In the following some operation modes of the quadrupole mass filter will be explained.

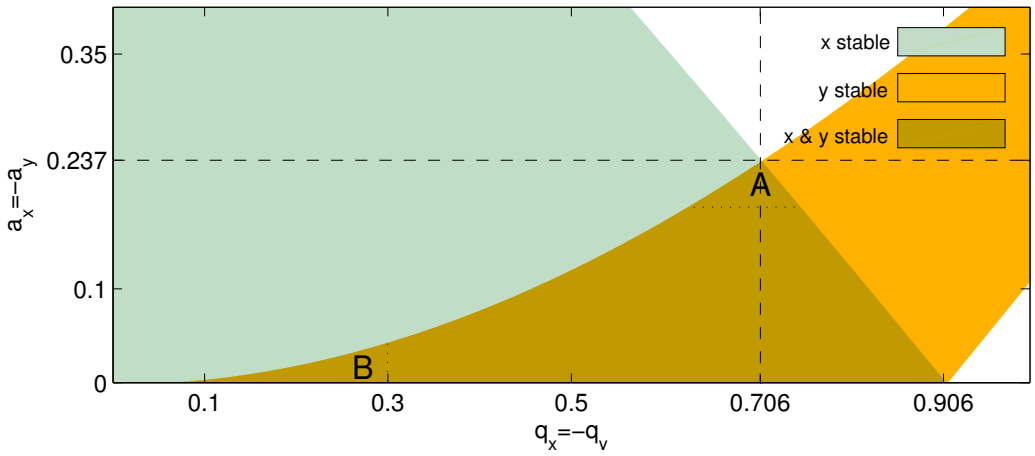

FIGURE 2.3: *Expanded View of the Mathieu Stability Diagram.*
The quadrupole mass analyser is operated in region A *for common mass scans and in region* B *to operate as a low–mass band pass as described on Page 20.*

2.3.1 Constant Resolution and Unit Mass Resolution Scans

To perform a *constant resolution mass scan* ($m/\Delta m$ is constant), the voltages U and V have to be varied simultaneously at a constant ratio, so as to keep a_x and q_x in the region A of Figure 2.3 close to $a_x = 0.237$ and $q_x = 0.706$ (compare also Page 23). This scan mode is illustrated by the upper –high resolution– scan line in Figure 2.4. As the voltages are varied they cross the regions of stability of different masses. To decrease the resolution and incresae the transmission, the ratio U/V is lowered and the scanline passes through a wider portion of the areas of stability. Because of the characteristic shape of the stability diagram, the peaks leading edge moves three times faster towards lower apparent mass than the trailing edge to higher apparent mass, as the resolution is decreased. This fact results in an apparent shift of the mass peaks center position.

To perform a *unit mass resolution scan* (Δm is constant) the ratio of U to V cannot be constant but must increase with increasing mass (compare Page 23). Let us treat U as a function of V. In the analog hardware, the nonlinear increase of U is approximated by lowering the intercept and raising the slope in a way that unit mass resolution is achived for a light and heavy calibration mass. In the Extrel systems, the intercept, primarily affecting low mass resolution, is called ΔM, and the slope, primarily affecting high mass resolution, is called ΔRes.

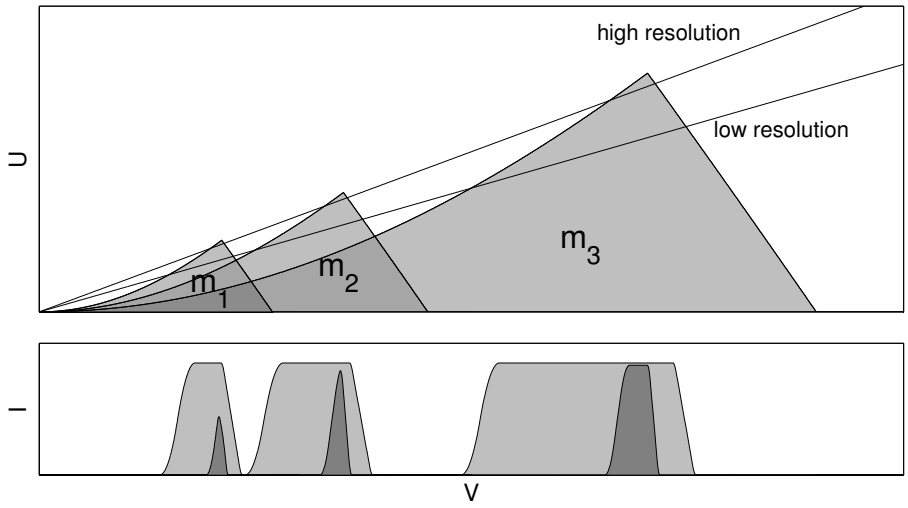

FIGURE 2.4: *Constant Resolution Mass Scan.*
In a stability diagram of the DC voltage U versus the RF voltage U each mass (here m_1, m_2, and m_3) has a different region of stability. Scanning V and U along a line leads to a constant resolution mass spectrum as shown in the lower part of the figure, where the Intensity I is plotted versus the RF voltage V. The peak broadening at lower resolution is assymetric.

Note: The quadrupole analyser installed in the described instrument has a rod diameter R of 9.5 mm ($R/r_0 = 1.148$) and a length of 200 mm. Two oszillators at $f = \omega/2\pi = 880$ kHz and 1.2 MHz result in a mass to charge range of 4000 u/e and 2000 u/e at a DC voltage U of ± 200 V and a RF amplitude V of 7.2 kV.

2.3.2 Low–Mass Band Pass

Another application of operating a quadrupole is to use it as a low–mass band pass at low q_x values. By comparing Equations (2.14) and (2.20) it can be shown, that the parameters q_x and η are identical for the quadrupole field. To fulfil the adiabatic approximation q_x has to be restricted to $q_x < 0.3$ (region B) in Figure 2.3; sometimes a restriction to $q_x < 0.4$ was found to be sufficient to describe the quadrupole using the effective potential as well [50, 51].

The effective potential can be derived direcly by inserting the quadrupoles electrostatic potential

$$\Phi_s = U_0 \cdot (x^2 - y^2)/r_0^2$$

and the time dependent part of the electrical field

$$E_0 = -\nabla\Phi_t = -\frac{2V_0(x\mathbf{e}_x - y\mathbf{e}_y)}{r_0^2}$$

into Equation (2.10).

The result

$$V^*(x,y) = \frac{q^2 4V_0^2(x^2+y^2)}{4m\omega^2 r_0^4} + qU_0(x^2-y^2)/r_0^2$$

can be converted to polar coordinates

$$V^*(r,\phi) = \frac{q^2 4V_0^2 r^2}{4m\omega^2 r_0^4} + \frac{qU_0(r^2\cos 2\phi)}{r_0^2}.$$

To ensure that ions starting at the quadrupole axis (r=0) are not attracted by the quadrupole rods at the distance r_0 to the axis, the effective potential has to be repulsive for $r = r_0$ and for all ϕ. This condition results in a mass cut–off of

$$m < qV_0^2/(\omega^2 r_0^2 U_0).$$

An important advantage of the operation mode, especially for deposition experiments, is the ensured conservation of kinetic energy.

2.3.3 RF–Only Mode

For a long time quadrupole mass filters were supposed to discriminate against higher masses, because higher masses require a higher mass resolution $m/\Delta m$ resulting in a lower transmission (compare Page 23). A way to increase the transmission of quadrupole mass filters for high masses by simply changing the applied voltages was identified in the 1970's. A detailed explanation can be found in References [54–56]. Normaly a quadrupole operated without a resolving DC voltage applied ($a_x = 0$ in the Mathieu stability diagram) acts as a high mass pass filter, because each ion that fulfils the condition $q_x \leq 0.906$ can be transmitted, which corresponds to a lowest mass of

$$(m/z)_{min} = \frac{1}{0.906}\frac{2V}{r_0^2\omega^2}.$$

The transversal kinetic energy gain of the ions was found to increase exponentially with the adiabaticity parameter η. This can be used for filtering ions at the $q_x = 0.906$ edge of the stability diagram in two different ways. One way is to simply apply a repulsive voltage to the exit lens of the quadrupole. Transversal kinetic energy is partially converted to parallel kinetic energy by the fringe field between the quadrupole rods and the exit lens, allowing just the ions of the desired mass to pass. Another way is to conserve the transversal kinetic energy and filter ions

that gained less energy by blocking ions close to the axis in a lens assembly behind the quadrupole. The high mass transmission in this operation mode was found to be ten times higher compared to the common mode of operation at the same mass resolution [54].

For deposition experiments the low–mass band pass mode should be used if possible. This mode requires the abscence of impurities of lower masses than the substance of interest, but ensures the conservation of kinetic energy as the adiabatic approximation is fulfilled. If this mode is not applicable the common mass resolving mode should be used and the resolution should be set in a way to filter all impurities but maximize transmission.

On this page, some useful equations for common quadrupole mass–filter operation are given as presented in Reference [57], with r_0 being the distance of the rods to the quadrupole axis and U and V the DC and RF voltage, respectively:

- mass resolution:

$$\frac{m}{\Delta m} = \frac{0.126}{0.16731 - U/V}$$

  full width for trapezoid peakshape / low resolution

$$\frac{m}{\Delta m} = \frac{0.252}{0.16731 - U/V}$$

  half width for triangular peakshape / high resolution

- transmission:

$$T = 100\%$$

  for trapezoid peakshape / low resolution

$$T \propto \frac{\Delta m}{m}$$

  for triangular peakshape / high resolution

- ideal aperture:

$$\Phi \approx \frac{r_0}{\sqrt{m/\Delta m}}$$

- maximum radial kinetic energy:

$$U_r \approx \frac{V}{15 \cdot (m/\Delta m)}$$

- apparent mass setting for resolving RF–only mode:

$$m_{RF-only} = 1.28 \times m_{RF-DC}$$

2.4 The Space–Charge Effect

The spatial electric charge distribution, caused by an excess of positive or negative charge carriers, treated as a continuum of charge instead of point–like charges, is called *space–charge*. Space–charge effects can play an important role in electron and ion sources, as they may degrade beam characteristics, such as intensity, focus size or energy resolution. To estimate whether the space–charge effect has an influence in the presented experiments, a simplified model will be presented as first introduced in Reference [58].

We assume the ion beam to be laminar, to have a continuous charge distribution and to be non–relativistic ($F_{el} \gg F_{mag}$). The radial electric field at the border ($r = R$) of the ion beam of the charge density ρ can be determined using Gauss's law to be

$$E(R) = \frac{\rho R}{2\epsilon_0}.$$

The Coulomb force acting on a single charge at the border of the beam

$$\vec{F} = q\vec{E}$$

leads to the equation of motion

$$m \cdot \frac{\mathrm{d}^2 R}{\mathrm{d}t^2} = \frac{qjR}{2\epsilon_0 v}$$

with the current density $j = \rho v$. Now we perform the substitutions

$$U = \frac{mv^2}{2q},$$

implying the kinetic energy of the ions to be only caused by a voltage U, and

$$I = \pi R^2 j$$

as the total ion current. We define the *perveance* K

$$K = \frac{I}{U^{3/2}} = \frac{\pi R^2 j}{U^{3/2}},$$

use the abbreviation

$$K_0 = 2\pi\epsilon_0 \cdot \sqrt{\frac{2q}{m}} = 0.77 \times 10^{-6} \, \frac{\mathrm{A}}{\mathrm{V}^{3/2}} \cdot \sqrt{\frac{q}{m}} \sqrt{\frac{\mathrm{u}}{\mathrm{e}}} \tag{2.23}$$

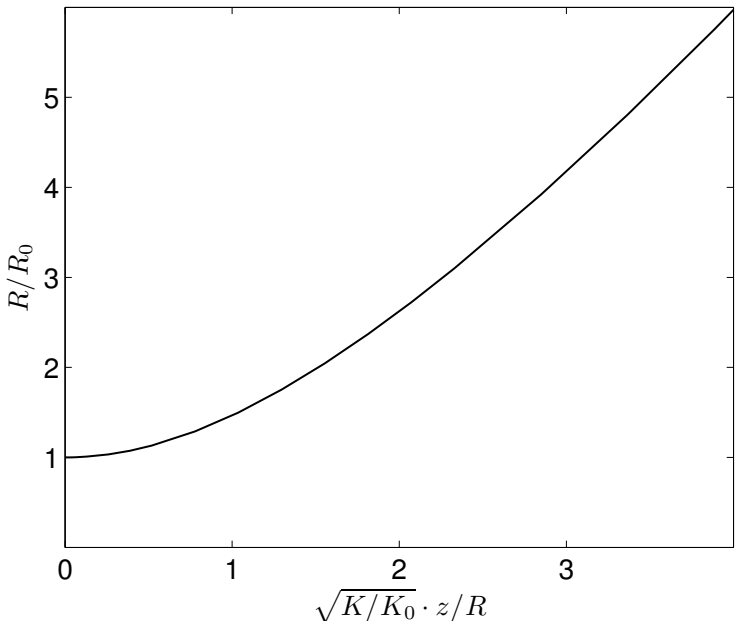

FIGURE 2.5: *Space–Charge induced Ion Beam Divergence.*
Development of the ion beam radius $R(z)$ of a parallel ion beam starting at $z = 0$ diverging due to space–charge repulsion. For explanation of K and K_0 see text.

as *characteristic constant* K_0 and change the derivative to be with respect to z

$$\frac{\mathrm{d}}{\mathrm{d}t} = v\frac{\mathrm{d}}{\mathrm{d}z}.$$

The ordinary differential equation

$$\frac{\mathrm{d}^2R}{\mathrm{d}z^2} = \frac{K}{K_0} \cdot 1/R \tag{2.24}$$

describes the development of the beam radius. It was solved using MATLAB's integrated Adams–Bashforth–Moulton PECE solver [59] and the result is shown in Figure 2.5.

To estimate the influence of the space–charge effect, we calculate K and K_0 for some typical values of I, U and m/q:

$$K = \frac{I}{U^{3/2}} \approx \frac{100\,\mathrm{pA}}{(10\,\mathrm{V})^{3/2}} \approx 3 \times 10^{-12}\,\frac{\mathrm{A}}{\mathrm{V}^{3/2}} \tag{2.25}$$

$$K_0 \approx 0.77 \times 10^{-6} \frac{\mathrm{A}}{\mathrm{V}^{3/2}} \cdot \sqrt{\frac{1}{1000}} \approx 2.5 \times 10^{-8} \frac{\mathrm{A}}{\mathrm{V}^{3/2}} \tag{2.26}$$

resulting in

$$\sqrt{K/K_0} \approx \frac{1}{100}. \tag{2.27}$$

According to Figure 2.5 the ion beam will thus expand, for example, from 1 mm to approximatly 6 mm after passing the vacuum chamber housing the quadrupole deflector, passing a distance of approximately 400 mm. To avoid this expansion the ion beam is widened by means of a pair of lenses between the conductance limiting apertures and ion optical devices as illustrated in Figure 3.13.

While performing the calculations of the ion funnel transmission in Section 3.4.1 the space–charge effect was neglected completely. In [60, 61] the maximum transmittable ion current was estimated by equating the focusing force of the effective potential and the defocusing force, due to the space–charge effect, on an ion at the border of the ion beam. The result is a maximum ion current of

$$I_{max} = \pi^4 \epsilon_0 \tau \rho E_z \left(\frac{q}{m}\right)^2 \frac{V_{rf}^2}{\omega^2 d^3}. \tag{2.28}$$

The estimated maximum current can be in the order of some hundred nA in our case, although the formula is not strictly correct because the condition $d \ll \rho$ is not fulfilled.

2.5 Scanning Tunnelling Microscopy and Spectroscopy

Scanning Tunnelling Microscopy (STM, also Scanning Tunnelling Microscope) delivers topographical pictures of solid surfaces with atomic resolution [62]. These pictures are obtained by moving a small tip across the surface at a distance Z of just some Ångströms, applying the tunnelling voltage V_S to the surface, and measuring the tunnelling current I. The tunnelling current is caused by a quantum mechanical phenomenon, the so–called *quantum tunnelling*, where particles are allowed to pass through a barrier they could not surmount classically (in this case electrons passing the vacuum–barrier). The precise positioning of the tip with respect to the sample surface is accomplished by piezoelectric actuators.

To measure the topography of a surface, the STM can be operated in two different modes, the so–called *constant height mode* and *constant current mode*. In the constant height mode, the tip is scanning above the surface in one plane, and the dependence of the current on the position is measured. In the constant current mode, an electronic *feedback loop* is regulating the height of the tip in a way to keep the tunnelling current constant and the dependence of the height on the position yields the surface's topography.

In the semiclassical Wentzel–Kramers–Brillouin (WKB) method the tunnelling current is approximated to be

$$I = \int_0^{eV} \rho_S(\mathbf{r}, E)\rho_T(E - eV_S)T(Z, V_S, E)dE \tag{2.29}$$

for low temperatures, with $T(Z, V_S, E)$ being the transmission probability, $\rho_T(E)$ the density of states (DOS) of the tip, and

$$\rho_S(\mathbf{r}, E) = \sum_\nu |\Psi_n(r)|^2 \delta(E_\nu - E)$$

the local density of states (LDOS) of the sample [63–66]. The electron tunnelling transition probability T of a trapezoidal barrier can be estimated to be

$$T(Z, V_S, E) = \exp\left(-\frac{2Z\sqrt{2m}}{\hbar}\sqrt{\frac{\Phi_S + \Phi_T}{2} + \frac{eV_S}{2} - E}\right) \tag{2.30}$$

with Φ_S and Φ_T being the work function of the sample and tip respectively [67].

To gain qualitative information of the energetic distribution of occupied and unoccupied states of the sample surface, the differential conductance $\mathrm{d}I/\mathrm{d}V_S$ is measured as a function of the tunnelling voltage V_S [68]. This mode of operation of an STM is referred to as *Scanning Tunnelling Spectroscopy* (STS). Basically the differential conductance can be measured in two different modes as well, either in the *constant height mode*, where the tip–sample distance is fixed, or in the *constant current mode*, where

the feedback loop regulates the current by changing the tip–sample distance. Under the assumption of the DOS of the tip being constant we estimate the differential conductance to be

$$\frac{\mathrm{d}I}{\mathrm{d}V_S} \propto \rho_S(\mathbf{r}, eV_S)T(Z, V_S, eV_S).$$

A qualitative picture of the sample's LDOS can be obtained directly from the differential conductance by the application of an adequate normalization procedure, for example, by dividing the differential conductance by the conductance as proposed in Reference [69]. A more complete explanation of the STM and STS techniques can be found for example in the References [63, 70–72].

3 Experimental Setup

An essential part of this thesis was the design and assembly of the described electrospray deposition experiment. In addition, a *low–temperature scanning tunnelling and atomic force microscope* (LT–STAFM) was purchased and both setups were adapted to one another. A rough overview of the instrument design is given in Section 3.1. In Sections 3.2 to 3.9, the different components of the deposition setup are described in detail. In Section 3.10, we describe the interface of the deposition setup and the LT–STAFM setup as well as the preparation chamber.

3.1 Overview

The electrospray deposition apparatus (Figure 3.1) is directly attached to a cryogenic scanning tunnelling and atomic force microscope (LT–STAFM) system so as to carry out the deposition and characterize the treated surface without breaking the ultra–high vacuum while the ion formation takes place at ambient pressure. To bridge the pressure gap of twelve orders of magnitude, five differential pumped vacuum chambers were installed.

To guide and purify the ion beam several ion optical devices are used. A two stage radio frequency ion funnel (Figure 3.1(b) and (c)) accomplishes high transmission from the ion source (Figure 3.1(a)) to the molecular flow regime. Beam purification is done in two levels. At first neutral contaminations are rejected by an electrostatic quadrupole deflector (Quadrupole Deflector / Energy Filter, Extrel CMS, Figure 3.1(d)). Afterwards charged particles are filtered by a 9.5 mm quadrupole mass spectrometer (9.5 mm (3/8 inch) diameter quadrupole mass filter assembly, Extrel CMS, Figure 3.1(e)).

Finally the ion beam is conducted to the sample in the deposition stage (Figure 3.1(f)). An Extrel Merlin Automation 5221 Series Scan and Resolution Controller is used to operate the complete instrument. The key components will be described in more detail below.

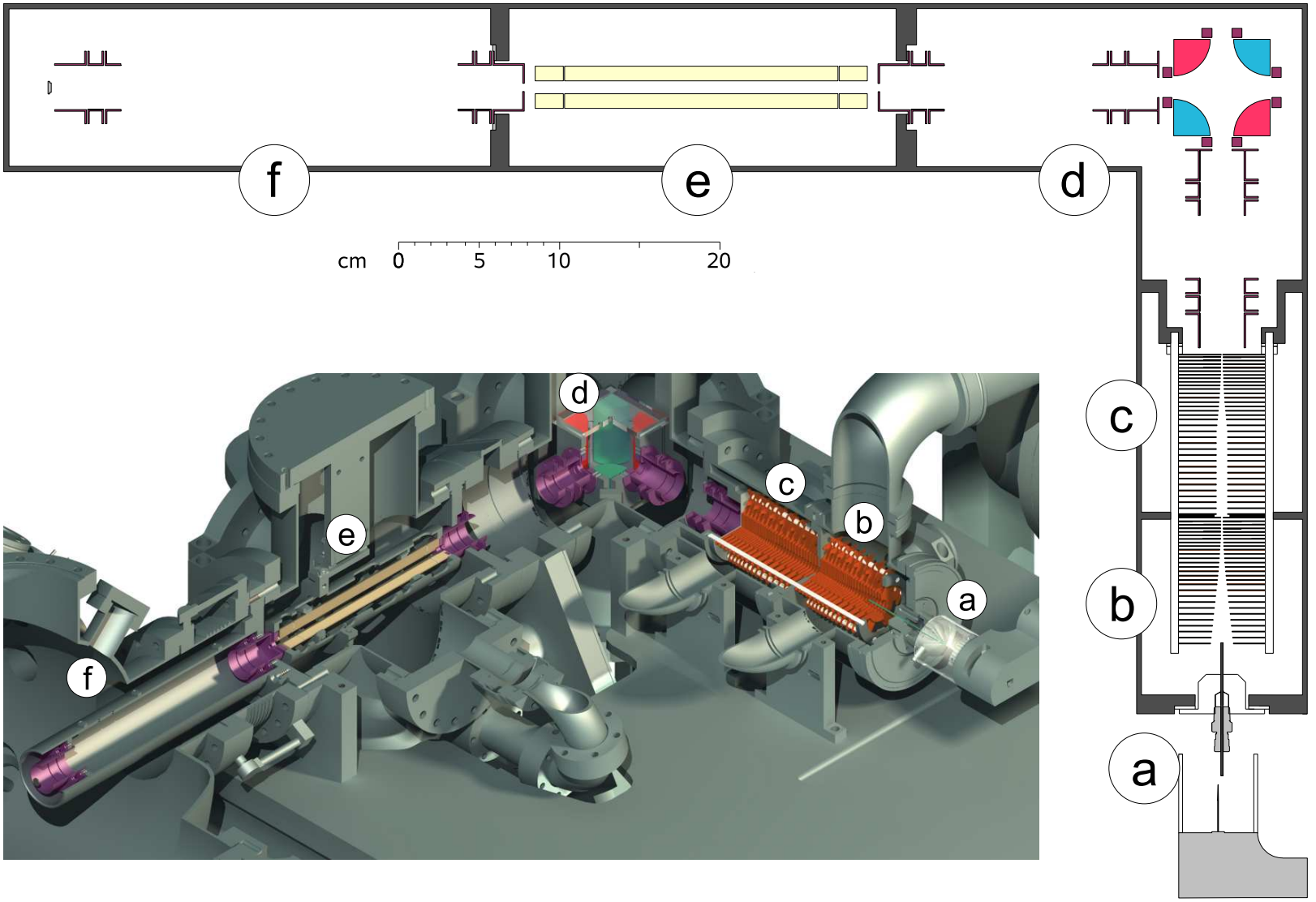

FIGURE 3.1: *Electrospray Ionization Deposition Instrument.*
(a) Ambient pressure electrospray ion source; (b) and (c) two stage radio frequency ion funnel for high ion transmission in the viscous flow regime ($p_1 \approx 0.8\,\mathrm{mbar}$, $p_2 \approx 3.5 \times 10^{-2}\,\mathrm{mbar}$); (d) electrostatic quadrupole deflector for separation of charged particles and energy filtering ($p_3 \approx 1 \times 10^{-5}\,\mathrm{mbar}$); (e) quadrupole mass filter ($p_3 \approx 1 \times 10^{-7}\,\mathrm{mbar}$); (f) ion deposition ($p_5 \approx 1 \times 10^{-9}\,\mathrm{mbar}$).

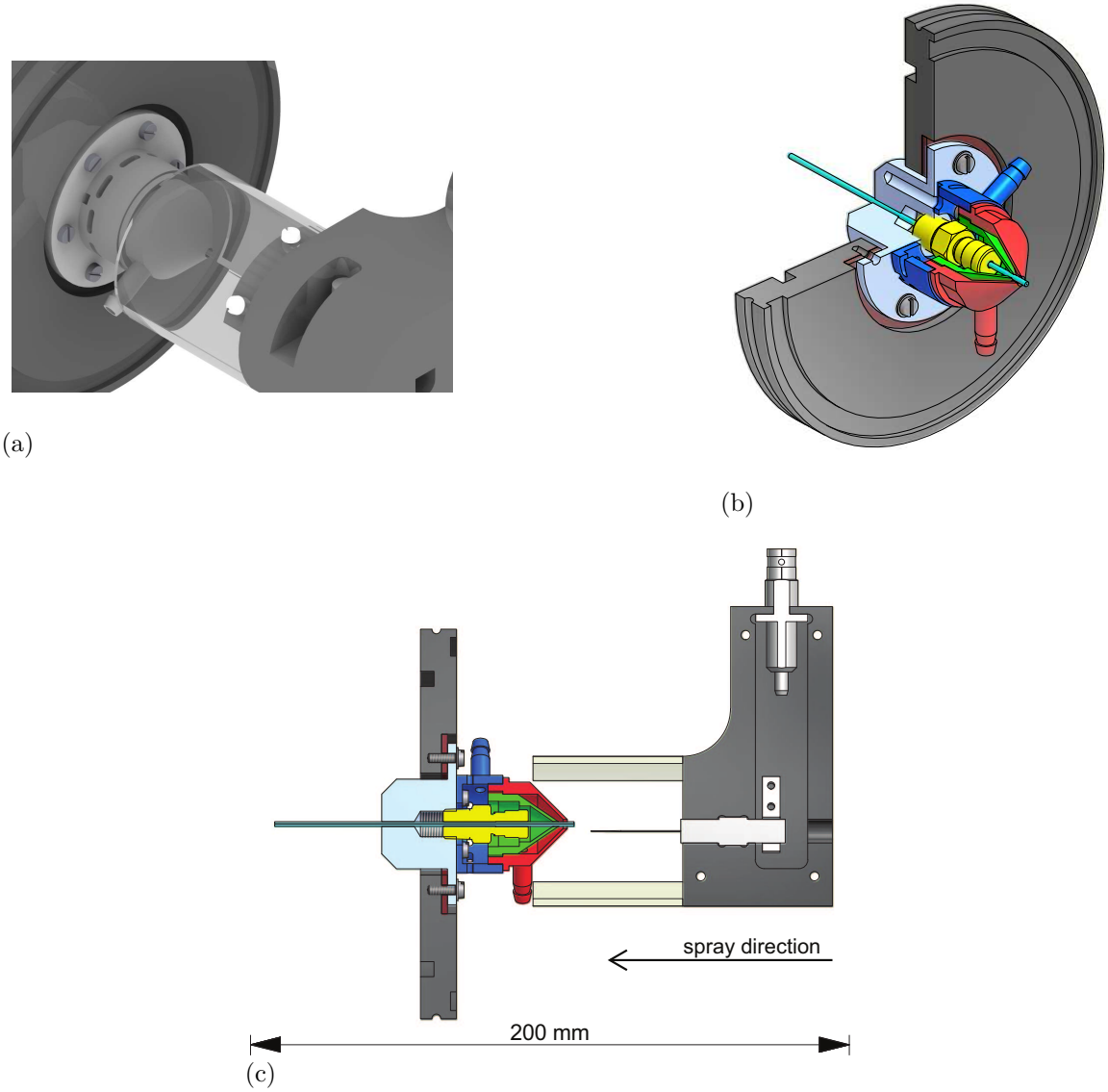

FIGURE 3.2: *Electrospray Ion Source.*
(a) Three–dimensional representaion of the ion source with the vacuum flange including the capillary feedthrough and countergas nozzel at the left rear, the insulating hood in the middle and the high voltage connection housing at the front right. The ionizing high voltage is applied to the spray tip (black needle in (c)) inside the black PVC part by an SHV jack. The desolvation capillary ((b) and (c) turquoise) is fed through the vacuum flange by an Ultra–Torr connection (Swagelock, yellow in (b) and (c)). The red and green nozzles provide the heated counter gas flow, the dark blue connection can be used for additionally tempering the capillary. The complete capillary and nozzle setup is electrically insulated by a rubber gasket (brown).

3.2 Electrospray Ion Source

The ions intended to be deposited are produced by a home–made electrospray ion source (Figure 3.1(a)). The sample solution is forced by a syringe pump (KDS100 syringe pump, KD Scientific Inc.) through a stainless steel needle (Metal TaperTip, Tip ID 100 µm, New Objective Inc., black needle in Figure 3.2(c)), floating at ±2–7 kV relative to the desolvation capillary (turquoise in Figure 3.2), which interfaces the atmospheric pressure spray to the first pumping stage. By changing the polarity of the voltage applied to this needle, positive or negative charged ions can be produced in the so–called positive or negative ion mode.

The position of the spray needle can be changed with respect to the capillary by an XYZ linear stage. A heated counter gas flow of 1–5 l/min at approximately 200 °C supports droplet desolvation. This counter gas flow is applied at the connection coloured red in Figure 3.2 and guided by the nozzles coloured red and green. The connection coloured blue can be used to apply a gas stream for cooling the desolvation capillary below the temperature of the heated counter gas to prevent damage of the rubber sealing inside the Ultra–Torr connection (Swagelok, yellow in Figure 3.2).

The desolvation capillary, the feedthrough and the counter gas nozzles are electrically insulated by a rubber gasket (Figure 3.2, brown). This allows to apply a defined voltage between the desolvation capillary and the first electrode of the ion funnel. The electrospray is protected by a transparent hood, which acts as a protection against contact while providing optical access for judging the spray status. At the same time the spray gets more stable, as undesired motion of the air is avoided.

The ion current entering the vacuum system typically averages out at 4–5 nA.

3.3 Differential Pumping System

The vacuum system of the combined electrospray deposition and LT-STAFM system is displayed in Figure 3.3. It consists of five differentially pumped chambers. A 200 m^3/h roots pump (WKP 250 AM, Pfeiffer Vacuum Inc.) backed up by a 65 m^3/h rotary vane pump (DUO 65 M, Pfeiffer) is used for pumping the first chamber down to 0.7 mbar overcoming the 5 mbar l/s gas load induced by the desolvation capillary (100 mm length, 0.03 " ID, stainless steel). Another 65 m^3/h rotary vane pump is attached to the second chamber which is connected to the first chamber by a 1.5 mm aperture, achieving a pressure of 5×10^{-2} mbar.

To strictly separate the viscous and molecular flow regimes an aperture with a diameter of just 1.0 mm is placed between the second and third chamber, as different approaches are required for focusing ions in the different flow regimes. The third and fourth chambers, containing the electrostatic quadrupole deflector and the quadrupole mass spectrometer, are pumped by 500 l/s turbo molecular pumps (TMU

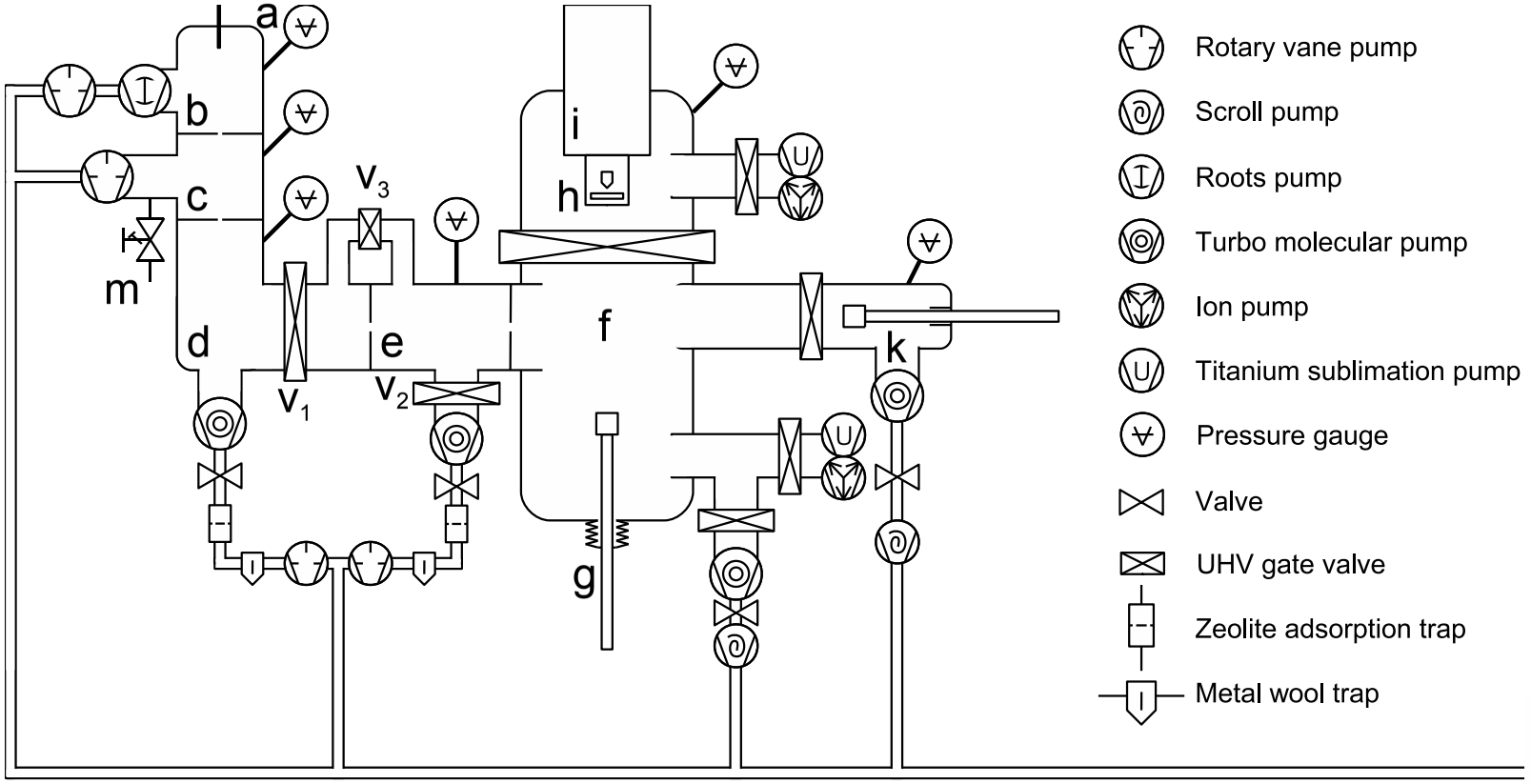

FIGURE 3.3: *Schematics of the Vacuum System of the Combined Electrospray Deposition LT–STAFM Experiment. (a) ambient pressure electrospray ion source; (b) and (c) two vacuum stages of the radio frequency ion funnel at a pressure of* $p_1 \approx 0.8\,\mathrm{mbar}$ *and* $p_2 \approx 3.5 \times 10^{-2}\,\mathrm{mbar}$*; (d) vacuum chamber housing the quadrupole deflector (*$p_3 \approx 1 \times 10^{-5}\,\mathrm{mbar}$*); (e) quadrupole mass filter chamber (*$p_3 \approx 1 \times 10^{-7}\,\mathrm{mbar}$*); (f) preparation chamber of the LT–STAFM system (*$p_5 \approx 1 \times 10^{-9}\,\mathrm{mbar}$*); (g) manipulator used for deposition and transfer of the sample to the STM/AFM, providing the possibility to heat or cool the sample; (h) STM/AFM in its vacuum chamber; (i) liquid helium cryostat; (k) load–lock chamber; (m) needle valve for pressure adjustment in the second ion funnel stage; the usage of the gate–valves (*V_1*) to (*V_3*) is explained in Section 3.3.*

521, Pfeiffer). Between these two chambers there is a 5.08 mm aperture. They can be cut off by a UHV gate–valve (V_1, VAT, DN–100 CF) when no deposition is performed.

The turbo molecular pump of the fourth chamber can be separated by a gate–valve (V_2, VAT, DN–160 CF) as well. During operation the respective pressures in these chambers basically read 1×10^{-5} mbar and 1×10^{-7} mbar. In the preparation chamber, behind the last aperture of 5.08 mm, the pressure increases by only 3×10^{-10} mbar, allowing for deposition times of several hours before severe substrate contamination occurs. This chamber is pumped by a combination of a turbo molecular (500 l/s), an ion (300 l/s) and a titanium sublimation (1000 l/s) pump.

The pressure is measured by Pirani gauges (PPT 100, Pfeiffer) in the first two vacuum stages and by combined Pirani / Bayard-Alpert gauges (HPT 100, Pfeiffer) in the other stages, which are connected to a single control unit (DPG 109). The pressure in the second ion funnel vacuum stage can be adjusted by a gas dosing valve to optimize the ion funnel transmission efficiency.

Rotary vane pumps (DUO 10, Pfeiffer) provide the required fore–vacuum for the turbo molecular pumps, pumping the high and ultra–high vacuum chambers. To avoid any traces of lubricant in the vacuum chamber a combination of a fore–vacuum safety valve, a metal wool trap, and a zeolite trap was mounted.

If the gate valve between the two chambers containing the quadrupole deflector and the quadrupole mass filter was closed, the volume between the seat of the valve and the wall separating these chambers would just be pumped through conductance limiting aperture. To improve the pumping speed an additional bypass was installed, which can be closed by another gate–valve (V_3, VAT, DN–40 CF).

All UHV gate–valves installed in the deposition setup are operated electro–pneumatically. To avoid any unintended operation, a hardware interlock was implemented, allowing opening only under controlled conditions. The gate–valve (V_1) separating the chambers housing the quadrupole deflector and the quadrupole mass filter can only be opened, if both chambers are under vacuum and the bypass gate–valve (V_3) is closed. On the other hand, the bypass gate–valve can only be opened if V_1 is closed. For the turbo pump gate–valve (V_2) being allowed to open, the turbo pump needs to be running and chamber housing the quadrupole mass filter needs to be under vacuum. This arrangement of gate–valve allows to seal the deposition system and turn off all mechanical pumps during the STM measurements.

3.4 Ion Funnel

Within the high and ultra–high vacuum regime, charged particles can be guided precisely by means of electrostatic or magnetic fields. In low and fine vacuum this guiding process is hindered by background gas collisions and induced gas dynamic effects. Therefore it is difficult to realize a high ion transfer, which is important to achieve acceptable deposition times. Another challenge in the first vacuum chamber of an ambient pressure ionization mass spectrometer is the spatial size of the expanding gas jet. An RF–only multipole ion guide usually cannot accomplish a huge acceptance area of ions from the jet and a small focus for effective transmission through the conductance–limiting orifice to the next vacuum chamber. The solution implemented in many commercial mass spectrometers is a skimmer as conductance limit, that samples only a small part of the jet and usually limits the total ion current.

To improve the sensitivity of ESI mass spectrometers ionization mass spectrometry, a so–called *ion funnel* setup was proposed. This device, replacing the common skimmer setup [16], provides collisional focusing in low and fine vacuum [73]. It is a modification of known radio frequency ion guides and ion traps reported in References [44, 74].

An ion funnel consists of a series of ring electrodes with gradually decreasing inner diameter. RF–potentials that are phase shifted by 180° are applied to adjacent electrodes to radially confine the ions and a DC gradient drives them towards the conductance–limiting orifice. A review of the development of the ion funnel until today can be found in Reference [75].

The home–built two stage ion funnel setup designed for the presented deposition source (Figure 3.1(b) and Figure 3.1(c), orange and Figure 3.4) is composed of 29 electrodes in the first and 33 electrodes in the second vacuum stage made of 0.5 mm thick gold coated brass plates. In the first stage the free inner diameter decreases parabolically from 15.25 mm to 1.5 mm. The second stage starts with a drift region of 7.13 mm inner diameter and a length of 55 mm followed by a series of electrodes with gradually decreasing inner diameter as in stage one. The electrodes are spaced from each other using insulating washers by 3.25 mm, 2.25 mm or 1.75 mm thickness depending on the inner diameter to prevent ion trapping in the RF pseudo potential dwells while keeping the overall capacitance low.

The electrodes and washers are mounted on six alumina rods with 5.0 mm diameter and a length of 200 mm circular arranged around the ion funnel axis at a diameter of 60 mm using through holes. Each electrode exhibits three soldering tabs for applying the required RF and DC potentials. To avoid complicated wiring and to make the funnel fit into a 100 mm chamber these soldering tabs were arranged in three different geometries as shown in Figure 3.5.

Carbon resistors of different resistances, as listed in Table 3.1, were soldered to two

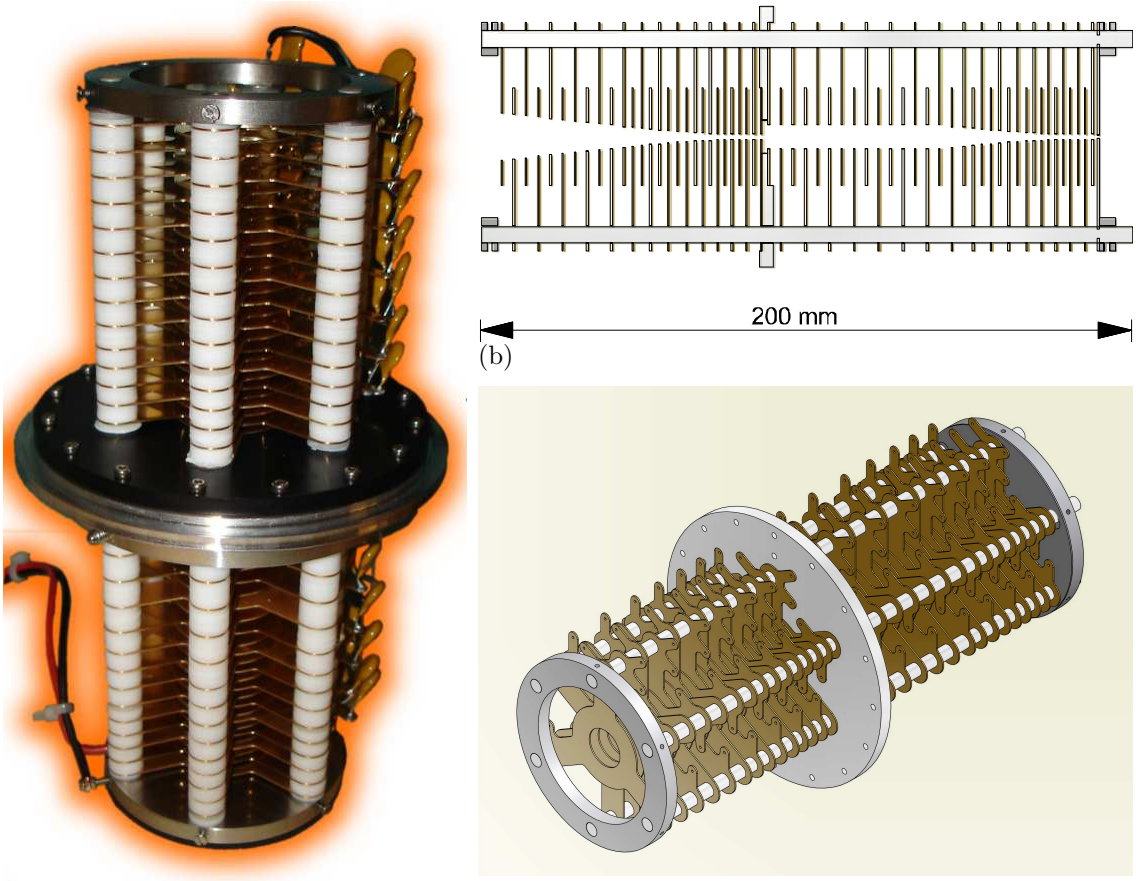

FIGURE 3.4: *Ion Funnel.*
(a) Photograph of the radio frequency ion funnel. A PVC disk (middle, black) separates the first and second stage of the funnel. Insulating washers (white) on ceramic rods separate the electrodes. RF is applied by 1 nF *capacitors (yellow, right), the resistor chain for dividing the DC voltages is hidden. (b) Sectional view of the ion funnel. The inner diameters of the first stage decrease in a parabolic way, the second stage starts with some electrodes of equal diameter. For exact dimensions compare Table 3.1 and Section 3.4. (c) Schematic 3D view of the ion funnel.*

neighbouring electrodes to divide the DC potentials applied to electrode 1, 30 and 62. The DC potential gradients, provided by the chain of carbon resistors, in both funnel stages can be controlled separately. The simulations presented in Section 3.4.1 have shown, that at pressures around 0.4 mbar the field strength should match the depth of the effective potential dwells to prevent ion trapping. Accordingly the resistances in the second vacuum stage are chosen in a way to be roughly proportional to the depth of the effective potential dwells V_{trap}. In the first vacuum stage a constant electrostatic field, providing a constant drag force towards the conduction limiting

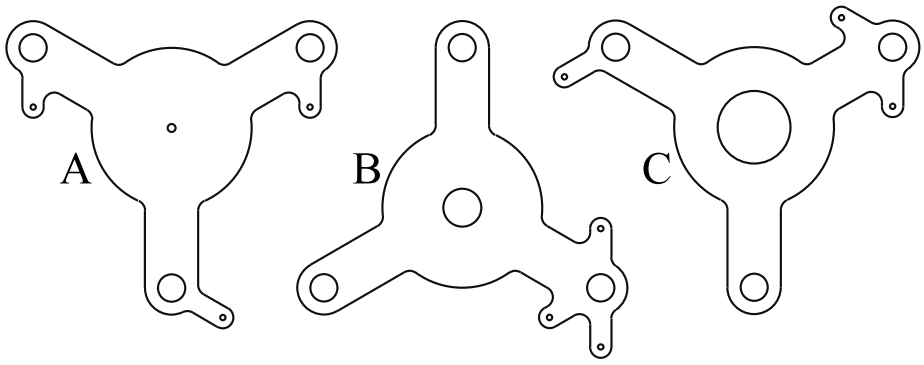

FIGURE 3.5: *Ion Funnel Electrode Layout.*
Examples for the three different arrangements of the soldering tabs on the ion funnel electrodes. Capacitors supplying the RF are applied on the tabs pointing outwards, two resistors, one to each neighbouring electrode, are soldered on the tabs pointing inwards. The inner diameter of the electrodes shown is A: 1.5 mm *(smallest diameter), B:* 7.1 mm *(drift region) and C:* 13.6 mm *(close to the ion funnel opening).*

orifice, is expected to yield a high transmission, since the ion motion gets even more affected by damping and the direction of the gas flow. Low–pass filters on the leads providing these voltages prevent radio frequency crosstalk on the DC power supplies.

Each ion funnel electrode is connected to a radio frequency high voltage power supply by a 1 nF capacitor in such a way that the phase shifts by 180° to its neighbouring electrodes. The RF voltage drop on these capacitors is insignificant, because the driven capacitance of one electrode to its neighbouring electrodes is in the low pA range. The RF is driven by a power supply similar to the one described by I. Čermák [76]. A 48 μH inductor is soldered to the two RF–supply leads and the capacitance of the ion funnel of approximately 310 pF form a resonance circuit at a frequency of 1.3 MHz. The voltage reaches up to 220 V peak–to–peak. A scheme of the voltage connections to the ion funnel is outlined in Figure 3.6. Behind the last ion funnel electrode at a distance of 1 mm an additional stainless steel electrode provides the aperture for differential pumping. This electrode is connected to a separate DC power supply and no RF is applied. All required DC voltages are provided by the optic modules of the Merlin 5221 Controller not only for the ion funnel but also for every other electrostatic ion optical device.

no.	$2 \cdot \rho$ (mm)	d^* (mm)	type	R (MΩ)	no.	$2 \cdot \rho$ (mm)	d^* (mm)	type	R (MΩ)	V_{trap}[1]
					30	7.13	3.25	*A*	2.7	0.26
					31	7.13	3.25	*C*	2.7	0.26
					32	7.13	3.25	*B*	2.7	0.26
					33	7.13	3.25	*B*	2.7	0.26
1	15.25		*B*		34	7.13	3.25	*A*	2.7	0.26
2	14.44	3.25	*A*	10.0	35	7.13	3.25	*C*	2.7	0.26
3	13.63	3.25	*C*	10.0	36	7.13	3.25	*B*	2.7	0.26
4	12.82	3.25	*B*	10.0	37	7.13	3.25	*B*	2.7	0.26
5	12.00	3.25	*B*	10.0	38	7.13	3.25	*A*	2.7	0.26
6	11.19	3.25	*A*	10.0	39	7.13	3.25	*C*	2.7	0.26
7	10.38	3.25	*C*	10.0	40	7.13	3.25	*B*	2.7	0.26
8	9.57	3.25	*B*	10.0	41	7.13	3.25	*B*	3.0	0.26
9	8.75	3.25	*B*	10.0	42	7.13	3.25	*A*	3.0	0.26
10	7.94	3.25	*A*	10.0	43	7.13	3.25	*C*	3.0	0.26
11	7.13	3.25	*C*	10.0	44	7.13	3.25	*B*	3.0	0.26
12	6.32	3.25	*B*	10.0	45	6.32	3.25	*B*	3.0	0.44
13	5.75	2.25	*B*	8.6	46	5.75	2.25	*A*	3.0	0.29
14	5.19	2.25	*A*	8.6	47	5.19	2.25	*C*	3.0	0.50
15	4.67	2.25	*C*	8.6	48	4.67	2.25	*B*	3.0	0.80
16	4.18	2.25	*B*	8.6	49	4.18	2.25	*B*	3.3	1.22
17	3.74	2.25	*B*	8.6	50	3.74	2.25	*A*	3.6	1.78
18	3.33	2.25	*A*	8.6	51	3.33	2.25	*C*	4.3	2.46
19	2.97	2.25	*C*	8.6	52	2.97	2.25	*B*	4.7	3.2
20	2.65	2.25	*B*	8.6	53	2.65	2.25	*B*	5.6	4.1
21	2.36	1.75	*B*	6.8	54	2.36	1.75	*A*	6.2	5.1
22	2.16	1.75	*A*	6.8	55	2.16	1.75	*C*	6.8	6.1
23	1.98	1.75	*C*	6.8	56	1.98	1.75	*B*	7.5	7.0
24	1.84	1.75	*B*	6.8	57	1.84	1.75	*B*	9.1	7.9
25	1.72	1.75	*B*	6.8	58	1.72	1.75	*A*	9.1	8.6
26	1.62	1.75	*A*	6.8	59	1.62	1.75	*C*	10.0	9.2
27	1.55	1.75	*C*	6.8	60	1.55	1.75	*B*	10.0	9.6
28	1.51	1.75	*B*	6.8	61	1.51	1.75	*B*	10.0	9.9
29	1.50	1.75	*B*	6.8	62	1.50	1.75	*A*	10.0	10.0

TABLE 3.1: *List of Ion Funnel Electrodes.*

Numbering starts at the electrode closest to the desolvation capillary. The electrodes of the first stage are listed in the left columns, electrodes of the second stage in the right ones. The electrodes inner diameter $2 \cdot \rho$ and separation distance d^* define the geometry of the effective potential. The three different types of electrodes differ in the arrangement of the soldering tabs as shown in Figure 3.5. The voltage–dividing resistors R and separation distances d specified are located between the listed and the preceding electrode. For a detailed description of the dimensions of the ion funnel see Section 3.4.

[1] normalized depth of the RF effective potential dwells [60], compare Figure 3.8

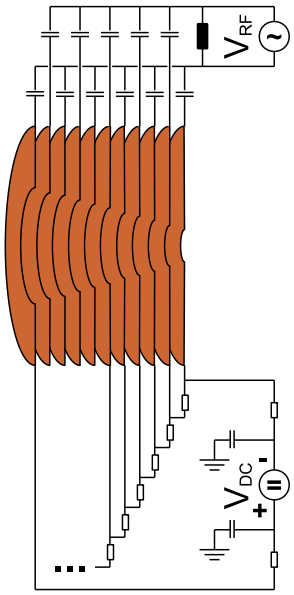

FIGURE 3.6: *Ion Funnel Voltage Connections.*
A DC potential gradients, is provided by the voltage–divider made up of carbon resistors of different resistances as listed in Table 3.1. The ion funnel electrodes are connected to the RF power supply by capacitors, blocking the DC voltage, in such a way to be phase shifted by 180° *to the adjacent electrodes. To prevent the RF–voltage from reaching the DC power supply, this supply is attached via low–pass filters. The ion funnel's capacitance and a parallel inductor form a resonance circuit at a resonance frequency. The RF power supply drives the RF voltage at resonance.*

Theoretical considerations show that ion funnel transmission efficiencies of almost 100 % may be realized [60]. However, experimental values are obtained by comparing incoming and outgoing ion currents. While low mass, solvent–related ions or charged droplets contribute to the incoming current, these particles are not transmitted. Therefore the experimentally determined values are usually lower than the theoretical ones. Nevertheless transmissions of 60 % have been reported for an m/z range of 200 u/e to 2000 u/e [77]. For the funnel presented here, more than 400 pA outgoing current has been detected for an incoming current of 5 nA. This corresponds to a transmission close to ten percent for two ion funnel stages in series and will allow the total transmission of one percent as required in Section 1.3.

3.4.1 The Ion Funnel within the Adiabatic Approximation

In this section the transmission characteristics of the presented ion funnel will be investigated by a numerical method. The effective potential of the ion funnel will be presented and the validity of the adiabatic approximation will be discussed. As an important result, transmission plots of the accessible DC / RF voltage range will be shown for different background gas pressure regimes, including a rough analysis of the corresponding kinetic energy distribution of the ions. Some conclusions for reasonable use of the funnel will be drawn.

In general a complete theoretical investigation of an ion funnel setup would have to take into account the time dependent E–field, composed of RF and DC, damping and random component action of ion–neutral collisions and ion–ion Coulomb interaction. Such a study has been reported for a specific geometry in Reference [60].

The presented numerical computation takes damping and random component ac-

tion of background gas collisions into account. The space charge effect and the electric field time dependence are omitted, because their influence has already been studied [47, 60] and computation time would significantly increase.

Effective Potential

To understand the operation of the ion funnel, generally the effective potential approximation (Equation (2.4)) is used and Equation (2.10) is written as

$$V^*(r,z) = \frac{qE_0^2(r,z)}{4m\omega^2} \tag{3.1}$$

with r, z as radial and axial position.

The first step of these computations is the numerical solution of Poisson's equation, which has been realized using the SIMION 8.0 software [78]. To calculate the effective potential, a voltage of $\pm 100\,\mathrm{V}$ has been applied to every second electrode and Poisson's equation was solved. The derived potential is shown in Figure 3.7(a). The corresponding electrical field was squared and calibrated according to Equation (3.1) using a sample ion of $m = 1500\,\mathrm{u}$ and $q = 1e$.[1]

To justify the potential computed this way, it will be compared with the effective potential resulting from an analytical approximation. Basically the ion funnel can be regarded as a ring electrode trap as described in Reference [43] with a varying inner diameter of the electrodes. The ring electrode geometry leads to an effective potential, that can be analytically approximated as follows:

$$V^*(r,z) = \frac{qV_{rf}^2\pi^2}{8m\omega^2 d^2}\left[I_1^2\left(\pi\frac{r}{d}\right)\cos^2\left(\pi\frac{z}{d}\right) + I_0^2\left(\pi\frac{r}{d}\right)\sin^2\left(\pi\frac{z}{d}\right)\right]/I_0^2\left(\pi\frac{\rho}{d}\right) \tag{3.2}$$

wherein d is the spacing between two electrodes, ρ is the inner electrode radius, I_0 and I_1 are 0^{th} and 1^{st} order modified Bessel functions and V_{rf} is the peak-to-peak amplitude of the applied RF voltage.

A comparison of the effective potential calculated this way to the analytical approximation in Equation (3.2) along the ion funnel axis can be found in Figure 3.8. While the shape of both curves is in very good agreement, the absolute values differ slightly, which is most probably due to the assumption of parabolic electrode cross section in the analytic solution of Reference [43] in contrast to the installed electrodes with rectangular cross sections used for the numerical calculation.

The effective potential of the ion funnel setup as experienced by the sample ion

[1] All results in this section are given for sample ions of $m = 1500\,\mathrm{u}$ and $q = 1e$. This mass is comparable to the one of the cyclodextrins used for measuring the ion funnel transmission in Chapter 4.

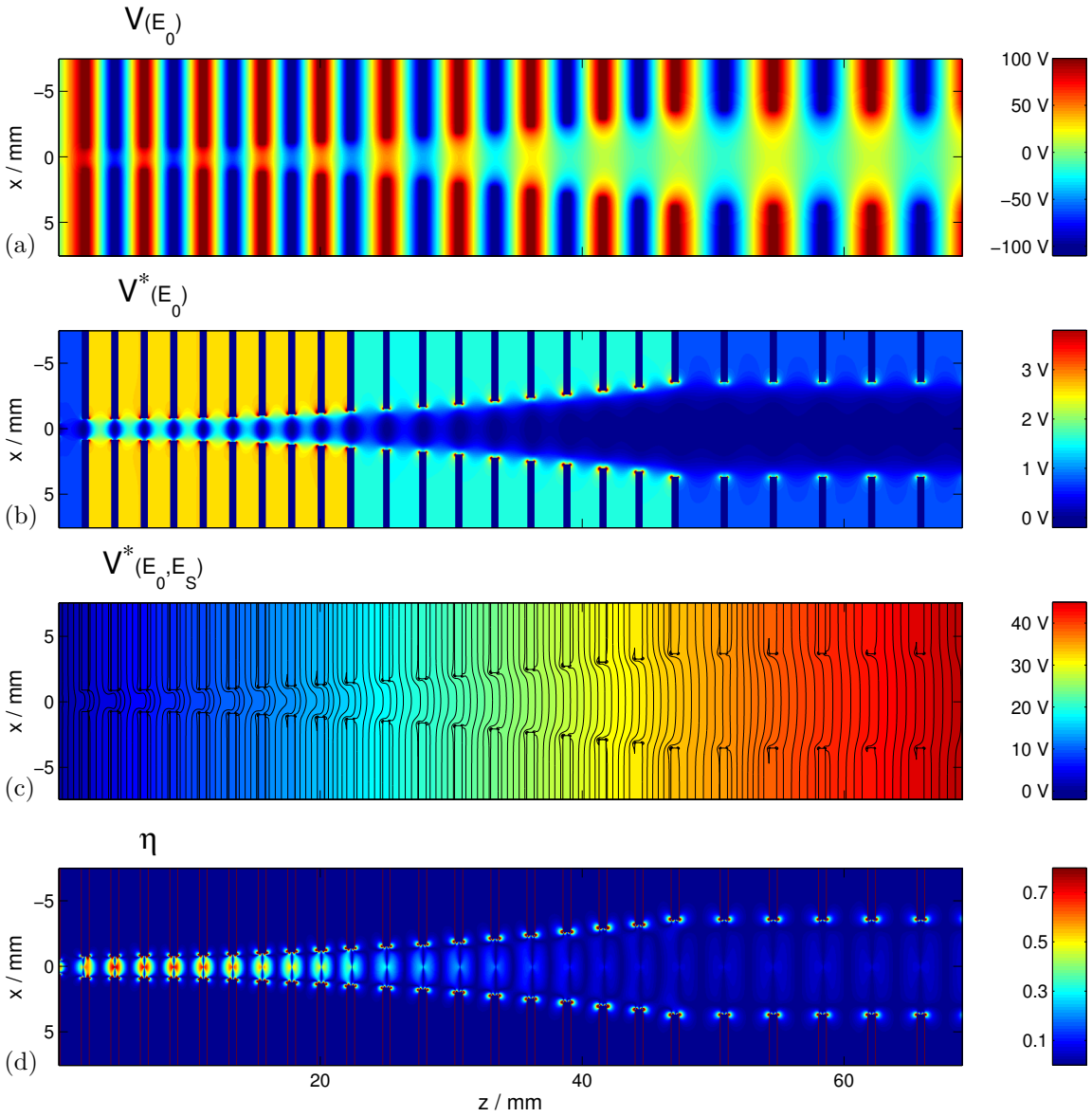

FIGURE 3.7: *Ion Funnel Pseudo Potential and Adiabatic Parameter.*
Cut–out view of the last 24 electrodes of the second ion funnel stage. (a) Snapshot of the maximum electric potential of the RF voltage, (b) pseudopotential of RF voltage only, (c) pseudopotential of superimposed RF and DC voltage, (d) adiabatic parameter η, calculated for the following parameters: $m/z = 1500\,\mathrm{u/e}, V_{RF,pp} = 200\,\mathrm{V}, f = 1.3\,\mathrm{MHz}, V_{DC} = 70\,\mathrm{V}$. For these settings no closed equipotential lines can be found in the total pseudopotential (c), the applied DC voltage is just high enough to eliminate the potential wells and prevent ion trapping. The plot of the adiabatic parameter shows that close to the ion funnel end ($z = 0\,\mathrm{mm}$) the adiabatic approximation is hardly valid.

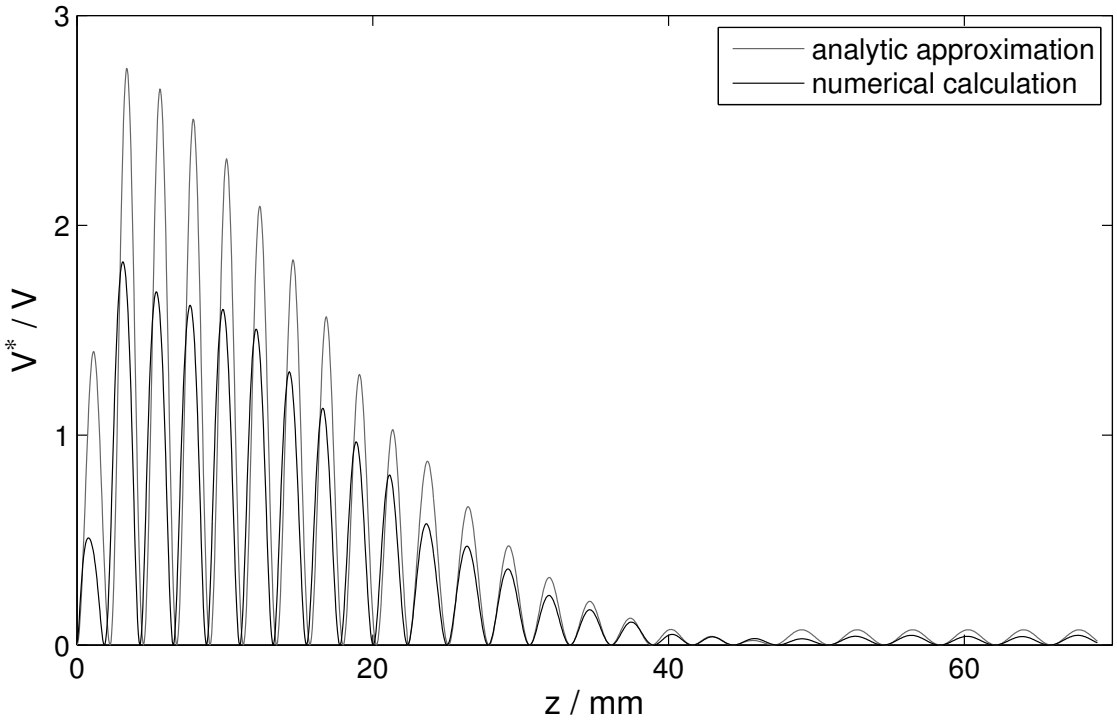

FIGURE 3.8: *RF Pseudopotential along the Ion Funnel Axis.*
The potential was calculated for the electric fields computed by SIMION using Equation (3.1) *(black line) and the analytical approximation from Equation* (3.2) *(grey line). Curve shapes are in fair agreement, the absolute value differs for small electrodes inner diameters, most probably due to the different electrode cross sections used.*

is presented in Figure 3.7(b) for a peak to peak voltage of $V_{RF} = 200\,\mathrm{V}$ and an RF frequency of $f = 1.3\,\mathrm{MHz}$. Close to the ion funnel end the effective potential forms dwells of almost 2 eV depth. The radial component of the effective potentials gradient always points towards the ion funnel axis. To drive the ions through the funnel, a DC voltage of $V_{DC} = 70\,\mathrm{V}$ is applied on the first and last of the 31 electrodes and divided according to the resistors listed in Table 3.1 No. 1 to 29. The total effective potential of the superposition of the RF and DC fields is shown in Figure 3.7(c). For these settings no closed equipotential lines can be found, thus ions cannot be trapped in the potential dwells. The radial and axial components of the effective potentials gradient always point towards the ion funnel axis or end respectively. Using these settings with elevated background gas pressure will result in the ions being guided towards the conductance limit without a significant gain of kinetic energy as will be shown in the following.

The plot of the adiabatic parameter η in Figure 3.7(d) calculated according to Equation (2.14) shows that the adiabatic approximation is hardly valid and ions

–especially of lower mass to charge ratios– may gain kinetic energy. The maximum value of η in this case is 0.75.

Transmission Characteristics

The transmission probability of the ion funnel depends on the applied voltages, given vacuum pressure and properties of the ions. To understand the transmission probability in detail, the trajectories of a set of one hundred ions were calculated (within the SIMION package) for a range of DC– and RF–voltages and for five different background gas pressures. For deposition experiments the amount of ions transmitted within a certain interval of kinetic energy is more important than the integrated transmission, because individual ions with a high impact energy will be destroyed at impact. Therefore not only the transmission probability but also the average kinetic energy and the kinetic energy distribution width of the transmitted ions is evaluated. In the simulation the ions started 66 mm in front of the last ion funnel electrode of the second funnel stage on a disk of 0.5 mm radius around the ion funnel axis. Their initial kinetic energy was arbitrarily chosen to be 0.1 eV with an angular distribution of 45° around the axis.

The results of the simulation are displayed in Figure 3.9. Each column images the results for a different background gas pressure (0, 1, 10, 40 and 100 Pa). The first row displays the total transmission probability, the second and third row the average kinetic energy gain and distribution width respectivly. To get an idea of the amount of particles that can be gently deposited, the transmission probability within an energy interval of 2 eV around the average kinetic energy is shown in the lowest row of Figure 3.9.

In the left column of Figure 3.9 the transmission is investigated in the absence of any background gas. Under these conditions the transmission plot (Figure 3.9 top left) becomes complicated and the exact starting conditions and voltage settings have a strong influence. Several regions of high transmission can be identified. Due to the effective potential the ions perform macroscopic oscillations around the ion funnel axis while being acellerated towards the ion funnel end. The frequency of the mascroscopic oscillation depends on the strength of the effective potential and the time needed for passing the funnel depends on the applied DC–voltage. If the RF– and DC–voltage match in a way, that each ion performs a multiple of a half oscillation during its passage, the ions will be quite close to the axis of the funnel at the last electrodes and transmission will be high. In the uppermost region of high transmission in the corresponding transmission plot ions can perform two half oscillations, in the high transmission region below three half oscillation, etc. During the passage the ions potential energy in the electrostatic potential is completely converted to kinetic energy because of the abscence of any background gas scattering events. The contrast in the kinetic energy distribution of the ions plot is just a statistical artefact. Since

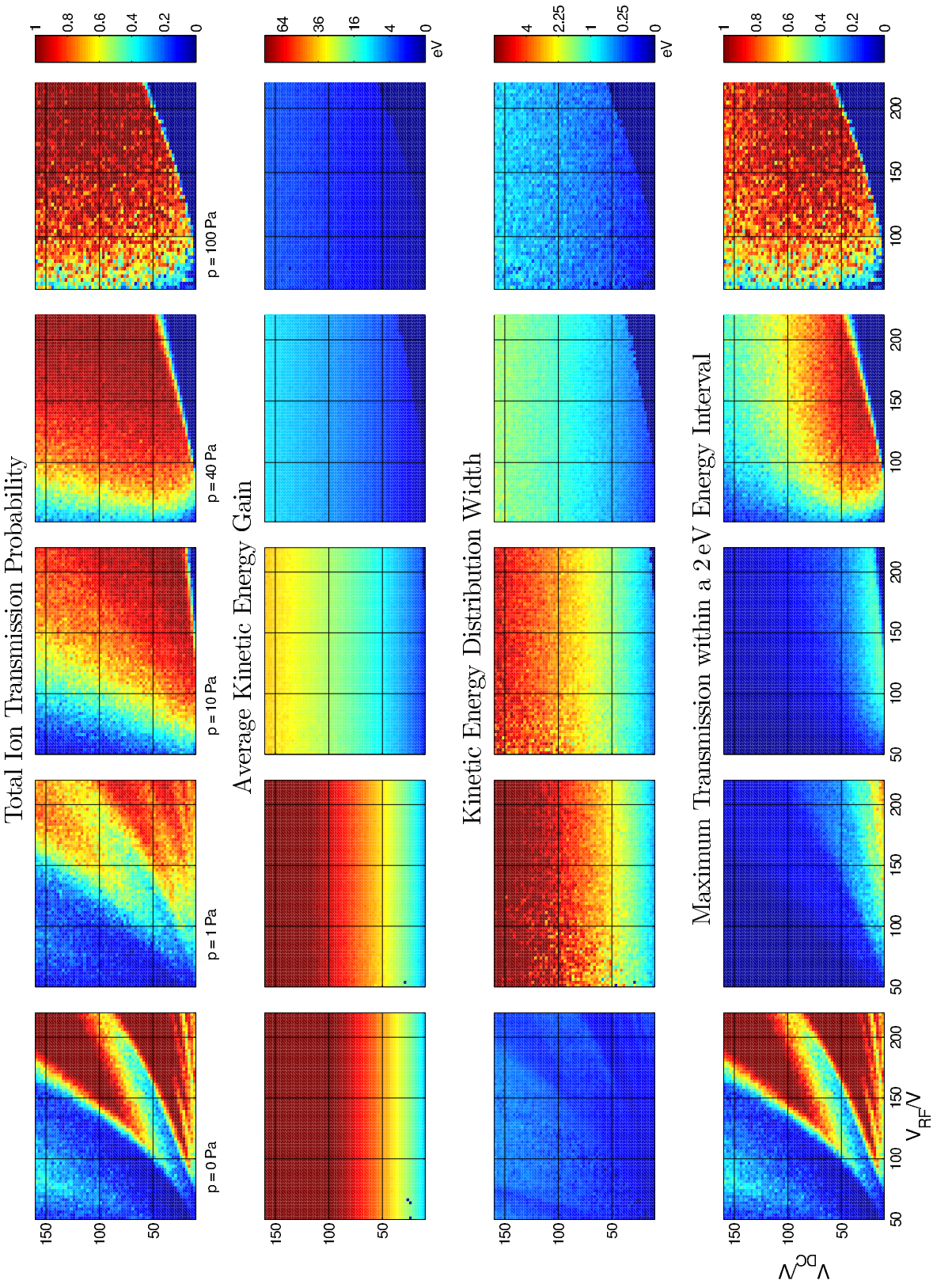

FIGURE 3.9: *Ion Funnel Transmission Probability.*
Pressure dependent transmission probability, kinetic energy gain and broadening and weighted transmission for the experimental accessible DC– and RF–voltage range. This figure is described in full detail in section ***Transmission Characteristics*** *on the Page 43.*

the kinetic energy is not spread, all ions are in the 2 eV transmission window and the maximum transmission within the 2 eV energy interval is identical to the total ion transmission.

In the following three columns the background gas pressure is raised to 1, 10, and 40 Pa respectively using a hard sphere collision model with an estimated cross section of $\sigma = 1.2 \cdot 10^{-17}$ m^2 and nitrogen ($m = 28$ u) as background gas. At 1 Pa the structure in the transmission plot, as seen at 0 Pa, is already smeared but still visible. Approximately half of the ions initial potential energy is lost in collision events and the energetic distribution of the ions is quite broad ($\approx 5\%$ of V_{DC}). As the pressure is raised to 10 Pa (third column) the transmission probability plot gets more uniform and energy gain and distribution width decrease due to the increasing number of scattering events. For both pressures (1 Pa and 10 Pa) the energy distribution width (standard deviation) is only below 2 eV for DC–voltages below ≈ 40 V and ≈ 60 V respectivly. Due to the broad energy distribution the weighted transmission in a 2 eV window is very low except for a small range at very low DC–voltages. As the pressure is increased a region of no transmission arises in the lower right part of the transmision diagram. This region of no transmission is caused by trapping of ions in the dwells of the effective potential.

At a background gas pressure of 40 Pa (fourth column) the transmission probability is high over a wide range of voltage settings. At the same time kinetic energy gain and distribution width decrease significantly because of the increased collision rate. As a result a transmission probability of almost one can be found in the weighted transmission plot around $V_{RF} \approx 170$ V and $V_{DC} \approx 40$ V.

As the pressure is further increased energy gain and distribution width decrease further and the weighted transmission should rise in principle. However the number of collision events during one oscillation in the RF–field is now high enough (~ 100 collisions per oscillation) to significantly decrease the oscillation amplitude, resulting in a weaker effective potential at the same applied voltage. In the described example the RF–rescaling factor γ is approximately 0.85 at 100 Pa (compare Equation (2.16) and [47]) and the maximum RF–voltage is barely enough for optimal transmission. At 200 Pa the scaling factor would be down to 0.6 and focusing would get too weak.[2]

The conclusion that can be drawn is that for high transmission in a fixed energy interval the RF and DC voltages as well as the background gas pressure have to be adjusted correctly. Low pressures of $p \leq 10$ Pa (0.1 mbar) are not favourable because the voltages are hard to adjust, the kinetic energy spread is high and in addition desolvation might be incomplete. Pressures higher than 100 Pa (1 mbar) are not favourable because the pressure in the subsequent chambers would increase, which will additionally broaden the energy distribution due to collisions in the high vacuum chambers, in addition the gasload on the sample would increase. Furthermore the

[2] The RF–rescaling factors for the lower background gas pressures are $\gamma(p = 0\text{ Pa}) = 1$, $\gamma(p = 1\text{ Pa}) = 1$, $\gamma(p = 10\text{ Pa}) = 1$ and $\gamma(p = 40\text{ Pa}) = 0.97$.

effective potential scales down at higher pressures and the required voltage cannot be achieved.

Following the ion funnel transmission characteristics, the values $p \approx 40\,\mathrm{Pa}$, $V_{RF} \approx 170\,\mathrm{V}$ and $V_{DC} \approx 40\,\mathrm{V}$ appear to be appropriate but have to be adjusted for every new substance because the effective potential strength and the collisional damping depend on the ion mass, charge and scattering cross section.

Low m/z Cutoff

To estimate the lowest mass to charge ratio that can be transmitted by the ion funnel the amplitude of the ions RF oscillation will be calculated from Equation (2.4) at the local maxima of the effective potential, because the effective potential energy is stored in the oscillatory motion (Equation (2.12)). If the oscillation amplitude is larger than the funnels geometric dimension, the ion cannot be transmitted. At the potential maxima close to the funnel end the RF–field amplitude E_0 is approximately $100\,\mathrm{V/mm}$. The request of the amplitude $\mathbf{A}$ being smaller than half the typical dimension $s \approx 1\,\mathrm{mm}$

$$\frac{qE_0}{m\omega^2} \ll \frac{s}{2}$$

is resulting in a lower mass limit of

$$\frac{m}{q} \gg \frac{2E_0}{s\omega^2}$$

$$\frac{m}{q} \gg 280\,\mathrm{u/e}.$$

This is less than the mass of single nucleotides, which are the building blocks of DNA and RNA. Another effect compromising the transmission of light ions is the increase of the adiabaticity parameter η proportional to $(m/q)^{-1}$. For ions of $m/q = 1000\,\mathrm{u/e}$ η already adds up to one and the ions will gain additional energy.

3.5 Quadrupole Deflector

A practical method to extract ions from a beam mixed of ions and neutral particles is the use of a two–dimensional quadrupole deflector. The electrostatic quadrupole deflector (Figure 3.1(d) and Figure 3.10) acts as an energy filter and prevents neutral contaminations originating from the ion source from reaching the high vacuum chambers. It is often used to sample ions from electrospray or other ambient pressure ion sources.

By changing the applied voltages the deflector can be used to analyse the kinetic energy of the ions. The deflector is redirecting the ion beam from the ion funnel axis to the mass spectrometer axis by a right angle. Because most of the gas load and

condensables move in a straight line once they enter the deflector chamber, they are prevented from directly reaching the next pumping stage. In this way the efficient pumping speed is improved and sample contaminations are minimized. For well collimated beams with a narrow energy distribution, the transmission efficiency can approach as much as 100 % but is usually found to be above 50 % in our experiments. It can be assumed that the main losses are due to the energy dispersion and angular acceptance of the quadrupole deflector.

Identical voltages are applied to opposing rods. The potential difference between the two rod pairs controls the mean kinetic energy of particles allowed to pass through the deflector as well as their energy spread [79].

Half the potential difference between the two rod pairs, ΔV_{QD}, is a quite close approximation of the mean kinetic energy per charge of those particles which pass through the deflector [79, 80]. The energy bandpass of the transmitted ion beam is determined by ΔV_{QD} as well, and in addition by the size of the entrance and exit apertures. To estimate the mean impact energy per charge at the substrate, we use ΔV_{QD} plus the potential difference between the substrate and the average potential of the rods. The quadrupole deflector can be operated by the use of just two voltage sources, one for each pair of rods. The voltage required for the entrance and exit lens is provided by a resistive voltage divider.

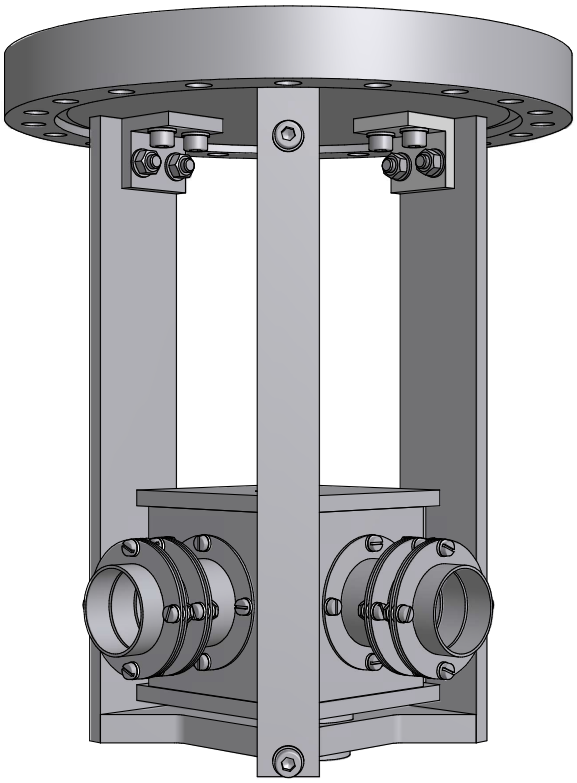

FIGURE 3.10: *Quadrupole Deflector. The assembly consisting of the cube, containing the deflector itself, and two ion optical lens assemblies. The mounting allows for three translational and one rotational (within the deflection plane) degree of freedom. The alignment has to be performed by an optical method. The four quadrupole rods can be seen in the section view in Figure 3.1(d).*

Zeman [81] calculated the ion trajectories in an ideal 2D quadrupole field up to the second order in input position, angle, and energy. The effect of the fringe field of the entrance and exit lens on the deflection angle was found to be significant [79]. Therefore the voltages for 90° deflection were calculated with the SIMION software for the special geometry of the installed deflector (Quadrupole Deflector / Energy Filter, EX-

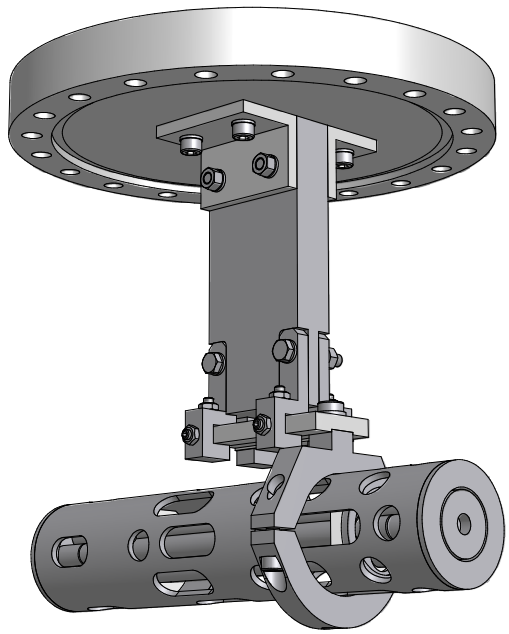

FIGURE 3.11: *Quadrupole Mass Filter. Sketch of the quadrupole mass filter and its mounting mechanism. The mounting allows for all degrees of freedom. The quadrupole is aligned by an optical method as well as a mechanical centring with respect to the flanges.*

TREL). As a result the applied voltage ΔV_{QD} has to be not 2 but 1.85 times the kinetic energy of the ions.

Furthermore the use of a quadrupole provides the option to attach additional ion sources to the setup in future. In principle ion beams from two other ion sources (another one at a right angle to the quadrupole mass filter one aligned with it) could be coupled to the quadrupole mass filter in this way.

As required in Section 1.2 the use of the quadrupole deflector allows to seperate neutral particles out and determine the kinetic energy of the ions.

3.6 Quadrupole Mass Filter

Quadrupole mass spectrometers are well suited for applications where specific ions should be further investigated because of their ability to be set to a specific mass to charge ratio constant. This is in particular the case for deposition experiments.

In a quadrupole mass filter the ions pass through the centre of four parallel rod shaped electrodes, which are aligned in a square configuration. The combination of a DC– and RF–field inside the quadrupole leads to an m/z selection, allowing only particles of a defined mass to charge ratio to pass.

The quadrupole used here (9.5 mm diameter quadrupole mass filter assembly, EXTREL) has a pre and post filter assembly for better transmission (Figure 3.1(e) and Figure 3.11). This mass spectrometer can be operated at different RF to DC ratios to

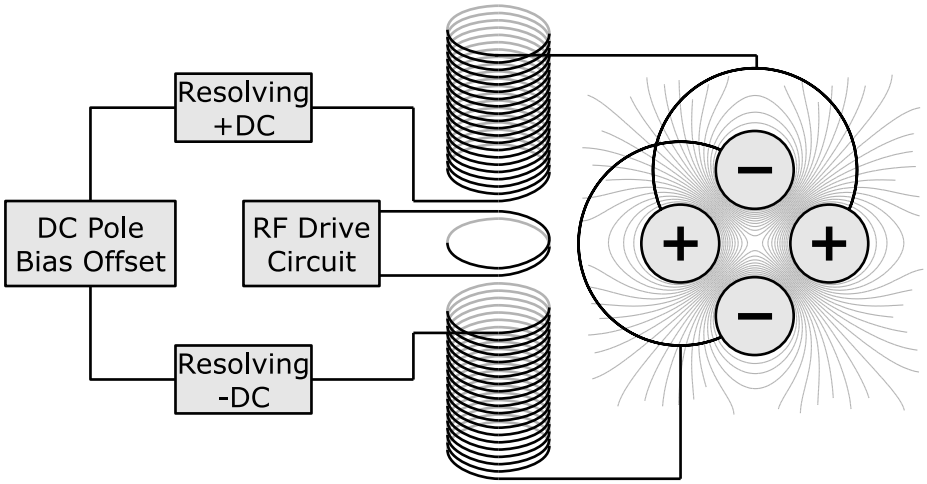

FIGURE 3.12: *Schematics of the Voltage Supplies of the Quadrupole Mass Filter. The DC pole bias offset determines the potential on the quadrupole axis, the two resolving DC voltages are superimposed one on each pair of rods as well as two RF voltages with opposing polarity.*

change mass resolution as well as in the RF only mode with a broad mass transmission range. It is powered by a 1.2 MHz oscillator allowing a maximum of $m/z = 2000$ u/e in mass resolving mode. The lower mass limit of this oscillator is 2 u, maximum mass resolution is 1500 u, and the relative transmission is 25 % [82]. This oscillator can be replaced by a 880 kHz oscillator with a mass range of 10 u to 4000 u, mass resolution of 1200, and 20 % relative transmission. The electronics can source a DC–voltage of ±200 V and an RF–voltage of 7.2 kV. The electrical connections of the quadrupole mass filter are sketched in Figure 3.12.

In general quadrupole mass filters are known to discriminate against high masses, because higher masses require higher mass resolution. The installed quadrupole provides some options to increase the high mass transmission efficiency. The pre and post filter, short extensions of the quadrupole rods with just RF– but no resolving DC–voltage applied, improve the transmission by reducing the effect of fringe fields. Biasing the entrance and exit lens of the quadrupole has the same effect. The operation of the device in the so–called RF–only mode as described in the section **RF–Only Mode** on Page 21 can also provide higher transmission for high masses. Another method is to increase the kinetic energy inside the quadrupole as the mass increases, keeping the time between the rods roughly constant.

The theoretical background of the quadrupole mass filter, including different modes of operation, is explained in detail in Section 2.3.

3.7 Ion Optical Lenses

In all high vacuum stages guiding and focusing of the ion beam is done by cylindrical electrostatic ion optical lenses arranged in pairs (purple in Figure 3.1, compare Figure 3.13). One lens of a pair acts as a collimator and the other one is used to focus the collimated beam to the entrance aperture of the next ion optical device or on the sample.

Each lens stack consists of three cylindrical electrodes with a free inner diameter of 28 mm separated by 1 mm ceramic washers. The two inner electrodes of a lens pair are grounded to provide a field free region for ion transfer and have a length of 10 mm. The outermost electrodes share the potential of the ion optical device they are attached to (V_3 in Figure 3.13) and are 20 mm long to simplify focusing. The lens element directly following the ion funnel is slightly longer and composed of two parts, one of them fixed in the deflector chamber, the other directly attached to the ion funnel, providing the conductance limiting aperture. The focusing potential (V_2 in Figure 3.13) is applied to the middle electrode of a stack having a length of 10 mm as well. Attracting focusing potentials were found to provide higher ion transmission in this setup.

The voltage needed for best focusing / collimation of the ion beam has been determined by simulation in SIMION. Within this simulation a parallel ion beam has been guided to a lens and the voltage V_2 needed for the correct focus length was determined for different values of the kinetic energy per charge of the parallel beam

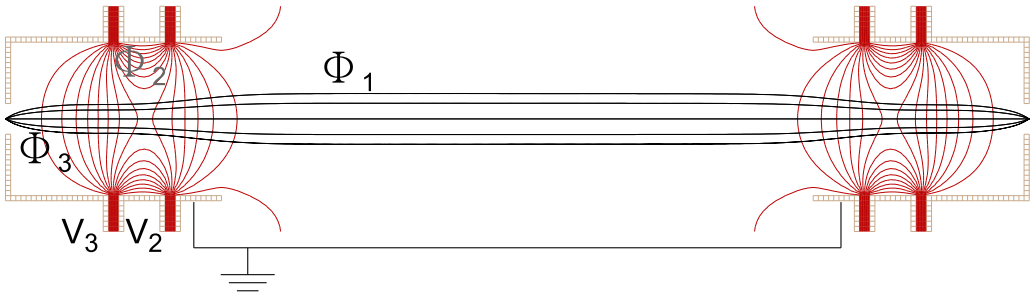

FIGURE 3.13: *Ion Beam Guiding by a Pair of Ion Optical Lenses.*
Ions are guided by pairs of ion optical lenses, one acting as a collimator the other one is focusing the ion beam again. Five ion trajectories are drawn in black and some equipotential lines in red. The kinetic energy of ions on ground potential Φ_1 and the applied voltages V_2 and V_3 determine the kinetic energy Φ_3 of ions passing the aperture of the outermost lens elements and the virtual kinetic energy Φ_2 on the attractive focusing potential V_2.

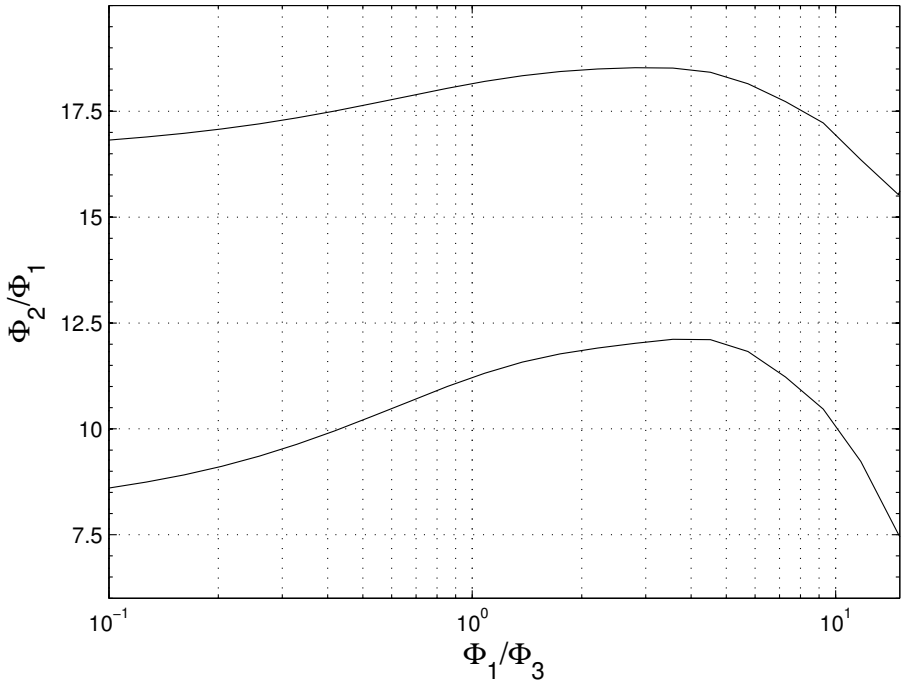

FIGURE 3.14: *Ion Lens Focusing Voltage.*
Diagram for determining the required focusing voltage as described in the text. The upper curve represents all lenses having a focus length of 20 mm. *The one directly following the ion funnel, which has a focus length of* 28 mm, *is represented by the lower curve.*

Φ_1/q and the one of the focused beam Φ_3/q. The latter can be calculated to be

$$\frac{\Phi_3}{q} = \frac{\Phi_1}{q} - V_3.$$

The virtual kinetic energy per charge Φ_2/q on the focusing potential as a multiple of Φ_1/q can be determined from the graph in Figure 3.14 and is used for calculating the focusing voltage

$$V_2 = \frac{\Phi_2 - \Phi_1}{q}.$$

Actual focusing voltages are usually found to be slightly lower because additional fringe fields in between a pair of lenses provide additional focusing.

3.8 Voltage Connections

The DC–voltage used for guiding the ion beam in all the different devices described so far are provided by the so–called optic supplies of the mass spectrometer controller (Merlin Automation 5221 Series Scan and Resolution Controller, EXTREL). In this section the calculation of the voltages from physical quantities will be described. To be able to automatically adjust the voltages applied to all devices–except for the ion funnel–for best transmission, the kinetic energy of ions passing the device has to be known. We can assume that this energy is just influenced by the potential energy in the electrostatic field, once the ions passed the conductance limiting orifice between the second ion funnel chamber and the deflector chamber. The kinetic energy E_{kin} at a location r can be calculated from the initial kinetic energy of the ion E_{esc} (*escape energy*), at the moment it is passing the conductance limiting orifice, the voltage at this orifice V_{IFend} and the electrostatic potential at its location $\Phi(r)$ by

$$E_{kin}(r) = E_{esc} + V_{IFend} - \Phi(r).$$

An other important value is the kinetic energy at locations where the electrostatic potential equals the potential of the–grounded–vacuum chambers. This value is called $E_{kin,0}$. The escape energy E_{esc} has to be estimated from the ion funnel setting using, for example, Figure 3.9.

The Merlin Automation Data System Software (EXTREL) has been expanded by a script, to compute the voltages that have to be applied with respect to ground. These voltage calculations are based on the following assumptions and voltage settings.

The voltages for the ion optical lenses are calculated according to the description in Section 3.7 and Figure 3.14. Both lenses at the deflector are equal in terms of geometry and potential on the focused beam side, therefore they share one voltage output.

The mean value of the two voltages attached to the quadrupole deflector accelerates or decelerates the ions to the so–called *pass energy* E_{pass}, which can be set in the software and grants direct control on the energy band path as described in Section 3.5.

The *ion funnel extraction voltage* is applied between the DC–only gas conductance limiting electrode and the last RF bearing electrode of the ion funnel. The voltages *ion funnel* DC_1 and DC_2 provide the DC gradient in the two ion funnel stages. The DC potential difference between the desolvation capillary and the first electrode of the ion funnel is called *capillary voltage* V_{cap}.

The kinetic energy at the quadrupole mass filters entrance and exit lenses can be set individually. The pre and post filter share one setting.

The ion polarity is taken into account for all voltages. Just the bias voltage of the quadrupole mass filter is not adjusted automatically and not set to the correct polarity if the polarity of the ions is changed. This is due to technical reasons.

3.9 Current Measurement

The measurement of the ion current is performed by a picoammeter (Keithey 6487/E). It can measure currents down to 20 fA at a rise time of 2 ms. A switching unit provides the possibility to measure the ion current at four different locations. These are the first electrode of the ion optical lens directly behind the ion funnel, the last element of the lens in front of the quadrupole mass filter, the first element of the lens behind the mass filter and the sample. This way it is possible to characterize and optimize the produced ion beam step by step. The measurement directly at the sample surface during the deposition allows for estimating the achieved coverage.

The measurement on a single element of the lenses can be very efficient, if the successive electrode is held at a repulsive potential or the beam is defocused, depending on the exact geometry.

The ammeter features an internal voltage source, which can be utilized for floating current measurements. This is, for example, useful for lowering the impact energy of the ions on the surface by applying a repulsive potential.

3.10 Attachment to the LT-STAFM System

The electrospray deposition apparatus is directly attached to a modified cryogenic scanning tunnelling and atomic force microscope system (SPS-CreaTec GmbH, Berlin, Germany) as shown in Figure 3.15. The deposition takes places in an ultra–high vacuum chamber belonging to this system at a pressure of $p_5 \approx 1 \times 10^{-9}$ mbar (Figure 3.1(f)). This chamber is pumped by a combination of a turbo molecular (500 l/s), an ion (300 l/s) and a titanium sublimation (1000 l/s) pump. During deposition the surface is mounted on a differentially pumped manipulator which can be used for heating or cooling the surface and is used for putting the sample to the LT–STAFM. This vacuum chamber provides facilities for preparing the single crystal surfaces by ion bombardment and annealing. It is equipped with a load lock chamber.

The direct connection of the electrospray source to this chamber guarantees the best deposition conditions. The sample can stay under UHV for the complete experiment and in addition can be heated or cooled at any time. The possibility of positioning the surface just some millimetres away from the last focusing lens results in a lower loss rate and the possibility to use the voltage approximation from Section 3.7.

To avoid vibrations of the experimental setup during STM or AFM measurements the aluminium frame of the electrospray source and the stainless steel frame of the LT-STAFM system are rigidly coupled by heavy stainless steel angle brackets and bolts. The complete instrument can be lifted by a pneumatic damping system.

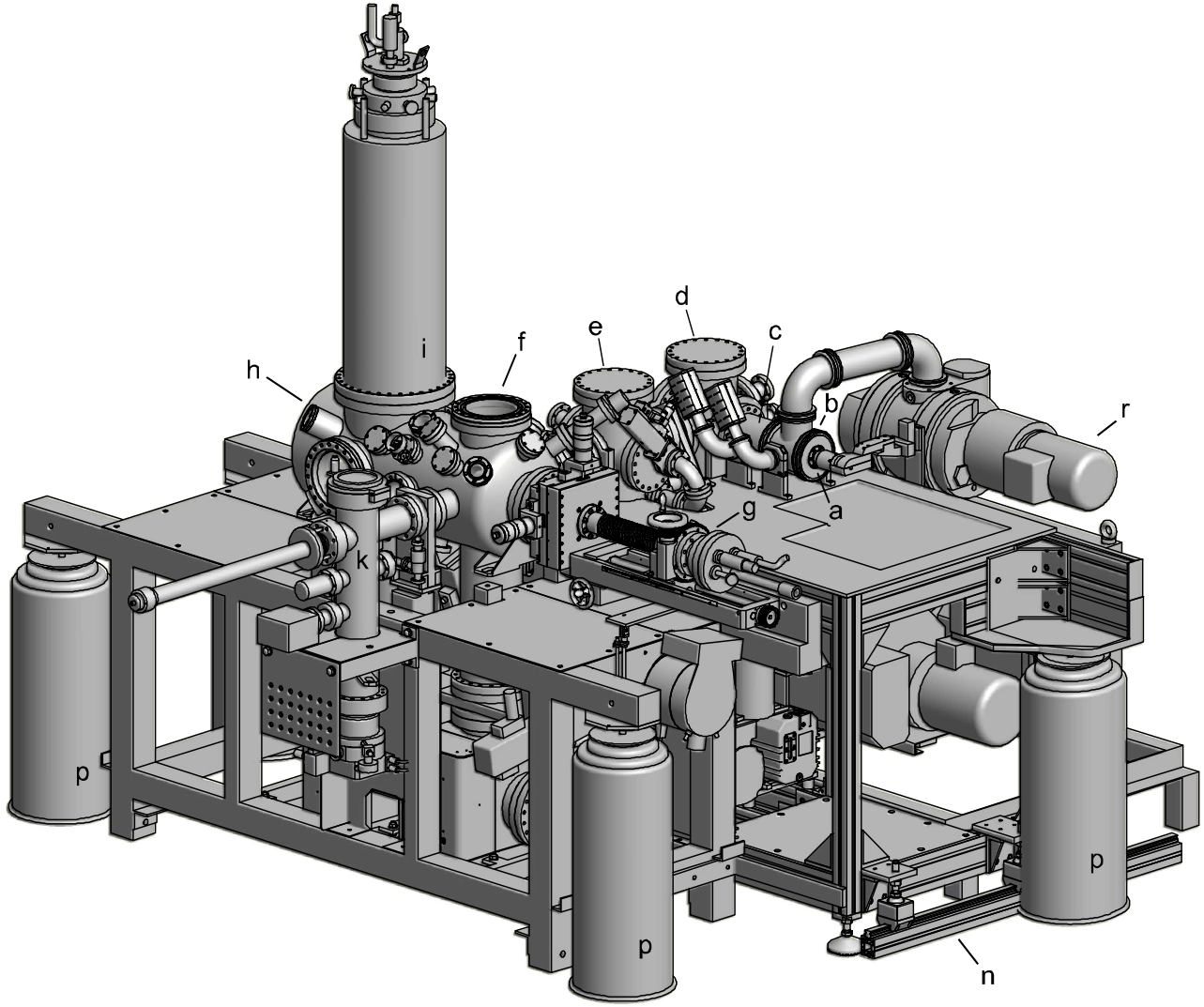

FIGURE 3.15: *Assembly of LT–STAFM and ESI–source.*
(a) Ambient pressure electrospray ion source; (b) and (c) two vacuum stages of the radio frequency ion funnel; (d) vacuum chamber housing the quadrupole deflector; (e) vacuum chamber housing the quadrupole mass filter; (f) preparation chamber; (g) manipulator used for deposition and transfer of the sample to the STM/AFM, providing the possibility to heat or cool the sample; (h) STM/AFM vacuum chamber; (i) liquid helium cryostat; (k) load–lock chamber; (n) rail–system for assembling / dissembling the deposition source to the LT–STAFM system; (p) pressured air damping system; (r) roots pump.

4 Experimental Results

In this chapter experimental data obtained by scanning tunnelling microscopy (STM) and scanning tunnelling spectroscopy (STS) proving the proper operation of the electrospray deposition instrument will be provided. Beforehand the usage of the deposition apparatus as a mass filter and the validity of the results of the simulated ion funnel transmission in Chapter 2 will be shown.

The presented STM and STS results will demonstrate the ability to deposit substances of a wide mass range, the capability to conserve fragile substances as, for example, occurring in biological systems. They prove that samples prepared by electrospray deposition are of similar quality as samples prepared by other techniques, such as thermal sublimation. It can also be shown that deposition rates are sufficient to assure acceptable deposition times.

The first deposition experiment was performed using *manganese tetraphenylporphine sulfonate* (MnTPPS). Its mass of about 1000 u can be observed in the mass resolving mode of the quadrupole mass filter so that deposition can be performed with the mass filter in operation. Porphyrins are a class of substances repeatedly investigated in the STM community and they are suitable for both thermal and electrospray deposition. Therefore MnTPPS is best suited to show that the sample quality for molecules deposited by electrospray deposition can compete those of thermally evaporated ones.

To prove the capability of depositing high mass biomolecules, *bovine serum albumin* (BSA) was chosen with a mass of more than 66000 u. Real space sequencing of DNA is one of the challenges for scanning probe techniques, which could not be met by the traditional sample preparation techniques. The introduction of the pulse injection method [3] was a major advance, and we also hope to contribute to this field by the use of the electrospray deposition technique.

The free ligands of metal–organic grid complexes were investigated in preparation for experiments of metal–organic complexes. Two important results were obtained from these molecules. First, we were able to deposit molecules with a mass to charge ratio of less than 500 u/e, what was not anticipated because of the transmission characteristics of the ion funnel. In addition, a sample with a coverage of approximately 50 % was prepared, proving that the described instrument provides the required ion current.

Ruthenium based dyes for dye–sensitized solar cells are of current interest, but they are thermally too unstable to be deposited by thermal deposition techniques. The application of the electrospray method was successfully proposed [83, 84] and

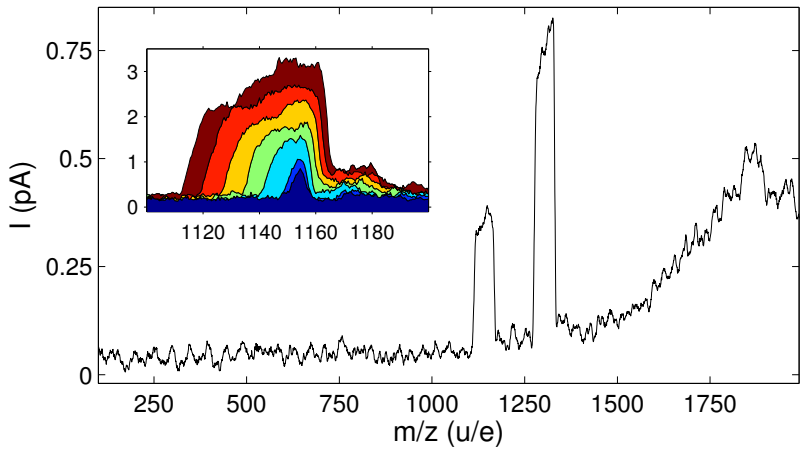

FIGURE 4.1: *Mass Spectrum of β– and γ–Cyclodextrin.*
The mass spectrum is showing two peaks corresponding to two different oligosaccharides and a broad distribution of beam impurities from $m/z > 1500$ u/e. The inset shows a series of scans at different resolutions. As the resolution is decreased, the current increases and the peak shifts to lower masses.

present the first STM / STS data of single N3 molecules, which belong to this class of substances.

The entirety of our experiments proves, that the ion beam flux is sufficient to produce coverages well suited for STM investigation for a number of very different substances. Furthermore the impurity density and fragmentation ratio is kept low.

The STM experiments were carried out at a pressure of 5×10^{-11} mbar and a temperature of 6 K with etched tungsten tips. The noble metal substrate surfaces were cleaned by ion bombardment and annealing.

To test the correct operation of the quadrupole mass filter in combination with the ion funnel, we performed experiments using different cyclodextrins (cyclic oligosaccharides). A mixture of β– and γ–cyclodextrin was dissolved in a 1:1 mixture of water and methanol and 1 % of acetic acid. A mass spectrum was aquired at a resolution of $m/\Delta m = 25$ (Figure 4.1). At this setting we can clearly distinguish rectangular peaks corresponding to β–cyclodextrin (nominal mass of 1135 u) and γ–cyclodextrin (nominal mass of 1297 u/e) as well as a broad distribution of particles beginning from $m/z \approx 1500$ u/e. From this mass scan it is obvious that the measured mass is higher than the nominal mass of the cyclodextrins.

In a series of scans (inset in Figure 4.1) the resolution was increased gradually (from red to blue). From high resolution mass spectra (blue curve in the inset of Figure 4.1) the masses of the ions can be read to be ≈ 1154 u and ≈ 1316 u. This mass discrepancy can be explained either by the hydrolysis of the cyclodextrins to maltoheptaose and maltooctaose respectively [85] and additional charging by protonation, by charging by

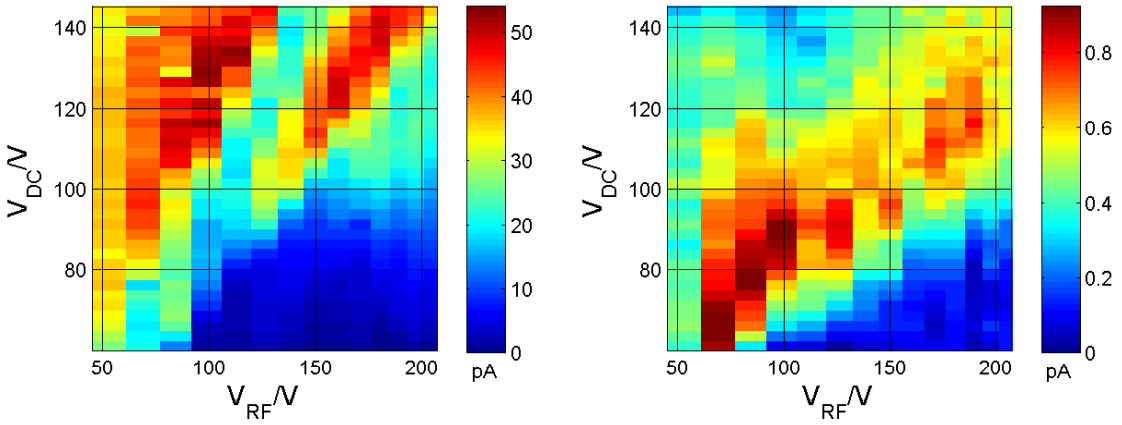

FIGURE 4.2: *Experimental Ion Funnel Transmission Diagram.*
The absolute transmission for $m/z > 880$ u/e *(left diagram) exhibits different regions of high transmission. The measured current mostly consists of multiple charged droplets, heavy enough not to be damped efficiently by the background gas at a pressure of* 10 Pa. *The mass selected current (right diagram)* $m/z \approx 1150$ u/e *is more intense at lower DC and RF voltages. The slight stripe pattern is an artefact of the measurement mode (scanning all DC voltages for one RF voltage consecutively) and variation in the ion current produced by the ion source.*

a hydronium ion (H_3O^+), or by protonation and the inclusion of a water molecule. The weak peak at ≈ 1172 u at lower resolution in the inset in Figure 4.1 can be explained by the inclusion of one additional water molecule in the cyclodextrin cage. At high resolution our setup can provide the information whether the used molecules are still intact. In addition, the attachment of solvent molecules can be detected. For deposition experiments the resolution can usually be lowered to increase the transmission of the quadrupole while still eleminating undesired ions.

The distribution of ions at high mass to charge ratios is most probably due to incompletely desolvated droplets. Without the opportunity of using the mass filter during deposition, these droplets would impinge on the surface and result in impurities. During deposition experiments it should be feasible to separate the oligosaccharides from background impurities.

The mass spectra at different resolution settings in the inset in Figure 4.1 illustrate how the transmission decreases while the resolution is increased. Since the left flank of the peak moves faster to low masses than its right flank to high masses as the resolution is decreased, the mass of the ion appears to shift to lower masses (compare Page 18).

One of the most challenging steps during a deposition experiment is the optimization of the ion funnel transmission by adjusting the corresponding settings. To confirm the simulated results for the transmission efficiency of the ion funnel in Sec-

tion 3.4.1, the RF voltage and second funnel stage DC voltage were varied over the complete range of available voltages and the transmission efficiency for β–cyclodextrin alone as well as the integrated ion current were measured.

For this experiment β–cyclodextrin in a 1:1 mixture of water and methanol and 1 % of acetic acid was used. The DC voltage of the first stage was kept constant at 150 V, the pressures in the ion funnel vacuum chambers were 10 Pa and 24 Pa respectively. To increase the influence of the undesolvated droplets no counter gas flow and no heating of the desolvation capillary were applied. The ion current was measured directly behind the quadrupole mass filter.

This way the two transmission plots of Figure 4.2 were acquired. Using the mass filter to select the oligosaccharide ions (right plot) results in a region of high transmission at relatively low RF and DC voltages. Operating the mass filter in the high pass mode results in a transmission diagram exhibiting strong substructure, comparable to the predicted low pressure transmission plots in Figure 3.9. In this case the detected current consists mainly of charged droplets, having a broad distribution of mass to charge ratios. Because the background pressure in the ion funnel chambers is not high enough to damp the macro–oscillations of these heavy droplets in the effective potential efficiently, the transmission plot is more similar to the one of single ions at lower pressure.

The results of this section prove that the in–line quadrupole mass spectrometer can be used to characterize the ion beam. In addition it can improve the achieved sample quality by filtering out impurities during deposition. The experimental ion funnel transmission plots are in good qualitative agreement with the ones predicted from the simulations in Section 3.4.1.

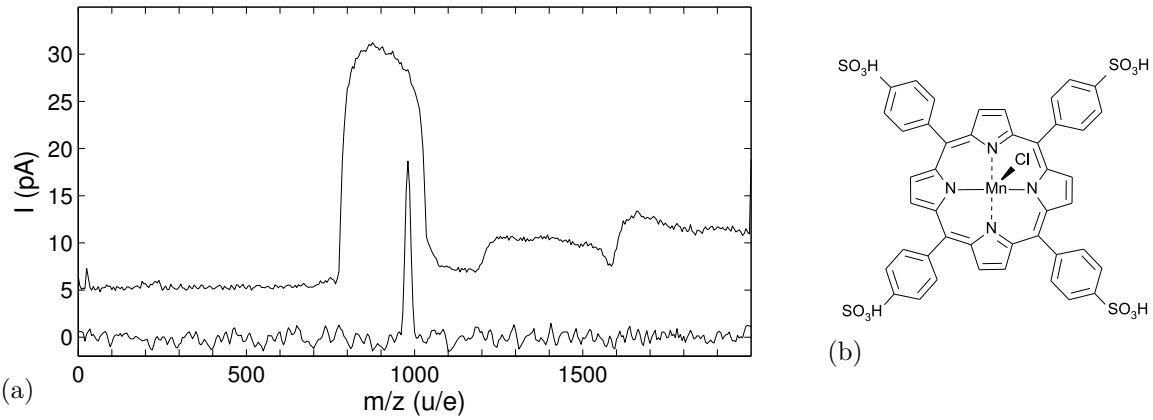

FIGURE 4.3: *Mass Spectra and Molecular Structure of MnTPPS.*
(a) Two mass spectra acquired at different mass resolution settings. The top spectrum is offset by 5 pA *and acquired at conditions identical to those used for the deposition. The spectra were acquired using an auxiliary electrode. For this reason the measured currents are slightly higher than during the deposition. (b) Schematic molecular structure.*

4.1 Manganese Tetraphenylporphine Sulfonate

Porphyrins are a class of water–soluble pigments many of which occur in biological systems. They are composed of four modified pyrrol rings interconnected by methine (=CH-) bridges. Their derivatives include haemoproteins, which are porphyrins with a central metal atom and an attached protein, such as haemoglobin, catalase and cytochrome. A well–known example of the porphyrins is the red pigment haem, which is a compound of the haemoglobin and exhibits an iron atom as central metal atom. Another example is the green chlorophyll, responsible for the photosynthesis in higher plants. The porphyrin cycle possesses 22 π–electrons and therefore they are aromatic due to Hückel's rule for aromaticity ($4n+2$ π–electrons with $n=5$). The cycle is highly–conjugated and the π–electrons are completely delocalized. As a direct consequence porphyrins usually possess strong absorption bands for visible light and have deep colours.

Due to their special properties porphyrins have become important in many technical applications as well. They are, for example, one class of substances used as photosensitizer in Photodynamic Therapy (PDT) [86] in clinical practise. These photosensitizers are modified in a way to bind to specific tissue with a certain degree. They can be activated by light of a specific wavelength and transfer the energy of the light to oxygen to form singlet oxygen, which inflicts severe damage to the surrounding tissue [87]. Other applications are the use as model systems of photochemical reactions [88], biomimics of enzymes (such as Cytochromes [89]), et cetera.

Porphyrins are well suited for investigations by STM because of their high recognition value and the possibility to deposit them by thermal deposition. Many STM studies were already carried out on different derivatives investigating the adsorption geometry [90], changes of the conformation due to the metal substrate [91–95], temperature dependent assembly [96], in–situ metalation [97] and intermixed porphyrin layers [98] (just to mention some of them).

In our experiments the porphyrin 5,10,15,20-Tetrakis(4-sulfonatophenyl)-21H,23H-porphine manganese (III) chloride (MnTPPS-Cl; $m = 1023.36$ u; Frontier Scientific Inc.; schematic molecular structure in Figure 4.3(b)) was dissolved in a mixture of methanol, water (ratio 1:1) and 1 vol% acetic acid at a concentration of ≈ 0.5 mM. The solution was sprayed at a flow rate of 100 µl/h in positive ion mode at 4.6 kV. In the high resolution mass spectrum ($m/\Delta m \approx 100$; Figure 4.3(a) lower spectrum) a single peak can be observed at $m/z = (985 \pm 10)$ u/e originating from the MnTPPS cation without the detached Cl^- ($m = 35.45$ u). No fragments can be detected in the provided mass spectra. For deposition, the resolution was reduced to $m/\Delta m \approx 5$ (compare mass spectrum in Figure 4.3(a) upper spectrum) almost doubling the ion current to an average of 15 pA which could be maximized to 20 pA directly after cleaning the desolvation capillary and spray tip. Deposition on a Au(111) surface was performed for 6 h for the sample shown in Figures 4.4 and 4.5(a) to 4.5(c) resulting in nominal coverages[1] of about 20 % of a monolayer. During deposition the impact energy was set to (13.5 ± 5) eV (≈ 50 meV per degree of freedom of the MnTPPS molecule), which is low enough to keep molecules and surface intact. Afterwards the sample was softly annealed at 50°C for 10 minutes to enhance island formation.

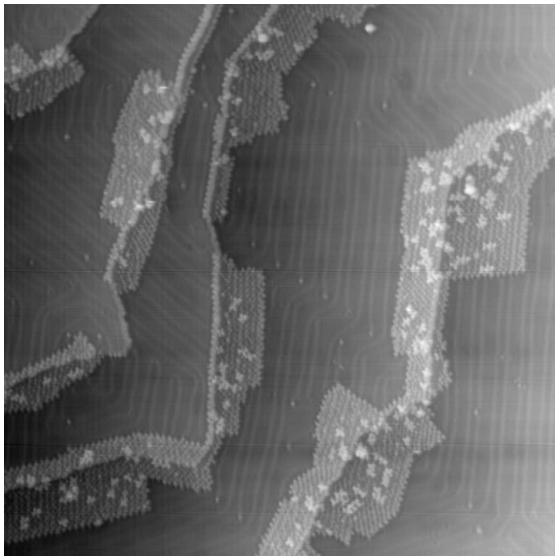

FIGURE 4.4: *MnTPPS on Au(111). Surface area covered by more than* 25 % *($I = 19$ pA; $V_S = 0.43$ V; 85×85 nm^2; $\Delta Z = 7$ Å).*

The STM images[2] in Figures 4.4 and 4.5 show self assembled MnTPPS islands on the reconstructed Au(111). Due to beam filtering and low residual gas pressure during the sample preparation, almost no contamination is observed. After covering the

[1] The nominal coverage equals the number of molecules times their unit cell area divided by the surface area.

[2] All STM images in this thesis are processed with WSxM [99].

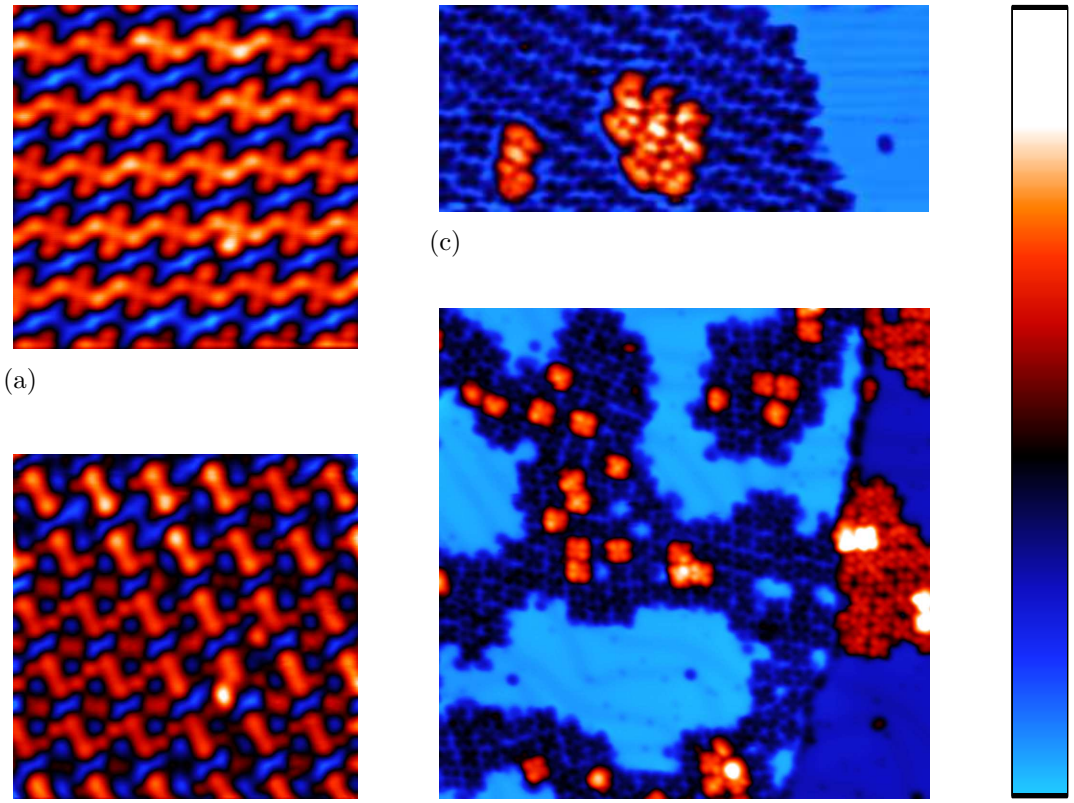

FIGURE 4.5: *Growth of MnTPPS on Au(111).*
(a) Intra–molecular structure of MnTPPS (compare Figure 4.3(b)) ($I = 23$ pA; $V_S = 2.7$ V; 9×9 nm^2; $\Delta Z = 1.6$ Å); (b) saddle conformation (see text) ($I = 23$ pA; $V_S = -3.2$ V; 9×9 nm^2; $\Delta Z = 1.6$ Å); (c) long range ordered MnTPPS island after annealing ($I = 10$ pA; $V_S = 2.7$ V; 28×12 nm^2; $\Delta Z = 11$ Å); (d) single second layer MnTPPS molecules ($I = 20$ pA; $V_S = 2.7$ V; 50×50 nm^2; $\Delta Z = 9.1$ Å).

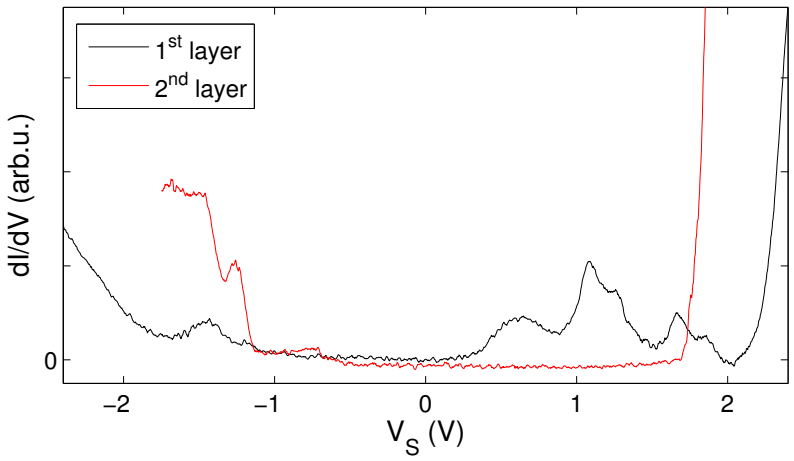

FIGURE 4.6: dI/dV–*Spectra of First and Second Layer MnTPPS Molecules. The red spectrum acquired on a single second layer MnTPPS molecule exhibits a HOMO–LUMO gap of* 2.8 eV. *The coupling of the first layer molecule to the substrate (black spectrum) gives rise to additional electronic states.*

complete step edge, almost perpendicular growth into the upper as well as the lower terrace can be observed. The oblique unit cell measures approximately 17 Å × 19 Å and has an angle of 70° between the primitive vectors. The rod like shape of the molecule at high negative sample voltages (Figure 4.5(b)) with twofold symmetry can be assigned to the so–called saddle form as reported in References [91, 94] and is caused by bending two of the four pyrrole rings up and down, respectively.

A significant number of molecules can be found on top of these island. A comparison of the numbers of molecules directly on Au(111) and on top of molecular islands indicates that MnTPPS molecules deposited on an island cannot descent to the substrate. This fact opens the possibility to observe the fairly undisturbed electronic structure of a single molecule by STS. In Figure 4.6 two dI/dV–spectra, one acquired on a molecule in an island directly on the gold surface (black) and the other acquired on a single second layer molecule (red) are shown. The red spectra exhibits a HOMO–LUMO gap of approximately 2.8 eV between −1.1 V and 1.7 V. The electronic structure of the first layer molecule is significantly modified.

The sample shown in Figure 4.5(d) was prepared at ambient temperature using an impact energy of less than 10 eV. At these conditions the molecular layer does not form long range order.

The results of this section indicate that the presented electrospray deposition apparatus is capable of achieving sample qualities similar to thermal deposition. In addition, we were able to deposit second layer molecules without completing the first layer.

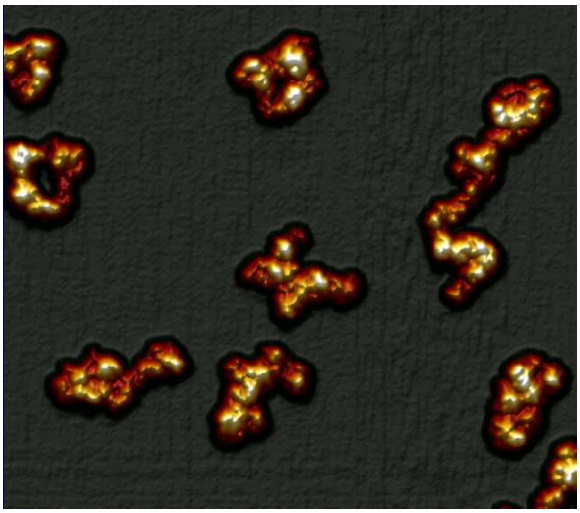

FIGURE 4.7: *STM Image of BSA. Several BSA molecules on the atomically flat Ag(111) surface ($I = 8$ pA; $V_S = 1.75$ V; 100×120 nm^2; $\Delta Z = 4.5$ Å). Investigation of the crystal structure of HSA resulted in a unit cell size of $a = 54.8$ Å, $b = 55.6$ Å, $c = 120.3$ Å, $\alpha = 81.2°$, $\beta = 91.1°$ and $\gamma = 64.3$ Å which should be a good estimation for the size of a BSA monomer [100].*

4.2 Bovine Serum Albumin

To demonstrate deposition of large biomolecules bovine serum albumin (BSA) was chosen. BSA deposited on HOPG by the electrospraying technique has already been investigated using scanning probe techniques [9]. BSA is a serum albumin protein having a variety of biochemical applications. Since BSA can be purified from cattle blood (by–product of the meat industry) it is readily available. BSA has a molecular weight of 66430 u, is a single polypeptide chain consisting of 583 amino acids and contains 17 intrachain disulfide brides and one sulfhydryl group in neutral solution [101]. The Stokes radius of BSA is 3.48 nm [102] which can be used as a first estimation for the molecular size measured in STM.

BSA (Sigma-Aldrich Corp., St. Louis, MO) has been sprayed in positive ion mode with a spray voltage of 4.6 kV from a solution of methanol, water (ratio 3:1) and some acetic acid ($pH = 4$) on a Ag(111) surface. The quadrupole mass filter was operated in the RF–only mode to block charged solvent particles. Deposition was performed for 30 min at a current of 30–50 pA to a total dose of 22.5 pAh at an impact energy of 8.5 ± 3 eV per charge.

In the topography in Figure 4.7 one can clearly distinguish several BSA molecules. The size of single BSA molecules on mica was obtained from tapping mode AFM images to be 12.2 nm $\times$ 6.2 nm (tip radius broadening subtracted)[103]. Therefore we can conclude that the features in Figure 4.7 are clusters of just a few BSA molecules. AFM images of BSA deposited on HOPG by the electrospraying technique [9] are comparable to our results as well.

We showed, that our instrument is capable of depositing molecules of high masses (≈ 66000 u in this example) which are well separated on the surface without any disturbing impurities.

4.3 Deoxyribonucleic Acid

Deoxyribonucleic acid (DNA) exists in all living organisms (except some viruses) and carrys the genetic information. It is a polymer composed of the so–called nucleotides, which consist of a backbone made of a phosphate group and the sugar 2–deoxyribose and of one of the four organic bases adenine, thymine, guanine, and cytosine (abbreviated A, T, G, and C). Normally two DNA strands are arranged in the shape of a double helix.

Today the most common DNA sequencing techniques are based on electrophoresis methods. DNA sequencing revolutionised biology and has become a standard procedure in medical and biology laboratories.

During the last two decades attempts have been made to directly read the sequence of a single DNA molecule, especially using the nanopore, transmission electron microscope (TEM), and STM techniques. Single DNA molecules were detected using an α–hemolysin nanopore [104], which was also found to discrimintate between purine and pyrmidine based nucleotides [105, 106]. A specific labeling technique was developed to visualize the DNA sequence by TEM with the shadow casting method[3] [107]. Using STM to resolve the electronic structure of single DNA molecules may become a powerful sequencing tool as well. Using the atomic scale resolution, it should be possible to identify the four nucleobases (adenine, thymine, guanine, and cytosine) and determine the base sequence of particular single–stranded DNA molecules (ssDNA) in real space. Many attempts to sequence DNA molecules by STM have been made, but preparing samples with reproducable quality was difficult and limiting the progress in this field [3, 108].

Early high resolution images (especially from 1989 and 1990) of what was believed to be DNA have later been attributed to structures of the highly orientated pyrolytic graphite substrates used, on which the DNA was drop casted [108].

Actual intramolecular resolution required to probe the electronic structure of a single DNA molecule has so far been achieved for only a few STM experiments.

A pulse injection method has been developed to deposit DNA oligomers from aqueous solution and to prevent artifacts, contaminations, decomposition, and aggregation [3]. The Cu(111) substrate used maintained its atomic flatness and the DNA oligomers were found to be intact and did not form agglomerations. Using pulse injection, it was possible to visualize the secondary structure (double helix) of DNA and achieve a resolution high enough to identify individual nucleotides, which allows a partial sequencing, utilizing the different sizes of the nucleotides [109]. STM and STS were performed on single DNA oligomers attached to fluorescein isothiocyanate dye [110]. The STM images showed the dye molecule and the individual bases. The possibility of identifying the four different nucleotides by STS was discussed. Later

[3]For shadow casting a metal is deposited from a source at a certain angle of incidence.

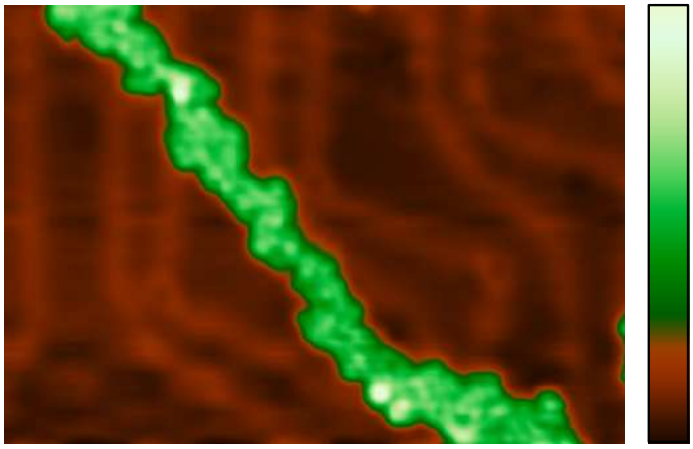

FIGURE 4.8: *STM Image of DNA on Au(111).*
A string of DNA molecules on the atomically flat, reconstructed gold surface (I = 30 pA; $V_S = 0.5$ V; 36×26 nm^2; $\Delta Z = 6$ Å).

on it was found that the guanine bases have a distinct electronic state and can be distinguished from the other bases [111].

As ESI can provide gas phase ions of non–covalent bound compounds like double–stranded DNA (dsDNA) [112] as well as ssDNA, we used the ESI source to deposit DNA on clean noble metal surfaces in UHV. In addition our setup can further reduce the amount of contaminations for oligonucleotides of a known sequence by carefully adjusting the mass transmission window and prevent, for example, the coadsorption of sodium ions attached to the DNA in solution.

For our first experiment we used a 20 µM solution of salmon sperm DNA of low molecular weight in a mixture of acetonitrile, water (2:1) and 0.1 vol% of triethylamine. The molecules were sprayed in the negative ion mode at a voltage of −3.5 kV for 3 h resulting in a dose of 60 pAh. As the DNA molecules are fragments of natural grown DNA their sequences, lengths and masses vary. Mass spectra showed a broad distribution in the range from $m/z \approx 1000$ u/e to 1500 u/e corresponding to multiply charged DNA. During the deposition the mass spectrometer was set to transmit the m/z-range from ≈ 825 u/e to ≈ 2500 u/e, which filters out low mass impurities, such as solvent ions.

Figure 4.8 shows a typical constant–current image of the prepared surface. While most of the substrate is free from adsorbates and exhibits the typical herringbone reconstruction, the deposited molecules have arranged into a string. The apparent width and height of the molecular structure in the image are ≈ 20 Å and ≈ 2 Å, respectively. While the apparent height in STM images may be significantly affected by electronic effects, the width of the string is more significant despite a possible influence of the shape of the STM tip. The strand shown in Figure 4.8 is most likely

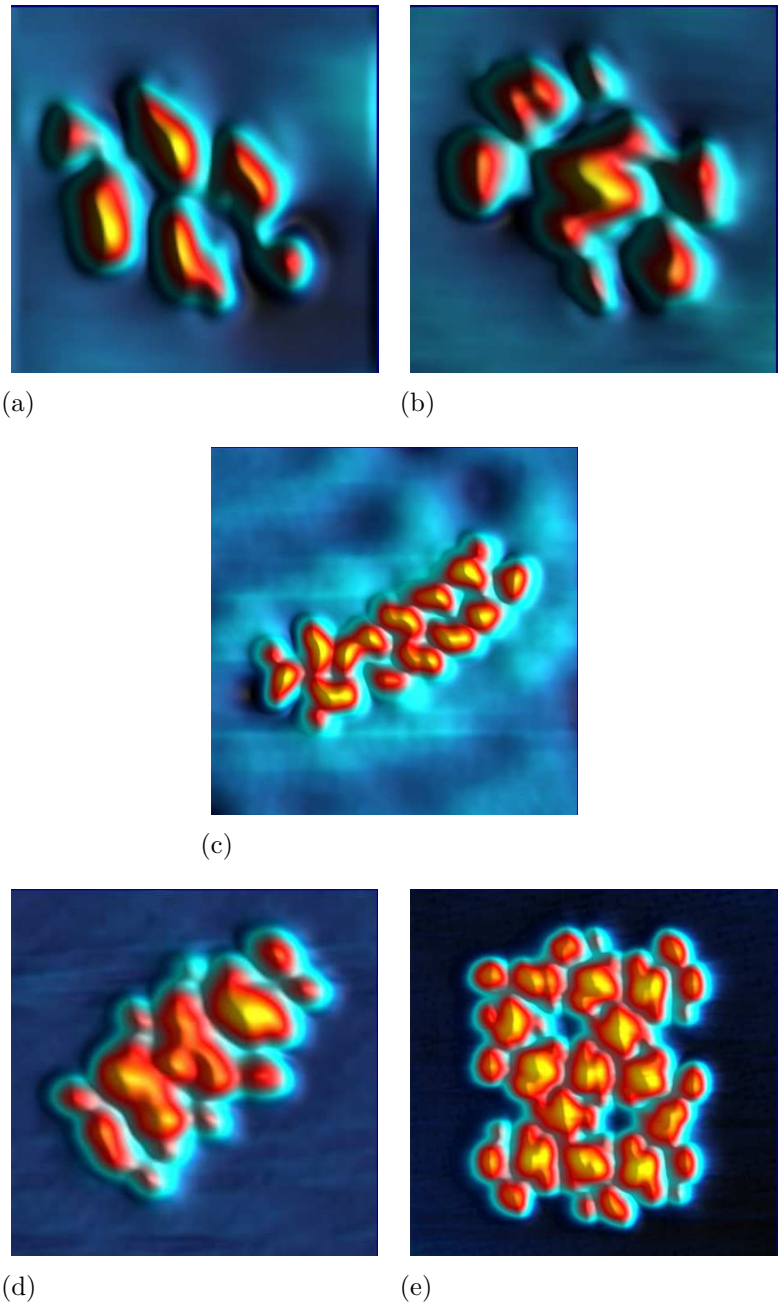

FIGURE 4.9: *STM Images of the T5C7 Oligonucleotide.*
The T5C7 oligonucleotide arrange into different structures of which especially the monomer and dimer can be observed more often; (a) monomer ($I = 50\,\mathrm{pA}$; $V_S = -20\,\mathrm{mV}$; $5 \times 5\,\mathrm{nm}^2$; $\Delta Z = 1.8\,\text{Å}$); (b) dimer($I = 50\,\mathrm{pA}$; $V_S = -20\,\mathrm{mV}$; $7.5 \times 7.5\,\mathrm{nm}^2$; $\Delta Z = 1.9\,\text{Å}$); and different types of oligomers (c) ($I = 8\,\mathrm{pA}$; $V_S = 50\,\mathrm{mV}$; $11 \times 11\,\mathrm{nm}^2$; $\Delta Z = 1.8\,\text{Å}$); (d) ($I = 8\,\mathrm{pA}$; $V_S = -1.1\,\mathrm{V}$; $10 \times 10\,\mathrm{nm}^2$; $\Delta Z = 4\,\text{Å}$); (e) ($I = 10\,\mathrm{pA}$; $V_S = -1.1\,\mathrm{V}$; $13 \times 13\,\mathrm{nm}^2$; $\Delta Z = 2.4\,\text{Å}$).

composed of one or two ssDNA molecules. We note that the level of detail of the STM data in Figure 4.8 is comparable to the best data reported to date in Reference [111].

Next we deposited an oligonucleotide of a known base sequence on Au(111) to gain further information on the topographic and electronic feature of the different bases. As a simple approach the oligonucleotide T5C7 was used, which has the base sequence TTTTTCCCCCCC. It has a molecular mass of 3483 u. The deposition procedure was similar to the one described above. This time the mass filter was set to $m/z = 1160$ u/e, corresponding to the three times charged oligonucleotide showing the highest ion current, with a resolution of $m/\Delta m = 8$. The deposition took 2.5 h and the charge added up to 40 pAh. After deposition the sample was slightly annealed at 100 °C for 20 min. We found the molecules to arrange in different structures, of which the smallest one was assigned to the monomer (Figure 4.9(a)) and the second smallest to the dimer (Figure 4.9(b)). These two structures were observed several times. In addition we found different types of oligomers, the most symmetric of them are shown in Figures 4.9(c) to 4.9(e). The interpretation of the topographical structure of the monomer and dimer and the mechanism resulting in the oligomer formation is still in progress.

The results presented in this section demonstrate that ESI deposition is useful in obtaining the high sample quality reported from pulsed injection. In addition mass separation can be applied to further reduce the risk of potential artifacts and contaminations. The formation of oligomers observed in our experiments can be assigned to the sample tempering after deposition. Our results as well as the ones presented in the literature [3, 109, 110, 113] indicate, that it will be quite difficult to determine properties of the nucleotides and realize sequencing from STM topographies alone. However we expect that using the instrument described in this thesis, it should be possible to determine properties of the four bases adenine, thymine, guanine, and cytosine by using STS or AFM in near future.

4.4 Free Ligands of Metal–Organic Grid Complexes

The construction of metal–organic complexes with well–defined structures by self–assembly is of current interest in supramolecular chemistry. When the used organic ligands contain the correct binding sites, a spontaneous formation of a desired inorganic architecture is formed in combination with the metal ions [114].

Supramolecular grid structures consisting of four Co^{II}–atoms and four organic ligands (such as bis(bipyridyl)-pyrimidine ligands) were reported to exhibit an antiferromagnetic coupling of the Co^{II}–spins. This coupling was found to have only intramolecular origin and does not depend on the physical conditions, making these grids an almost ideal quantum spin system [115].

Thin films of supramolecular grid structures on Au(111) were prepared by electrochemical deposition and characterised by in–situ STM [116] and found to form ordered structures. The morphologies of different [2×2]–grid–type Fe^{II} complexes on HOPG were studied by STM, coming to the conclusion that long alkyl chains attached to the organic ligands favour the organization of the molecules and therefore improve the applicability of STM [117]. The metal centres of [2×2]–grid–type Co^{II} complexes on HOPG were imaged by STM with submolecular resolution and addressed by STS [118].

We deposited two different organic molecules (see below) **A** (bis(bipyridyl)-phenylpyrimidine) and **B** (a bis(pyridylhydrazone)-phenylpyrmidine derivative), which are also used as ligands for [2×2]–grid–type metal complexes, on a Au(111) surface. The deposition of 50 pAh of molecule **A** (~ 30 pA for 100 min) results in well separated molecules as shown in Figure 4.10, just some of them are forming dimers.

As the bispyridyl–groups are free to rotate in the gas phase, different conformations of the molecule can be found after adsorption, which are shown in Figure 4.11. The schematic structures can explain these conformations quite well. The type shown in Figure 4.11(b) exists in two mirror symmetric subtypes and is the most common one. The conformation in Figure 4.11(c) is preferably found on the elbows of the herringbone reconstruction with the four nitrogen atoms of the pyridyl ring directly pointing towards the elbow site. It shoud be mentioned that molecule **A** is rather small, regarding its mass of 464 u, nevertheless the presented deposition setup –and

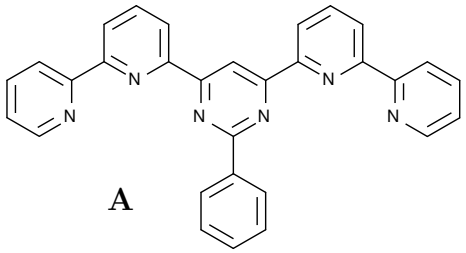

A

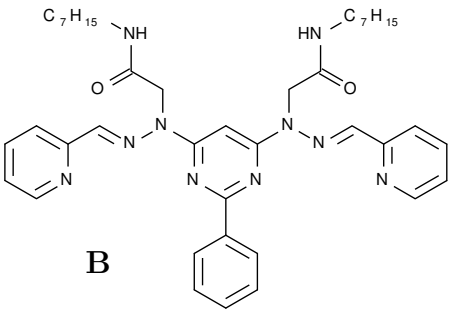

B

!t 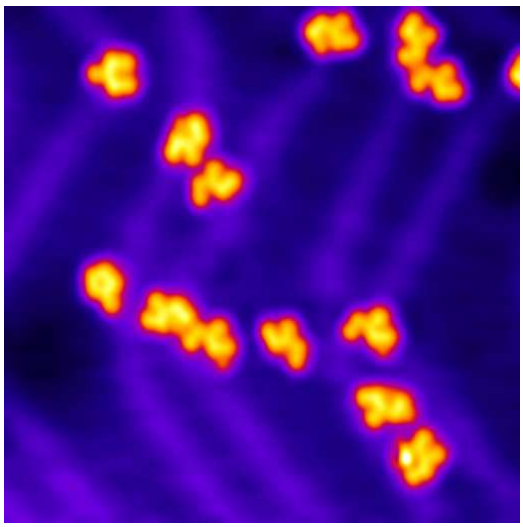

FIGURE 4.10: *Molecule **A** on Au(111). STM image of bis(bipyridyl)–phenylpyrimidine (**A**) on the reconstructed Au(111) surface ($I = 10\,\mathrm{pA}$; $V_S = -0.35\,\mathrm{V}$; $15 \times 15\,\mathrm{nm}^2$; $\Delta Z = 1.8\,\mathring{A}$). Three different molecular conformations can be identified as shown in Figure 4.11.*

the employed ion funnel design in particular– provides a useful ion flux.

Molecule **B** was deposited at two different coverages. At a low coverage (15 pAh, Figure 4.12(a)) the molecules form chains, most of them parallel to the herringbone reconstruction. At higher coverages these chains merge into a more or less random network. For molecule **B** the achieved ion current is quite high (70 pA in average, peak currents of more than 110 pA). This is most probably caused by the hydrophobic heptyl chains, which support droplet desolvation. In contrast to other reported STM measurements on HOPG [119] we do not find the alkyl chains supporting formation of regular structures at higher coverages on the Au(111) surface.

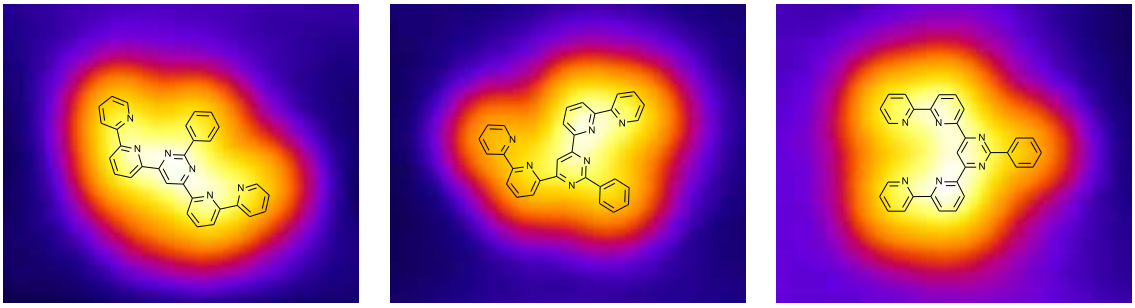

(a) (b) (c)

FIGURE 4.11: *Different Conformations of Bis(bipyridyl)–phenylpyrimidine (**A**). Detailed view of the three different conformations, including molecular schematics (all images acquired at the same condition, $I = 10\,\mathrm{pA}$; $V_S = -0.35\,\mathrm{V}$; $2.5 \times 2.1\,\mathrm{nm}^2$; $\Delta Z = 2\,\mathring{A}$).*

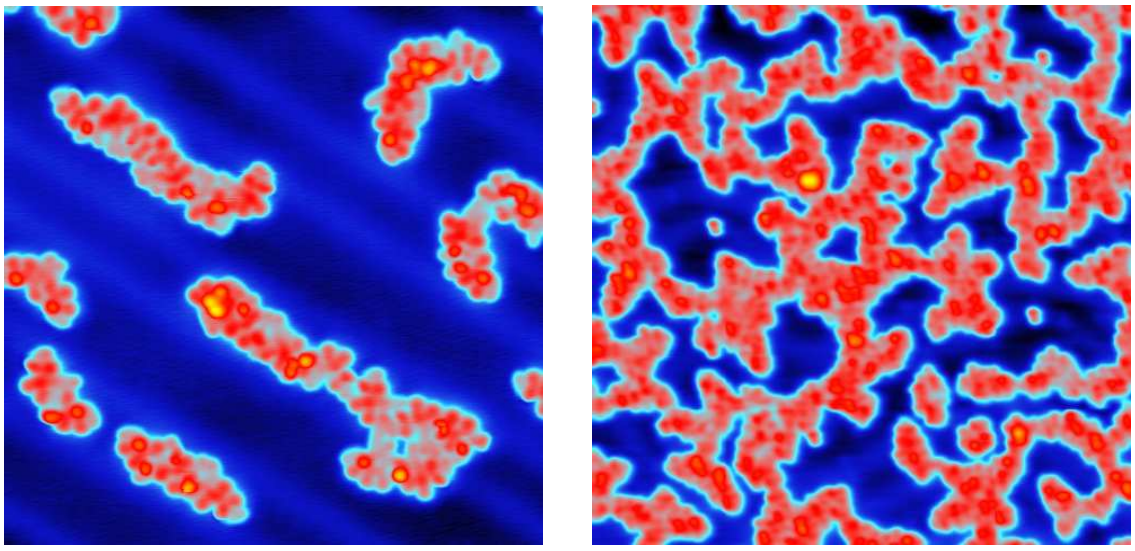

(a) (b)

FIGURE 4.12: *Growth of Bis(pyridylhydrazone)-phenylpyrmidine (**B**) on Au(111). (a) At low coverage (*15 pAh*) the molecules arrange into chains (*$I = 40$ pA*; $V_S = -0.22$ V; 20×20 nm^2; $\Delta Z = 2.5$ Å); (b) at higher coverages (*350 pAh*) a random network is formed (*$I = 50$ pA*; $V_S = -3.0$ V; 30×30 nm^2; $\Delta Z = 3.5$ Å).*

Previous STM data from metal–organic grid complexes or the corresponding ligand molecules are not very detailed [116] or were acquired on HOPG [117–119]. In this regard we would like to mention again the concern about structural investigations on HOPG in Reference [108], due to the variety of structures on the pure HOPG. High resolution STM studies of the metal–organic grids or their ligands on other surfaces should be used to confirm the results obtained so far. We hope to be able to participate in this field by use of the electrospray deposition technique.

The results presented in this section prove on the one hand that it is possible to deposit organic molecules of low m/z (< 500 u/e), and on the other hand we were able to show that (depending on the substance to deposit) ion currents in the order of 100 pA can be achieved, allowing for growth rates of ten percent of a monolayer per hour.

4.5 N3: A Ruthenium Based Dye for Solar Cells

Dye–sensitized solar cells (DSC), also known as Grätzel cells[4], are technically attractive because they are made of low–cost materials, are easy to manufacture, can form flexible sheets and cause little pollution [120]. The most common design is based on a photo–sensitized anode, an iodide electrolyte and a platinum cathode. The anode is formed by a transparent film of titanium dioxide (TiO_2) nano particles, which are coated by a monolayer of a covalent bound molecular dye to sensitize the device for visible light. The TiO_2 film is contacted by a transparent fluoride–doped tin dioxide thin film.

Because of the high surface area of the TiO_2 and the optimized spectral characteristics of the dye, power conversion efficiencies over 10.5 % were achieved in recent cells [121].

Light passing the transparent anode can excite electrons in the dye layer from the HOMO to the LUMO, which then are injected into the conduction band of the TiO_2 and can be collected by the anode. The depleted state of the dye molecule can then be replenished by stripping one electron from iodide in the electrolyte, which is thus oxidized into triiodide.

Ruthenium based dyes, such as N3 (cis-bis(isothiocyanato)bis(2,2'- bipyridyl-4,4'-dicarboxylato)-ruthenium (II), schematic structure in Figure 4.13(c)), the related N719, and so–called black dye are photoactive complexes used in dye sensitized solar cells (DSCs). They are the most efficient sensitizers for DSCs known so far. Using these dyes to sensitize nanoporous TiO_2 resulted in solar cells with very high quantum efficiency for visible light [122–124].

One of the major problems of this kind of solar cells is the sealing which should prevent the electrolyte from leaking. A solution to this problem would be to replenish the HOMO via a metal film instead of electrolyte containing a redox system such as iodide, so adsorption of a gold layer on the TiO_2 was proposed in References [125, 126].

Since the Ruthenium based dyes are thermally unstable they cannot be deposited by sublimation. This problem can be circumvented by using electrospray deposition as shown very recently for deposition on a TiO_2(110) surface [83] as well as on a Au(111) surface [84]. STM and STS measurements presented in this section are (to the best of our knowledge) the first ones investigating single N3 molecules.

Because the cell conversion efficiency depends strongly on the molecule–substrate interface and the properties of the dye the investigation of the adsorption of single molecules and their electronic structure might give fundamental insight to functionality of DSCs.

Here we present experimental data of N3 deposited on a Ag(111) surface. A 0.35 mM

[4]invented by Michael Grätzel and Brian O'Regan

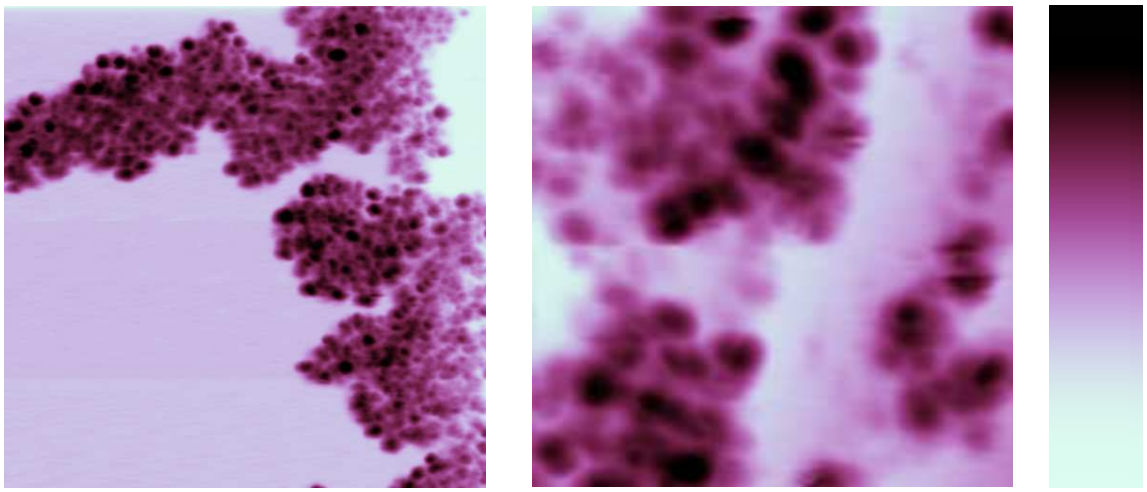

(a) (b)

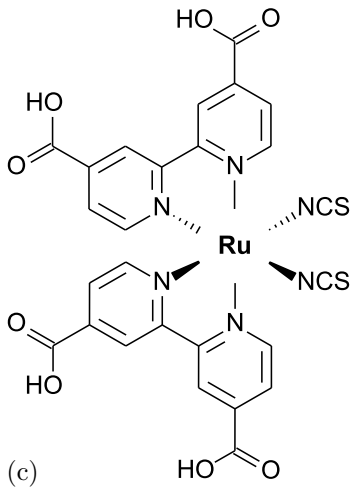

(c)

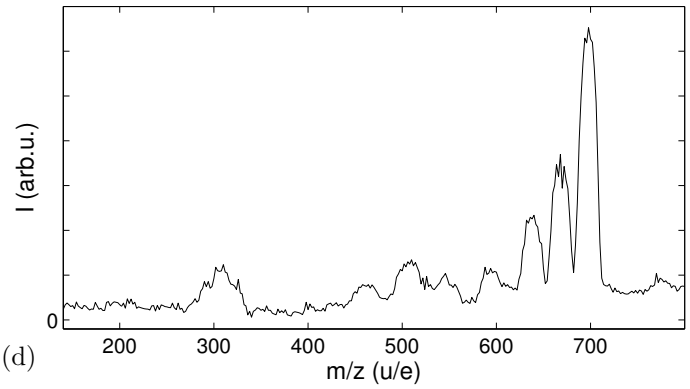

(d)

FIGURE 4.13: *STM Images of N3 on Ag(111).*
(a) Agglomerations of N3 molecules on a Ag(111) step edge ($I = 8\,\mathrm{pA}$; $V_S = 1.4\,\mathrm{V}$; $60 \times 60\,\mathrm{nm}^2$; $\Delta Z = 11.6\,\text{Å}$); (b) detailed view of an N3 agglomeration ($I = 6\,\mathrm{pA}$; $V_S = 1.7\,\mathrm{V}$; $20 \times 20\,\mathrm{nm}^2$; $\Delta Z = 9.8\,\text{Å}$); (c) schematic molecular structure of N3; (d) ESI mass spectrum of N3.

solution of N3 in methanol and 3 % water was sprayed at a rate of 200 µl/h and a spray voltage of 4.5 kV in negative ion mode. The impact energy during the deposition was set to 6 eV. The highest peak in the mass spectrum shown in Figure 4.13(d) corresponds to the nominal mass of the molecule of 705.64 u. The other peaks, which originate from fragments, impurities and multiple charged species can be easily filtered by the mass filter during the deposition. The ion current at the sample surface averaged 10 pA. The deposition was performed for 8 h.

The STM images in Figures 4.13(a) and 4.13(b) show bulky agglomerations of N3 molecules on the Ag(111) surface. No preferred adsorption configuration can be identified and the structure looks quite random. At the step edges of the silver surface some single molecules can be identified (Figures 4.14(a) and 4.14(b)), most of them showing a characteristic cleaved shape of the LUMO.

It is possible to irreversibly change the properties of these molecules by applying a voltage of roughly 2.5 V. STM images before and after such a change are presented in Figures 4.14(a) and 4.14(b), respectively. The shape of the LUMO looses its cleaved structure and now appears slightly higher. In the $\mathrm{d}I/\mathrm{d}V$ spectrum in Figure 4.14(c) this change can also be observed as a sudden decrease of the differential conduction. The spectrum was obtained in constant current mode at 17 pA on a single N3 molecule at a step edge. The acquisition started with the black curve at low voltages (300 mV). The voltage was continuously increased up to 2.9 V and afterwards decreased again. While decreasing the voltage (red curve) the spectroscopic features of the molecule are significantly altered. The constant height spectrum in the inset of Figure 4.14(c) shows a sudden decrease of the conduction at approximately 2.57 V which changes the electronic properties in the same way.

After this change the differential conductance of the molecules features a state with pronounced vibrational structure P^+ at positive voltages (red spectrum in Figure 4.14(c)) and a very sharp and intense peak P^- at negative sample voltages as shown in Figure 4.14(d). The peak P^- significantly shifts if the distance between the tip and the molecule is changed, as shown in Figure 4.15(b). These facts can be explained by two step tunnelling and the existence of a so–called *transient charged state* (TCS), which contributes to the tunnelling current at positive as well as negative sample voltage. This effect has already been reported for other molecules in References [127–129].

The TCS of the molecule can contribute to the tunnelling current at both voltage polarities, as visualised in Figure 4.16. The presented model demands an electronic decoupling of the molecule from the surface, which in our case could be accomplished by the three–dimensional structure of the molecule.

The TCS observed here is unoccupied when no sample voltage is applied. The energy difference between the Fermi level of the Ag and the electrostatic potential

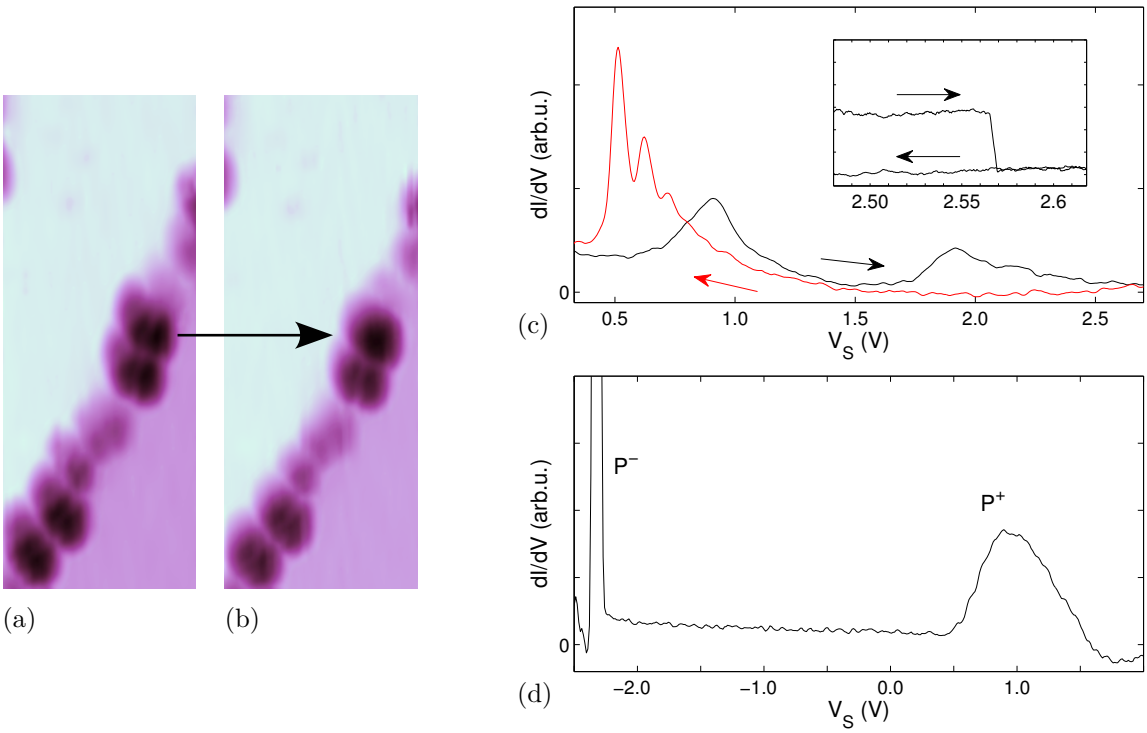

FIGURE 4.14: *STM Tip Induced Change of a Single N3 Molecule.*
(a) and (b) STM images of an N3 molecule before and after tip induced changing ($I = 6$ pA; $V_S = 1.5$ V; 8×20 nm^2) showing a change of the apparent molecular shape as well as an increase in apparent height ((a): $\Delta Z = 7.1$ Å and (b): $\Delta Z = 7.8$ Å). (c) the constant current $\mathrm{d}I/\mathrm{d}V$ spectra were obtained at 17 pA on a single N3 molecule without interruption, between the first spectrum (increasing voltage, black curve) and the second spectrum (decreasing voltage, red curve) the electronic structure was significantly altered. In the inset the change can be observed as a sharp decrease in differential conductance (constant height mode, feedback loop opened at 2.45 V, 54 pA); (d) constant height $\mathrm{d}I/\mathrm{d}V$ spectrum (feedback loop opened at -2.8 V, 26 pA) of a molecule featuring the transient charged state. The TCS is causing the features at positive as well as negative voltage.

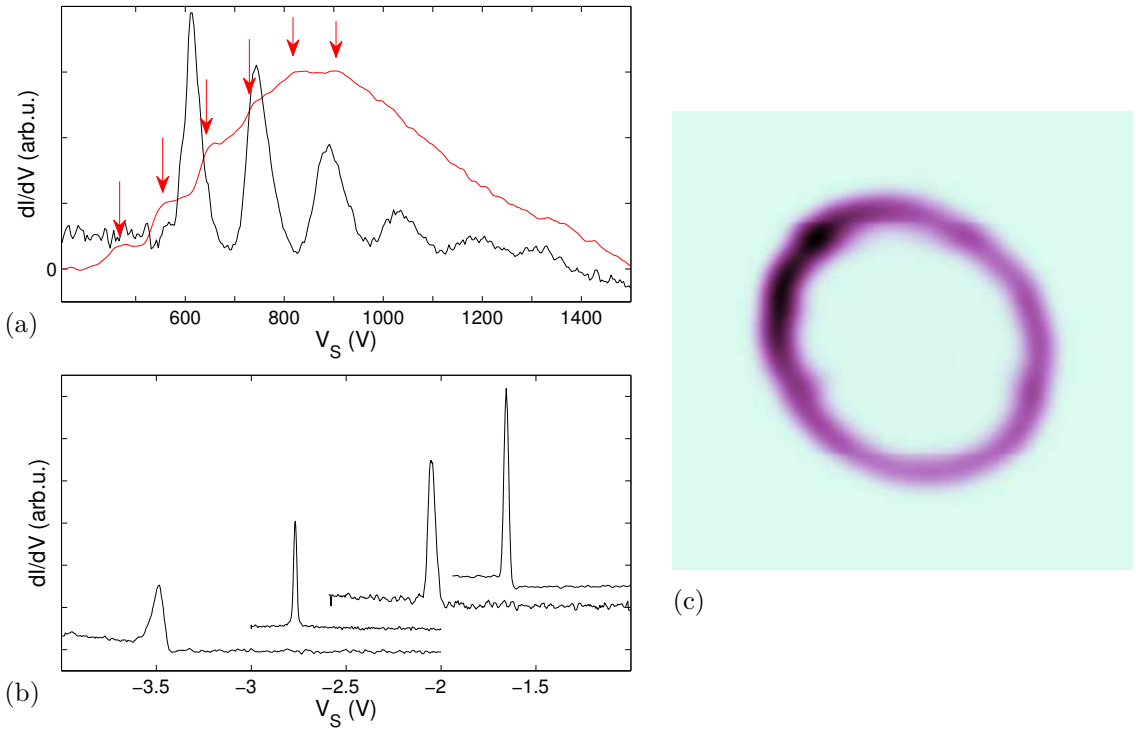

FIGURE 4.15: *Spectroscopic Features of the TCS.*
(a) Vibrational levels of the transient charged state obtained in constant current mode (black, $I = 17\,\mathrm{pA}$) and constant height mode (red, feedback loop opened at $I = 60\,\mathrm{pA}$ and $V_S = 2\,\mathrm{V}$); (b) constant height spectra visualizing the shift of the sharp peak corresponding to the transient charged state due to different tip–molecule displacements for a range of $\alpha \approx 0.1 \cdots 0.25$; (c) constant height $\mathrm{d}I/\mathrm{d}V$ map ($0.9 \times 0.9\,\mathrm{nm}^2$) showing the spatial distribution of the sharp peak for $V_S = -1.7\,\mathrm{V}$.

in the TCS of the N3 molecule can be written as $\alpha e V_S$, where V_S is the voltage applied to the Ag sample, e is the elementary charge, and α is a factor depending on the distance between the STM tip and the molecule as well as the properties of the insulating layer. This layer is most probably formed by a part of the molecule itself or another N3 molecule underneath. Two step tunnelling becomes possible when V_S is high enough to allow the energy level of the TCS E_{TCS} to align with the Fermi level of the silver at negative sample voltage or with the Fermi level of the tip at positive sample voltage. This is the case for negative voltages if

$$eV_S^- = -\frac{E_{TCS}}{\alpha} \tag{4.1}$$

and for positive voltages if

$$eV_S^+ = \frac{E_{TCS}}{1-\alpha}. \tag{4.2}$$

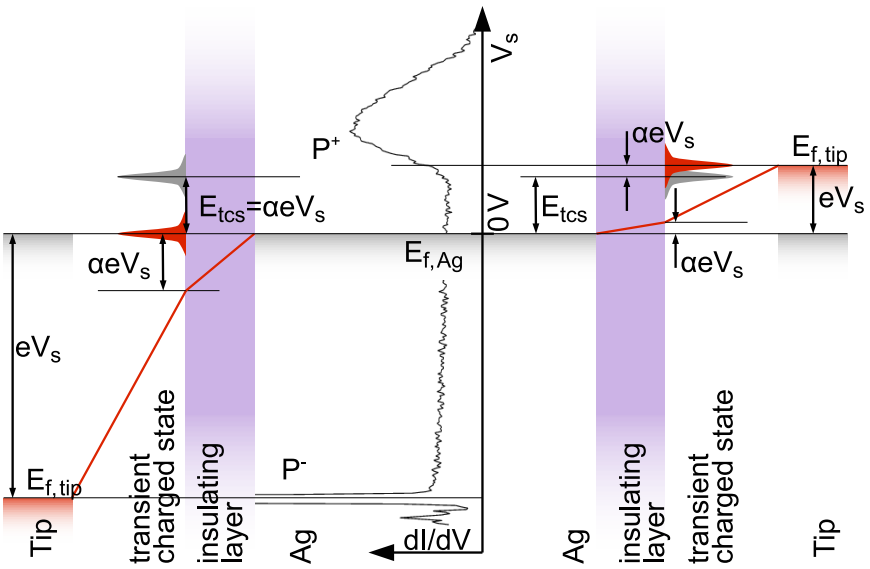

FIGURE 4.16: *Contribution of the Transient Charged State to the Differential Conductance, according to Reference [127].*
The position of the Fermi levels of the tip $E_{f,tip}$ and silver sample $E_{f,Ag}$ as well as the transient charged state E_{TCS} are marked in grey for the unbiased and red for the biased sample. In all presented experimental data the voltage V_S is applied to the sample. In this illustrative model $E_{f,Ag}$ is fixed and a tunnelling voltage of opposite polarity $-V_S$ is applied to the tip. The shape of the electrostatic potential is illustrated by the red line. The $\mathrm{d}I/\mathrm{d}V$ spectrum in the centre of the diagram assigns the two tunnelling mechanisms to the experimentally observed features. At both polarities the TCS can align with either the Fermi level of the tip or Ag and contribute to the tunnelling current.

Using the peak onsets of the peaks shown in Figure 4.14(d) ($V_S^- = (-2250 \pm 20)$ mV and $V_S^+ = (470 \pm 80)$ mV) results in an energy of the transient charged state of $E_{TCS} = (390 \pm 60)$ meV above the Fermi level and an α of 0.17 ± 0.03 for this particular spectrum.

As a simplification the factor α can also be written as $\alpha = \epsilon \cdot d/Z$, with Z being the distance between the molecule and the STM tip, and ϵ and d being the dielectric constant and thickness of the decoupling spacer, respectively [129]. All presented spectra were acquired at large Z and consequently $\alpha \ll 1$. According to Reference [129], in this case tunnelling through the spacer is much faster than tunnelling through the vacuum gap. This explains why just P^+ shows the vibronic side–bands and the side–bands of P^- are suppressed. For negative sample voltages the TCS is immediately refilled after an electron has tunnelled to the tip. Due to Coulomb repulsion no second electron can tunnel to the molecule. Therefore, the tunnelling current is only limited by the tunnelling rate from the TCS to the STM tip and becomes constant

as soon as at least one vibronic level is filled. For positive sample voltages electrons tunnelling from the tip to the TCS proceed immediately to the Ag. The vibronic levels are rarely filled, so that no Coulomb repulsion can occur and consequently tunnelling to each vibronic level is possible.

The shift of V_S^- while increasing the tip molecule separation was determined to be (-150 ± 30) mV/Å resulting in $\epsilon \cdot d = (2.6 \pm 1.0)$ Å. The ringlike feature around a molecule in the $\mathrm{d}I/\mathrm{d}V$ map at $V_S = -1.7$ V in Figure 4.15(c) corresponds to positions where the tip–molecule displacement shifts V_S^- to -1.7 V.

The different vibronic levels can be identified best in the constant current spectrum ($I = 17$ pA, black in Figure 4.15(a)) but the determination of the vibrational energy is more complicated because of the change of the factor α. The separation of the indicated peaks in the constant height spectrum (red in Figure 4.15(a), feedback loop opened at $I = 60$ pA, $V_S = 2$ V) was determined to be $\Delta E = 96 \pm 15$ meV. The energy difference of the vibrational levels is smaller by a factor of $1 - \alpha$ with $\alpha \approx 0.2$. The resulting vibrational energy of ≈ 75 meV is in an energy range called *fingerprint region* in infra–red spectroscopy, where vibrations cannot be attributed to a specific functional group.

At the moment we propose two models that may explain the change in the appearance of the molecule and its electronic structure. Either the voltage pulse establishes a chemical bond between the isocyanato group and the silver surface, turning the N3 molecule upright and decoupling it this way, or the pulse may detach a hydrogen atom, thus changing the electronic structure and giving rise to a state close to the Fermi energy. So far it is not possible to decide which model is valid.

Ruthenium based dyes, like N3, are of recent interest but the use of established surface science techniques is limited because they cannot be deposited by thermal evaporation. Studies using the electrospray deposition technique have already been presented [83, 84], but so far no in situ mass filter was used. Because the existence of fragments is obvious in Figure 4.13(d) a mass filter is of great importance to prevent impurities from reaching the surface. To the best of our knowledge, this is the first time that the topographic and electronic structure of single N3 molecule (or any other of the mentioned ruthenium based dyes) could be observed.

Electrospray deposition of ruthenium based dyes should provide better understanding of the adsorption mechanism on different substrates and the electron transport from the molecule to these substrates in near future.

Conclusion

A new electrospray deposition instrument for preparation of organic molecules on surfaces in ultra–high vacuum has been developed and put into operation. The apparatus is directly attached to a custom–made cryogenic scanning tunnelling and atomic force microscope system. This enables deposition and characterization of prepared surfaces without breaking the vacuum.

Molecules are transferred into the gas phase by the electrospray ionization technique. Because the ion formation takes place at ambient pressure, a pressure gap of twelve orders of magnitude has to be bridged. Therefore five differentially pumped vacuum chambers were installed. Several ion optical devices are used to guide and purify the ion beam. A two stage radio frequency ion funnel accomplishes a high overall transmission of more than ten percent from the electrospray ion source to the molecular flow regime in the high vacuum chambers. The ion beam is purified in two steps. At first neutral contaminations originating from the spray are filtered by an electrostatic quadrupole deflector. Then charged particles are filtered by an in–line quadrupole mass filter. Finally the ion beam is conducted to the sample surface in the deposition stage in the preparation chamber of the LT–STAFM system at a pressure of 1×10^{-9} mbar.

Because the new home built ion funnel exhibits smaller inner diameters than previously reported designs, its transmission characteristics were investigated by a numerical method. The results of the simulation are in good agreement with the experiments. They can be used to obtain initial parameters for voltage and pressure settings. In addition the influence of the charged particles scattering cross section on the DC versus RF transmission plots can help to estimate their size, to, for example, identify charged droplets. As low kinetic energies are used for deposition, no additional buffer layer for soft landing is required. The achieved ion currents of up to 100 pA allow preparation of coverages well suited for STM investigation in a few hours.

The experimental results (Chapter 4) prove that our electrospray deposition setup is able to deposit a variety of substances onto solid surfaces in a controlled way. The range of substances available for deposition under ultra–high vacuum conditions can be increased by the electrospray ionization technique. Most of the used substances are thermally unstable and not suited for thermal evaporation, but stay intact during electrospray deposition.

The results on the porphyrin MnTPPS (Section 4.1) indicate, that the presented electrospray deposition apparatus is capable of achieving the same sample qualities

known from other UHV–compatible techniques such as thermal deposition or from pulsed injection of DNA. The ability to deposit molecules of a wide mass range (from less than 500 u to more than 50000 u) was demonstrated by one of the free ligands of metal–organic grid complexes on the one hand and BSA on the other hand.

In most of the reported experiments the possibility to use the mass filter during deposition enabled us to efficiently remove molecular fragments and other impurities from the ion beam. In general the availability of the mass filter provides some further information on the substances used.

The developed electrospray deposition instrument is state of the art in all key features. The experimental results prove the capability of the electrospray deposition technique to deposit fragile substances on surfaces in a well defined way permitting to investigate them by established surface science techniques.

Bibliography

1. Hamann, C., Woltmann, R., Hong, I., Hauptmann, N., Karan, S. & Berndt, R. Ultrahigh vacuum deposition of organic molecules by electrospray ionization. *Review of Scientific Instruments* **82,** 033903 (2011).
2. Beuhler, R. J., Flanigan, E., Greene, L. J. & Friedman, L. Proton Transfer Mass Spectrometry of Peptides. A Rapid Heating Technique for Underivatized Peptides Containing Arginine. *Journal of the American Chemical Society* **96,** 3990–3999 (June 1974).
3. Tanaka, H. & Kawai, T. Scanning tunneling microscopy imaging and manipulation of DNA oligomer adsorbed on Cu(111) surfaces by a pulse injection method. *Journal of Vacuum Science & Technology B: Microelectronics and Nanometer Structures* **15,** 602–604 (May 1997).
4. Okabayashi, Y., Kanai, K., Ouchi, Y. & Seki, K. Apparatus for solution jet beam deposition of organic thin films and in situ ultraviolet photoelectron spectroscopy. *Review of Scientific Instruments* **77,** 033905 (2006).
5. Yamada, T., Suzuki, H., Miki, H., Maofa, G. & Mashiko, S. High–Resolution Scanning Tunneling Microscopy Images of Molecular Overlayers Prepared by a New Molecular Beam Deposition Apparatus with Spray–Jet Technique. *The Journal of Physical Chemistry B* **109,** 3183–3188 (Mar. 2005).
6. McNeal, C. J., Macfarlane, R. D. & Thurston, E. L. Thin Film Deposition by the Electrospray Method for Californium–252 Plasma Desorption Studies of Involatile Molecules. *Analytical Chemistry* **51,** 2036–2039 (Oct. 1979).
7. Ouyang, Z., Takats, Z., Blake, T. A., Gologan, B., Guymon, A. J., Wiseman, J. M., Oliver, J. C., Davisson, V. J. & Cooks, R. G. Preparing Protein Microarrays by Soft–Landing of Mass–Selected Ions. *Science* **301,** 1351–1354 (Sept. 2003).
8. Gologan, B., Takáts, Z., Alvarez, J., Wiseman, J. M., Talaty, N., Ouyang, Z. & Cooks, R. G. Ion soft–landing into liquids: Protein identification, separation, and purification with retention of biological activity. *Journal of the American Society for Mass Spectrometry* **15,** 1874–1884 (Dec. 2004).
9. Rauschenbach, S., Stadler, F. L., Lunedei, E., Malinowski, N., Koltsov, S., Costantini, G. & Kern, K. Electrospray Ion Beam Deposition of Clusters and Biomolecules. *Small* **2,** 540–547 (2006).

10. Thontasen, N., Levita, G., Malinowski, N., Deng, Z., Rauschenbach, S. & Kern, K. Grafting Crown Ether Alkali Host-Guest Complexes at Surfaces by Electrospray Ion Beam Deposition. *The Journal of Physical Chemistry C* **114,** 17768–17772 (Oct. 2010).

11. Hadjar, O., Wang, P., Futrell, J. H., Dessiaterik, Y., Zhu, Z., Cowin, J. P., Iedema, M. J. & Laskin, J. Design and Performance of an Instrument for Soft Landing of Biomolecular Ions on Surfaces. *Analytical Chemistry* **79,** 6566–6574 (2007).

12. Laskin, J., Wang, P. & Hadjar, O. Soft–landing of peptide ions onto self–assembled monolayer surfaces: an overview. *Physical Chemistry Chemical Physics* **10,** 1079–1090 (2008).

13. Laskin, J., Wang, P. & Hadjar, O. Soft–Landing of $Co^{III}(salen)^{+}$ and $Mn^{III}(salen)^{+}$ on Self–Assembled Monolayer Surfaces. *The Journal of Physical Chemistry C* **114,** 5305–5311 (Apr. 2010).

14. Franchetti, V., Solka, B. H., Baitinger, W. E., Amy, J. W. & Cooks, R. G. Soft landing of ions as a means of surface modification. *International Journal or Mass Spectrometry and Ion Physics* **23,** 29–35 (Jan. 1977).

15. Swarbrick, J. C., Taylor, J. B. & O'Shea, J. N. Electrospray deposition in vacuum. *Applied Surface Science* **252,** 5622–5626 (May 2006).

16. Kantrowitz, A. & Grey, J. A High Intensity Source for the Molecular Beam. Part I. Theoretical. *Review of Scientific Instruments* **22,** 328 (1951).

17. Lüth, H. *Solid Surfaces, Interfaces and Thin Films* 5th ed. ISBN: 9783642135910 (Springer, Berlin, Aug. 2010).

18. Fenn, J. B., Mann, M., Meng, C., Wong, S. & Whitehouse, C. Electrospray ionization for mass spectrometry of large biomolecules. *Science* **246,** 64–71 (Oct. 1989).

19. Fenn, J. B. Electrospray Wings for Molecular Elephants (Nobel Lecture)13. *Angewandte Chemie International Edition* **42,** 3871–3894 (2003).

20. de Hoffmann, E. & Stroobant, V. *Mass spectrometry: principles and applications* ISBN: 9780470033104 (Wiley–Interscience, Oct. 2007).

21. Gross, J. H. *Mass Spectrometry: A Textbook* ISBN: 3540407391 (Springer, June 2006).

22. Taylor, G. Disintegration of Water Drops in an Electric Field. *Proceedings of the Royal Society of London. Series A. Mathematical and Physical Sciences* **280,** 383–397 (July 1964).

23. Rayleigh. XX. On the equilibrium of liquid conducting masses charged with electricity. *Philosophical Magazine Series 5* **14,** 184 (1882).

24. Duft, D., Achtzehn, T., Muller, R., Huber, B. A. & Leisner, T. Coulomb fission: Rayleigh jets from levitated microdroplets. *Nature* **421,** 128 (Jan. 2003).

25. Dole, M. Molecular Beams of Macroions. *The Journal of Chemical Physics* **49,** 2240 (1968).

26. Iribarne, J. V. On the evaporation of small ions from charged droplets. *The Journal of Chemical Physics* **64,** 2287 (1976).

27. Kebarle, P. A brief overview of the present status of the mechanisms involved in electrospray mass spectrometry. *Journal of Mass Spectrometry* **35,** 804–817. ISSN: 1096-9888 (July 2000).

28. Kolb, C. E. & Herschbach, D. R. John Bennett Fenn. *The Journal of Physical Chemistry* **88,** 4447–4451 (1984).

29. Yamashita, M. & Fenn, J. B. Electrospray ion source. Another variation on the free–jet theme. *The Journal of Physical Chemistry* **88,** 4451–4459 (1984).

30. Yamashita, M. & Fenn, J. B. Negative ion production with the electrospray ion source. *The Journal of Physical Chemistry* **88,** 4671–4675 (1984).

31. Whitehouse, C. M., Dreyer, R. N., Yamashita, M. & Fenn, J. B. Electrospray interface for liquid chromatographs and mass spectrometers. *Analytical Chemistry* **57,** 675–679 (Mar. 1985).

32. Karas, M., Bahr, U. & Dülcks, T. Nano–electrospray ionization mass spectrometry: addressing analytical problems beyond routine. *Fresenius' Journal of Analytical Chemistry* **366,** 669–676 (Mar. 2000).

33. Bruins, A. P., Covey, T. R. & Henion, J. D. Ion spray interface for combined liquid chromatography/atmospheric pressure ionization mass spectrometry. *Analytical Chemistry* **59,** 2642–2646 (Nov. 1987).

34. Banks, J. F., Shen, S., Whitehouse, C. M. & Fenn, J. B. Ultrasonically assisted electrospray ionization for LC/MS determination of nucleosides from a transfer RNA digest. *Analytical Chemistry* **66,** 406–414 (Feb. 1994).

35. Wilm, M. & Mann, M. Analytical Properties of the Nanoelectrospray Ion Source. *Analytical Chemistry* **68,** 1–8 (Jan. 1996).

36. Little, D. P., Chorush, R. A., Speir, J. P., Senko, M. W., Kelleher, N. L. & McLafferty, F. W. Rapid Sequencing of Oligonucleotides by High–Resolution Mass Spectrometry. *Journal of the American Chemical Society* **116,** 4893–4897 (June 1994).

37. Limbach, P. A., Crain, P. F. & McCloskey, J. A. Molecular mass measurement of intact ribonucleic acids via electrospray ionization quadrupole mass spectrometry. *Journal of the American Society for Mass Spectrometry* **6,** 27–39 (Jan. 1995).

38. Little, D. P., Thannhauser, T. W. & McLafferty, F. W. Verification of 50– to 100–mer DNA and RNA sequences with high–resolution mass spectrometry. *Proceedings of the National Academy of Sciences* **92,** 2318–2322 (Mar. 1995).

39. De Bellis, G., Salani, G., Battaglia, C., Pietta, P., Rosti, E. & Mauri, P. Electrospray ionization mass spectrometry of synthetic oligonucleotides using 2–propanol and spermidine. *Rapid Communications in Mass Spectrometry* **14,** 243–249 (Feb. 2000).

40. Viseux, N., de Hoffmann, E. & Domon, B. Structural Analysis of Permethylated Oligosaccharides by Electrospray Tandem Mass Spectrometry. *Analytical Chemistry* **69,** 3193–3198 (1997).

41. Colton, R., D'Agostino, A. & Traeger, J. C. Electrospray mass spectrometry applied to inorganic and organometallic chemistry. *Mass Spectrometry Reviews* **14,** 79–106 (Mar. 1995).

42. Traeger, J. C. Electrospray mass spectrometry of organometallic compounds. *International Journal of Mass Spectrometry* **200,** 387–401 (Dec. 2000).

43. Gerlich, D. in *State–Selected and State–to–State Ion–Molecule Reaction Dynamics* (eds Ng, C. Y. & Baer, M.) *Advances in Chemical Physics Series* LXXXII (J. Wiley & Sons, 1992).

44. Teloy, E. & Gerlich, D. Integral cross sections for ion–molecule reactions. I. The guided beam technique. *Chemical Physics* **4,** 417–427 (June 1974).

45. Weibel, E. S. & Clark, G. L. Confinement of an electron beam by oscillating electromagnetic fields. *Journal of Nuclear Energy. Part C, Plasma Physics, Accelerators, Thermonuclear Research* **2,** 112–116 (Jan. 1961).

46. Gerlich, D. in *Electronic and Atomic Collisions* (eds Lorents, D., Meyerhof, W. & Peterson, J.) 541 (Elsevier, Amsterdam, 1986).

47. Tolmachev, A. V., Chernushevich, I. V., Dodonov, A. F. & Standing, K. G. A collisional focusing ion guide for coupling an atmospheric pressure ion source to a mass spectrometer. *Nuclear Instruments and Methods in Physics Research Section B: Beam Interactions with Materials and Atoms* **124,** 112–119 (Apr. 1997).

48. Paul, W. & Raether, M. Das elektrische Massenfilter. *Zeitschrift für Physik* **140,** 262–273 (May 1955).

49. Paul, W. Electromagnetic traps for charged and neutral particles. *Reviews of Modern Physics* **62,** 531 (July 1990).

50. Fischer, E. Die dreidimensionale Stabilisierung von Ladungsträgern in einem Vierpolfeld. *Zeitschrift für Physik* **156,** 1–26 (Mar. 1959).

51. Wuerker, R. F., Shelton, H. & Langmuir, R. V. Electrodynamic Containment of Charged Particles. *Journal of Applied Physics* **30,** 342 (1959).

52. Sträng, J. E. On the characteristic exponents of Floquet solutions to the Mathieu equation. *Académie Royale de Belgique. Bulletin de la Classe des Sciences. no. 7–12* **16,** 269–287 (Oct. 2005).

53. Jones, T. *Mathieu's Equations and the Ideal rf–Paul Trap* 2006.

54. Brinkmann, U. A modified quadrupole mass filter for the separation of ions of higher masses with high transmission. *International Journal or Mass Spectrometry and Ion Physics* **9,** 161–166 (July 1972).

55. Holme, A. E., Sayyid, S. & Leck, J. H. A detailed study of the quadrupole mass filter operating with no d.c. component of the rods. *International Journal or Mass Spectrometry and Ion Physics* **26,** 191–204 (Feb. 1978).

56. Dawson, P. H. Performance characteristics of an r.f.–only quadrupole. *International Journal of Mass Spectrometry and Ion Processes* **67,** 267–276 (Nov. 1985).

57. Paul, W., Reinhard, H. P. & Zahn, U. Das elektrische Massenfilter als Massenspektrometer und Isotopentrenner. *Zeitschrift für Physik* **152,** 143–182 (Apr. 1958).

58. Langmuir, I. The Effect of Space Charge and Residual Gases on Thermionic Currents in High Vacuum. *Physical Review* **2,** 450 (1913).

59. Shampine, L. F. & Gordon, M. K. *Computer Solution of Ordinary Differential Equations: The Initial Value Problem* ISBN: 0716704617 (W. H. Freeman & Co Ltd, June 1975).

60. Tolmachev, A. V., Kim, T., Udseth, H. R., Smith, R. D., Bailey, T. H. & Futrell, J. H. Simulation-based optimization of the electrodynamic ion funnel for high sensitivity electrospray ionization mass spectrometry. *International Journal of Mass Spectrometry* **203,** 31–47 (Dec. 2000).

61. Tolmachev, A. V., Udseth, H. R. & Smith, R. D. Charge Capacity Limitations of Radio Frequency Ion Guides in Their Use for Improved Ion Accumulation and Trapping in Mass Spectrometry. *Analytical Chemistry* **72,** 970–978 (Mar. 2000).

62. Binnig, G., Rohrer, H., Gerber, C. & Weibel, E. Surface Studies by Scanning Tunneling Microscopy. *Physical Review Letters* **49,** 57 (July 1982).

63. Chen, C. J. *Introduction to Scanning Tunneling Microscopy* ISBN: 9780195071504 (Oxford University Press, USA, May 1993).

64. Tersoff, J. & Hamann, D. R. Theory and Application for the Scanning Tunneling Microscope. *Physical Review Letters* **50,** 1998 (June 1983).

65. Tersoff, J. & Hamann, D. R. Theory of the scanning tunneling microscope. *Physical Review B* **31,** 805 (Jan. 1985).

66. Bardeen, J. Tunnelling from a Many–Particle Point of View. *Physical Review Letters* **6,** 57 (Jan. 1961).

67. Feenstra, R., Stroscio, J. A. & Fein, A. Tunneling spectroscopy of the Si(111) 2×1 surface. *Surface Science* **181,** 295–306 (Mar. 1987).

68. Lang, N. D. Spectroscopy of single atoms in the scanning tunneling microscope. *Physical Review B* **34,** 5947 (Oct. 1986).

69. Stroscio, J. A., Feenstra, R. M. & Fein, A. P. Electronic Structure of the Si(111) 2×1 Surface by Scanning–Tunneling Microscopy. *Physical Review Letters* **57,** 2579 (Nov. 1986).

70. Güntherodt, H. J. *Scanning Tunneling Microscopy I: General Principles and Applications to Clean and Adsorbate–Covered Surfaces* ISBN: 0387543082 (Springer–Verlag, Aug. 1992).

71. Wiesendanger, R. *Scanning Tunneling Microscopy II: Further Applications and Related Scanning Techniques* ISBN: 0387545557 (Springer–Verlag, Aug. 1992).

72. Wiesendanger, R. *Scanning Tunneling Microscopy III: Theory of Stm and Related Scanning Probe Methods* ISBN: 0387563172 (Springer–Verlag, Aug. 1993).

73. Shaffer, S. A., Tang, K., Anderson, G. A., Prior, D. C., Udseth, H. R. & Smith, R. D. A novel ion funnel for focusing ions at elevated pressure using electrospray ionization mass spectrometry. *Rapid Communications in Mass Spectrometry* **11,** 1813–1817 (1997).

74. Gerlich, D. & Käfer, G. Ion trap studies of association processes in collisions of CH_3^+ and CD_3^+ with n–H_2, p–H_2, D_2, and He at 80 K. *The Astrophysical Journal* **347,** 849–854 (Dec. 1989).

75. Kelly, R. T., Tolmachev, A. V., Page, J. S., Tang, K. & Smith, R. D. The ion funnel: Theory, implementations, and applications. *Mass Spectrometry Reviews* **29,** 294–312 (2009).

76. Cermak, I. Compact radio–frequency power supply for ion and particle guides and traps. *Review of Scientific Instruments* **76,** 063302 (2005).

77. Kim, T., Tolmachev, A. V., Harkewicz, R., Prior, D. C., Anderson, G., Udseth, H. R., Smith, R. D., Bailey, T. H., Rakov, S. & Futrell, J. H. Design and Implementation of a New Electrodynamic Ion Funnel. *Analytical Chemistry* **72,** 2247–2255 (May 2000).

78. Dahl, D. A. SIMION for the personal computer in reflection. *International Journal of Mass Spectrometry* **200,** 3–25 (Dec. 2000).

79. Mahaffy, P. R. & Lai, K. An electrostatic quadrupole deflector for mass spectrometer applications. *Journal of Vacuum Science & Technology A: Vacuum, Surfaces, and Films* **8,** 3244–3246 (July 1990).

80. Farley, J. W. Simple electrostatic quadrupole ion beam deflector. *Review of Scientific Instruments* **56,** 1834 (1985).

81. Zeman, H. D. Deflection of an ion beam in the two–dimensional electrostatic quadrupole field. *Review of Scientific Instruments* **48,** 1079 (1977).

82. Kimmell, D. *GP–203D Quadrupole Mass Filters* Nov. 2010.

83. Mayor, L. C., Ben Taylor, J., Magnano, G., Rienzo, A., Satterley, C. J., O'Shea, J. N. & Schnadt, J. Photoemission, resonant photoemission, and x–ray absorption of a Ru(II) complex adsorbed on rutile TiO_2(110) prepared by in situ electrospray deposition. *The Journal of Chemical Physics* **129,** 114701 (2008).

84. Mayor, L. C., Saywell, A., Magnano, G., Satterley, C. J., Schnadt, J. & O'Shea, J. N. Adsorption of a Ru(II) dye complex on the Au(111) surface: Photoemission and scanning tunneling microscopy. *The Journal of Chemical Physics* **130,** 164704 (2009).

85. Tewari, Y. B., Goldberg, R. N. & Sato, M. Thermodynamics of the hydrolysis and cyclization reactions of α–, β–, and γ–cyclodextrin. *Carbohydrate Research* **301,** 11–22 (June 1997).

86. Allison, R. R., Downie, G. H., Cuenca, R., Hu, X., Childs, C. J. & Sibata, C. H. Photosensitizers in clinical PDT. *Photodiagnosis and Photodynamic Therapy* **1,** 27–42 (May 2004).

87. Foote, C. S. Definition of Type I and Type II Photosensitized Oxidation. *Photochemistry and Photobiology* **54,** 659–659 (Nov. 1991).

88. Joran, A. D., Leland, B. A., Felker, P. M., Zewail, A. H., Hopfield, J. J. & Dervan, P. B. Effect of exothermicity on electron transfer rates in photosynthetic molecular models. *Nature* **327,** 508–511 (June 1987).

89. Hessenauer–Ilicheva, N., Franke, A., Meyer, D., Woggon, W. & van Eldik, R. Mechanistic Insight into Formation of Oxo–Iron(IV) Porphyrin π–Cation Radicals from Enzyme Mimics of Cytochrome P450 in Organic Solvents. *Chemistry – A European Journal* **15,** 2941–2959 (Mar. 2009).

90. Auwärter, W., Klappenberger, F., Weber–Bargioni, A., Schiffrin, A., Strunskus, T., Wöll, C., Pennec, Y., Riemann, A. & Barth, J. V. Conformational Adaptation and Selective Adatom Capturing of Tetrapyridyl–porphyrin Molecules on a Copper (111) Surface. *Journal of the American Chemical Society* **129,** 11279–11285 (2007).

91. Weber-Bargioni, A., Auwärter, W., Klappenberger, F., Reichert, J., Lefrançois, S., Strunskus, T., Wöll, C., Schiffrin, A., Pennec, Y. & Barth, J. V. Visualizing the Frontier Orbitals of a Conformationally Adapted Metalloporphyrin. *ChemPhysChem* **9,** 89–94 (2008).

92. Yokoyama, T., Yokoyama, S., Kamikado, T. & Mashiko, S. Nonplanar adsorption and orientational ordering of porphyrin molecules on Au(111). *The Journal of Chemical Physics* **115,** 3814 (2001).

93. Jung, T. A., Schlittler, R. R. & Gimzewski, J. K. Conformational identification of individual adsorbed molecules with the STM. *Nature* **386,** 696–698 (Apr. 1997).

94. Brede, J., Linares, M., Kuck, S., Schwöbel, J., Scarfato, A., Chang, S., Hoffmann, G., Wiesendanger, R., Lensen, R., Kouwer, P. H. J., Hoogboom, J., Rowan, A. E., Bröring, M., Funk, M., Stafström, S., Zerbetto, F. & Lazzaroni, R. Dynamics of molecular self–ordering in tetraphenyl porphyrin monolayers on metallic substrates. *Nanotechnology* **20,** 275602 (July 2009).

95. Brede, J., Linares, M., Lensen, R., Rowan, A. E., Funk, M., Broring, M., Hoffmann, G. & Wiesendanger, R. Adsorption and conformation of porphyrins on metallic surfaces. *Journal of Vacuum Science & Technology B* **27,** 799–804 (Mar. 2009).

96. Klappenberger, F., Weber–Bargioni, A., Auwärter, W., Marschall, M., Schiffrin, A. & Barth, J. V. Temperature dependence of conformation, chemical state, and metal–directed assembly of tetrapyridyl–porphyrin on Cu(111). *The Journal of Chemical Physics* **129,** 214702 (2008).

97. Buchner, F., Flechtner, K., Bai, Y., Zillner, E., Kellner, I., Steinru?ck, H., Marbach, H. & Gottfried, J. M. Coordination of Iron Atoms by Tetraphenylporphyrin Monolayers and Multilayers on Ag(111) and Formation of Iron–Tetraphenylporphyrin. *The Journal of Physical Chemistry C* **112,** 15458–15465 (Oct. 2008).

98. Comanici, K., Buchner, F., Flechtner, K., Lukasczyk, T., Gottfried, J. M., Steinruck, H. & Marbach, H. Understanding the Contrast Mechanism in Scanning Tunneling Microscopy (STM) Images of an Intermixed Tetraphenylporphyrin Layer on Ag(111). *Langmuir* **24,** 1897–1901 (Mar. 2008).

99. Horcas, I., Fernández, R., Go?mez–Rodri?guez, J. M., Colchero, J., Go?mez–Herrero, J. & Baro, A. M. WSXM: A software for scanning probe microscopy and a tool for nanotechnology. *Review of Scientific Instruments* **78,** 013705 (2007).

100. Bhattacharya, A. A., Curry, S. & Franks, N. P. Binding of the General Anesthetics Propofol and Halothane to Human Serum Albumin. *Journal of Biological Chemistry* **275,** 38731 –38738 (Dec. 2000).

101. Hirayama, K., Akashi, S., Furuya, M. & Fukuhara, K.-i. Rapid confirmation and revision of the primary structure of bovine serum albumin by ESIMS and frit–FAB LC/MS. *Biochemical and Biophysical Research Communications* **173,** 639–646 (Dec. 1990).

102. Axelsson, I. Characterization of proteins and other macromolecules by agarose gel chromatography. *Journal of Chromatography A* **152,** 21–32 (May 1978).

103. Quist, A. P., Björck, L. P., Reimann, C. T., Oscarsson, S. O. & Sundqvist, B. U. R. A scanning force microscopy study of human serum albumin and porcine pancreas trypsin adsorption on mica surfaces. *Surface Science* **325,** L406–L412 (Feb. 1995).

104. Kasianowicz, J. J., Brandin, E., Branton, D. & Deamer, D. W. Characterization of individual polynucleotide molecules using a membrane channel. *Proceedings of the National Academy of Sciences* **93,** 13770–13773 (Nov. 1996).

105. Akeson, M. Microsecond Time–Scale Discrimination Among Polycytidylic Acid, Polyadenylic Acid, and Polyuridylic Acid as Homopolymers or as Segments Within Single RNA Molecules. *Biophysical Journal* **77,** 3227–3233 (Dec. 1999).

106. Meller, A., Nivon, L., Brandin, E., Golovchenko, J. & Branton, D. Rapid nanopore discrimination between single polynucleotide molecules. *Proceedings of the National Academy of Sciences* **97,** 1079–1084 (Feb. 2000).

107. Moudrianakis, E. N. & Beer, M. Base Sequence Determination in Nucleic Acids with the Electron Microscope, III. Chemistry and Microscopy of Guanine–Labeled DNA. *Proceedings of the National Academy of Sciences* **53,** 564–571 (Mar. 1965).

108. Clemmer, C. & Beebe, T. Graphite: a mimic for DNA and other biomolecules in scanning tunneling microscope studies. *Science* **251,** 640–642 (Feb. 1991).

109. Tanaka, H. & Kawai, T. Visualization of detailed structures within DNA. *Surface Science* **539,** L531–L536 (Aug. 2003).

110. Yoshida, Y., Nojima, Y., Tanaka, H. & Kawai, T. Scanning tunneling spectroscopy of single–strand deoxyribonucleic acid for sequencing. *Journal of Vacuum Science & Technology B: Microelectronics and Nanometer Structures* **25,** 242 (2007).

111. Tanaka, H. & Kawai, T. Partial sequencing of a single DNA molecule with a scanning tunnelling microscope. *Nature Nanotechnology* **4,** 518–522 (2009).

112. Gabelica, V., Rosu, F., Houssier, C. & De Pauw, E. Gas phase thermal denaturation of an oligonucleotide duplex and its complexes with minor groove binders. *Rapid Communications in Mass Spectrometry* **14,** 464–467 (Mar. 2000).

113. Tanaka, H., Hamai, C., Kanno, T. & Kawai, T. High–resolution scanning tunneling microscopy imaging of DNA molecules on Cu(111) surfaces. *Surface Science* **432,** L611–L616 (July 1999).

114. Hanan, G. S., Arana, C. R., Lehn, J. & Fenske, D. Synthesis, Structure, and Properties of Dinuclear and Trinuclear Rack–Type Ru^{II} Complexes. *Angewandte Chemie International Edition in English* **34,** 1122–1124 (June 1995).

115. Waldmann, O., Hassmann, J., Müller, P., Hanan, G. S., Volkmer, D., Schubert, U. S. & Lehn, J. Intramolecular Antiferromagnetic Coupling in Supramolecular Grid Structures with Co^{2+} Metal Centers. *Physical Review Letters* **78,** 3390 (Apr. 1997).

116. Hassmann, J., Hahn, C. Y., Waldmann, O., Volz, E., Schleemilch, H., Hallschmid, N., M?ller, P., Hanan, G. S., Volkmer, D., Schubert, U. S., Lehn, J., Mauser, H., Hirsch, A. & Clark, T. Structural and Electronic Properties of Self–Assembled Supramolecular Grid Structures: Doping of Supramolecular Thin Films. *MRS Online Proceedings Library* **488,** null (1997).

117. Mourran, A., Ziener, U., Möller, M., Breuning, E., Ohkita, M. & Lehn, J. Two Morphologies of Stable, Highly Ordered Assemblies of a Long–Chain–Substituted [2×2]–Grid–Type Fe^{II} Complex Adsorbed on HOPG. *European Journal of Inorganic Chemistry* **2005,** 2641–2647 (July 2005).

118. Alam, M. S., Strömsdörfer, S., Dremov, V., Müller, P., Kortus, J., Ruben, M. & Lehn, J. Addressing the Metal Centers of [2×2] Co_4^{II} Grid–Type Complexes by STM/STS. *Angewandte Chemie International Edition* **44,** 7896–7900 (Dec. 2005).

119. Pace, G., Stefankiewicz, A., Harrowfield, J., Lehn, J. & Samorì, P. Self–Assembly of Alkoxy–Substituted Bis(hydrazone)–Based Organic Ligands and of a Metallosupramolecular Grid on Graphite. *ChemPhysChem* **10,** 699–705 (Mar. 2009).

120. O'Regan, B. & Grätzel, M. A low–cost, high–efficiency solar cell based on dye–sensitized colloidal TiO_2 films. *Nature* **353,** 737–740 (Oct. 1991).

121. Gao, F., Wang, Y., Zhang, J., Shi, D., Wang, M., Humphry–Baker, R., Wang, P., Zakeeruddin, S. M. & Grätzel, M. A new heteroleptic ruthenium sensitizer enhances the absorptivity of mesoporous titania film for a high efficiency dye–sensitized solar cell. *Chemical Communications,* 2635 (2008).

122. Hagfeldt, A. & Grätzel, M. Molecular Photovoltaics. *Accounts of Chemical Research* **33,** 269–277 (May 2000).

123. Grätzel, M. Photoelectrochemical cells. *Nature* **414,** 338–344 (Nov. 2001).

124. Grätzel, M. Dye–sensitized solar cells. *Journal of Photochemistry and Photobiology C: Photochemistry Reviews* **4,** 145–153 (Oct. 2003).

125. Grätzel, M. Applied physics: Solar cells to dye for. *Nature* **421,** 586–587 (Feb. 2003).

126. McFarland, E. W. & Tang, J. A photovoltaic device structure based on internal electron emission. *Nature* **421,** 616–618 (Feb. 2003).

127. Nazin, G. V., Qiu, X. H. & Ho, W. Vibrational spectroscopy of individual doping centers in a monolayer organic crystal. *The Journal of Chemical Physics* **122,** 181105 (2005).

128. Nazin, G. V., Qiu, X. H. & Ho, W. Charging and Interaction of Individual Impurities in a Monolayer Organic Crystal. *Physical Review Letters* **95,** 166103 (Oct. 2005).

129. Wu, S. W., Nazin, G. V., Chen, X., Qiu, X. H. & Ho, W. Control of Relative Tunneling Rates in Single Molecule Bipolar Electron Transport. *Physical Review Letters* **93,** 236802 (Dec. 2004).

List of Figures

List of Abbreviations

AFM	Atomic Force Microscope
BSA	Bovine Serum Albumin
CRM	Charge Residue Model
DNA	Deoxyribonucleic Acid
DOS	Density of States
DSC	Dye Sensitized Solar Cell
ESI	Electrospray Ionization
ESMERALDA	Electrospray Ionization Mass and Energy Resolving Adsorbate Layer Deposition Apparatus
HOMO	Highest Occupied Molecular Orbital
LDOS	Local Density of States
LT–STAFM	Low–Temperature Scanning Tunnelling and Atomic Force Microscope
LUMO	Lowest Unoccupied Molecular Orbital
MALDI	Matrix-Assisted Laser Desorption / Ionization
STM	Scanning Tunnelling Microscopy
STS	Scanning Tunnelling Spectroscopy
TCS	Transient Charged State
TEM	Transmission Electron Microscope
UHV	Ultra–High Vacuum

Danksagung

Ich bedanke mich bei allen Personen, die zum Gelingen dieser Arbeit beigetragen haben. Prof. Dr. Richard Berndt gilt mein besonderer Dank für die Möglichkeit, diese Arbeit in seiner Gruppe (der *AG Raster–Tunnelmikroskopie*) durchzuführen, für die fazinierende Themenstellung, das harmonische Arbeitsklima, seine stets wertvolle Unterstützung und das große in mich gesetzte Vertrauen. Weiterhin danke ich Dr. Thomas Jürgens; sein großes Interesse, seine weitreichende Erfahrung mit dem Aufbau von Experimenten und seine hilfreichen Ratschläge waren für die Verwirklichung der Arbeit sehr wichtig. Planung, Fertigung und Aufbau eines so komplexen Experimentes und seiner Komponenten sind natürlich ohne umfangreiche Hilfe nicht denkbar. René Woltmann danke ich für seine Unterstützung beim Entwurf von Komponenten und bei der Planung und Durchführung des Aufbaus, im Speziellen beim Zusammenbau der beiden großen Vakuumsystem (ESI und STM). Allen Mitarbeitern der *Zentralen Werkstatt im Physikzentrum*, besonders Frank Brach und seinem Team, danke ich für die Fertigung der benötigten apparativen Komponenten und für Verbesserungsvorschläge. Für die Realisierung der notwendigen elektronischen Komponenten danke ich Dipl.-Ing. Ali Talmat, Jörg Neubauer und Horst Schlüter. Bei einem Besuch am Institut für Physikalische Chemie in Karlsruhe wurde ich mit den Grundlagen der Elektrospray Ionisation vertraut gemacht; dafür danke ich Dr. Oli T. Ehrler und Prof. Dr. M. Kappes.

Bei meinen „Labor–Kollegen“des ELSA–Teams (**E**lectrospay Deposition – **L**ow–Temperature **S**canning–Tunnelling– and **A**tomic–Force–Microscope) bedanke ich mich für die gute Zusammenarbeit und die Durchführung eines Großteils der STM–Experimente: Nadine Hauptmann für die Untersuchungen an N3, Dr. I–Po Hong für die DNA Experimente, Sujoy Karan für das Experimentieren mit MnTPPS und den metall–organischen Gittern, Katharina Scheil für das Untersuchen von BSA und Kristof Buchmann für weitreichende Diskussionen über das Ionentrichter Design.

Dr. Markus Gruyters, Dr. Thomas Jürgens und meinem Bruder Dr. Matthias Hamann danke ich für gründliches Korrekturlesen.

Monika Seeger, Dr. Jens Kuntze und den Mitarbeiterinnen der zentralen Verwaltung im Physikzentrum danke ich für ihre Unterstützung bei allen aufgetretenen administrativen Problemen und die vielen ausgeführten Bestellungen.

Den zahlreichen Kollegen der Arbeitsgruppe, Simon Altenburg, Dr. Michael Becker, Andreas Burtzlaff, Björn Gojdka, Dr. Thiruvancheril G. Gopakumar, Dr. Thomas von Hofe, Torben Jasper–Tönnies, Henning Jensen, Thomas Knaak, Prof. Dr. Jörg Kröger, Lars Mühlenberend, Svenja Mühlenberend, Ursula Nebendahl, Dr. Nicolas Neél,

Julia Neff, Torben Pingel, Dr. Jürgen Rathlev, Dr. Patrick Schmidt, Natalia Schneider, Johannes Schöneberg, Dr. Guillaume Schull, Dr. Alexander Sperl, Dr. Yongfeng Wang, Dr. Alexander Weismann, Dr. Hao Zheng, Dr. Martin Ziegler und allen anderen danke ich für die nette Arbeitsathmosphäre, wertvolle Diskussionen und Ihre Unterstützung. Meiner Frau Dorthe danke ich dafür, dass sie mich während meiner gesamten Studienzeit immer unterstützt hat und gerade in anstrengenden Phasen der Arbeit immer viel Verständnis und Geduld aufgebracht hat. Dank gilt auch meinen Eltern Monika und Rainer, die mich immer in jeder Hinsicht tatkräftig unterstützt haben und schon früh mein Interesse an der Naturwissenschaft weckten.

Dem Land Schleswig–Holstein danke ich für die erhaltene finanzielle Förderung im Rahmen der Innovationsfonds–Projekte *Präparation und Characterisierung von Schaltbaren Oberflächen und Nanomaterialien* und *Molekulare Kräfte und Quantentransport*.

Eidesstattliche Erklärung

Hiermit erkläre ich an Eides statt, diese Arbeit selbstständig unter der Beratung meiner wissenschaftlichen Lehrer angefertigt und keine weiteren Hilfsmittel, außer den im Text angegebenen sowie den bekannten Nachschlagewerken der Naturwissenschaften, verwendet zu haben. Diese Arbeit wurde weder ganz noch in Teilen an anderer Stelle im Rahmen eines Prüfungsverfahrens vorgelegt. Frühere Promotionsversuche wurden von mir nicht vorgenommen.

Kiel, den 16. Dezember 2011

Christian Hamann